ANALYSIS AND MODELING OF AN ACTUATION SYSTEM TO BE USED IN LIGHT-WEIGHT COLLABORATIVE ROBOTS

A Thesis Submitted to
the Graduate School of Engineering and Sciences of
İzmir Institute of Technology
in Partial Fulfillment of the Requirements for the Degree of

MASTER OF SCIENCE

in Mechanical Engineering

by
Mert YILMAZ

January 2019
İZMİR

We approve the thesis of **Mert YILMAZ**

Examining Committee Members:

Assoc. Prof. Dr. Mehmet İsmet Can DEDE
Department of Mechanical Engineering
İzmir Institute of Technology

Prof. Dr. Serhan ÖZDEMİR
Department of Mechanical Engineering
İzmir Institute of Technology

Assoc. Prof. Dr. Levent ÇETİN
Department of Mechatronics Engineering
İzmir Kâtip Çelebi University

28 January 2019

Assoc. Prof. Dr. Mehmet İsmet Can DEDE
Supervisor,
Mechanical Engineering
İzmir Institute of Technology

Prof. Dr. Metin TANOĞLU
Head of the Department of
Mechanical Engineering

Prof. Dr. Aysun SOFUOĞLU
Dean of the Graduate School of
Engineering and Sciences

ACKNOWLEDGMENTS

I would like to thank my advisor, Assoc. Prof. Dr. Mehmet İsmet Can DEDE for all his guidance, understanding and patience over the last years. I consider myself fortunate to have the opportunity to study under his supervision. I would also like to appreciate my thesis committee members: Prof. Dr. Serhan ÖZDEMİR and Assoc. Prof. Dr. Levent ÇETİN for taking the time and making recommendations.

I would also like to thank warmly my dear friends in Human - Robot Interaction Lab. and Robotics Lab. for their support and friendship. I would also special thanks to Görkem KARABULUT, Orhan AYİT, Oğulcan IŞITMAN, Osman Nuri ŞAHİN, Emre UZUNOĞLU, İbrahimcan GÖRGÜLÜ, and Mert KANIK for all their persistent help and patience.

I am also thankful to my wife, Esra BİBEROĞLU YILMAZ, for her support and patience for my long hours of working in the laboratory. I am also grateful to my parents and parents-in-law for their endless support during my thesis and all my life.

ABSTRACT

ANALYSIS AND MODELING OF AN ACTUATION SYSTEM TO BE USED IN LIGHT-WEIGHT COLLABORATIVE ROBOTS

Collaborative robots are a relatively new concept in robotics and industrial automation. Traditional industrial robots are relatively expensive, heavy, and dangerous devices for humans since they are enclosed in working cells with fences. Nowadays, in small and medium enterprises (SMEs), instead of traditional robots lightweight and versatile robots are required which can work alongside human co-workers. In such applications, human safety is a critical factor. ISO has produced new standards for these robots to regulate their collaborative work with human co-workers and named these robots as collaborative robots.

The subject of the thesis is related to the actuation systems of light-weight collaborative robots. For these robots, a variety of actuation systems are designed in recent years which are usually modular and compact actuation systems. The main aim of the thesis is to analyze and model of a commonly used actuation system in collaborative robots and to verify its model.

ÖZET

HAFİF İŞBİRLİKÇİ ROBOTLARDA KULLANILACAK EYLEYİCİ SİSTEMİN ANALİZİ VE MODELLENMESİ

İşbirlikçi robotlar robotikte ve endüstriyel otomasyonda nispeten yeni bir konseptir. Geleneksel endüstriyel robotlar nispeten pahalı, ağır ve çitlerle çevrelenmiş çalışma hücreleri içinde olan, insanlar için tehlikeli cihazlardır. Günümüzde, küçük ve orta ölçekli işletmelerde (KOBİ'ler), geleneksel robotlar yerine, insan iş arkadaşlarıyla birlikte çalışabilecek hafif ve çok yönlü robotlara ihtiyaç duyulmaktadır. Bu tür uygulamalarda insan güvenliği kritik bir faktördür. ISO, bu robotların insan meslektaşlarıyla ortak çalışmalarını düzenlemek için yeni standartlar üretmiş ve bu robotları işbirlikçi robotlar olarak adlandırmıştır.

Tezin konusu hafif işbirkçi robotların eyleyici sistemleriyle ilgilidir. Bu robotlar için, son yıllarda genellikle modüler ve kompakt olmak üzere çeşitli eyleyici sistemler tasarlanmıştır. Tezin temel amacı işbirlikçi robotlarda genel olarak kullanılan eyleyici sistemi analiz etmek, modellemek ve modelini doğrulamaktır.

TABLE OF CONTENTS

LIST OF FIGURES

Figure **Page**

LIST OF TABLES

CHAPTER 1

INTRODUCTION

Robotics is a science which examines robots and their usages. Robotics comprises of autonomy, achieving tasks and sensing. A robot, by the way, is a programmable and automatic mechanical device that is designed for performing specific tasks by resembling human. Due to the faced problems in manufacturing, robots have been developed in order to perform routine or dangerous jobs instead of humans. They are called industrial robots which will be examined in detail in the next section.

1.1. Industrial Robots

By the nature of robots, they have capabilities like versatility, reprogrammable, working automatically and independently. Due to these features, robots are the indispensable part of the industry. Industrial robots improve product quality and consistency, increase production output rates and also reduce operating costs in industrial automation systems (Singh et al., 2013). The evolution of industrial robots are examined in the following subsection.

1.1.1. History of Industrial Robots

The first industrial robot developed by George Devol and Joseph Engelberger in 1959. Its weight is about two tons and control performed by a magnetic drum which is a storage device. The first industrial robot used in the factory is Unimation in 1961. It was used to make automotive interiors by executing the commands stored in a magnetic drum. In 1962, the first cylindrical robot, the Versatran - stands for Versatile Transfer, came into use in the USA.

In 1969, the first spot-welding robot was automated and improved productivity. As a consequence, it became widespread in a manner of dirty and dangerous operations. At the same year, the first commercial painting robot created. It is used for house applications due to the absence of Norwegian labor.

KUKA designed a robot, Famulus, with six electromechanically driven axes, in 1973. The company used Unimation robots to develop their robots. At about the same time, Hitachi designed the automatic bolting robot for the construction industry. The novelty of the design is dynamic vision sensors that distinguish the objects in motion. In 1974, the first industrial robot which obeys the commands from minicomputer. T3, The Tomorrow Tool, was also the first commercially available robot.

Kawasaki, Japan, developed the first arc-welding robot in 1974. It is used for spot welding and manufacturing own motorcycles. They also improved their Hi-T-Hand robot by implementing touch and force sensing capabilities. At the same year, the first fully electric, microprocessor-controlled industrial robot developed by ASEA, Sweden. The notable characteristic of the robot is its anthropomorphic design that imitates the movement of the human arm. In 1975, a cartesian-coordinate robot, SIGMA, used in assembly applications.

In 1978, Programmable Universal Machine for Assembly (PUMA) developed by Unimation. The robot has the capability that sharing the workspace with a human operator. At about the same times, SCARA-Robot (Selective Compliance Assembly Robot Arm) which resembles the human arm by its articulated two-link arm layout, developed. Also, the first six-axis robot, RE 15, with own control system developed in Germany.

Some historical examples of industrial robots are as shown in Figure 1.1.

1.1.2. Industrial Robot Applications

There are several applications of robots that are in use in industry. The popular industrial robot applications are as follows (Jabil, 2018):

- **Material Handling:** It includes many operations like selecting, picking, moving, packing and palletizing. The automated material handling allows transferring product sub-components to create the actual product. The automation reduces the need for employees. Hence, the employment cost decreases and tiresome and dangerous works put out of action. The leading companies in the material handling sector are Fanuc, Motoman, and KUKA.

- **Machine Tending:** It is an automated tracking process of loading and unloading parts to a machine. The robot carries out different functions during the operation. Hence, it brings flexibility to the robot and saves not only money but also space. The prominent companies in machine tending are ABB, KUKA, and Fanuc.

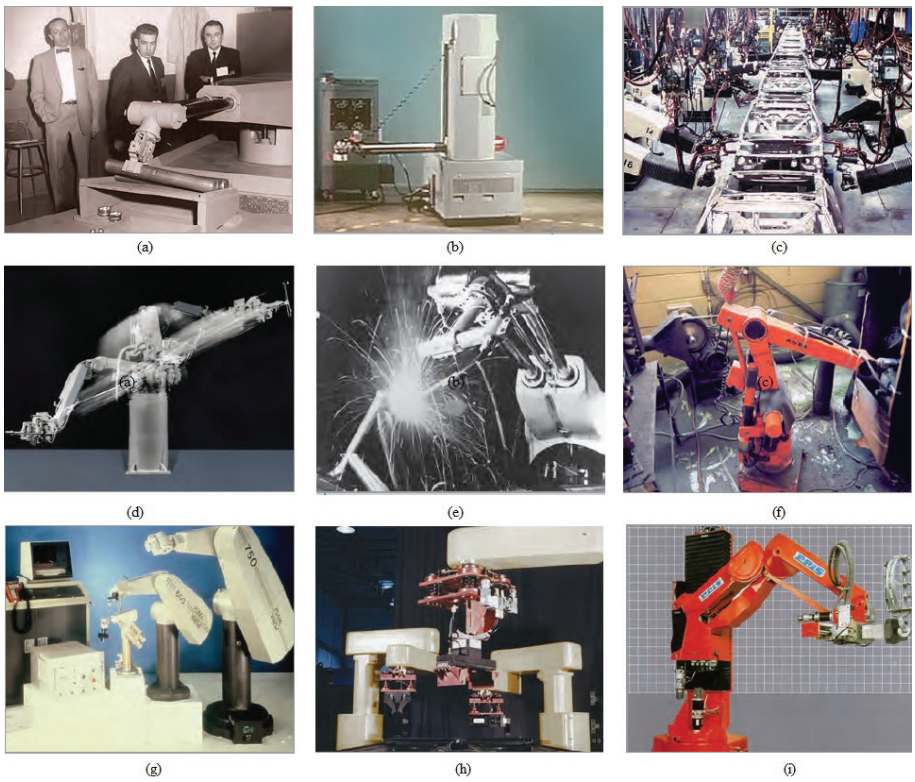

Figure 1.1. Evolution of industrial robots: a) the Unimation Robot, b) the Versatran, c) GM's spot-welding robot, d) T3-The Tomorrow Tool, e) Kawasaki's arc-welding robot, f) IRB 6 Robot, g) PUMA Robot, h) SCARA robot, i) RE15 robot (Source: IFR (2012))

- Painting, assembly, picking, machine cutting, and grinding are other useful applications that can be performed by industrial robots.

1.2. Collaborative Robots

The abovementioned industrial robot applications require high power, speed, and precision from robots. Therefore, they are heavy, expensive and single task systems and pose inevitable dangers. They are also occupants of considerable spaces. In this context, they do not require todays varying needs of industry. Small and medium enterprises suffer from unmodifiable, unsafe and low return on investment systems. In this context, cheap and high safety provided robot need arises. These robots shall work safely together with the human in a shared workspace. As a result, engineers have developed collaborative robots or in short, cobots. In other words, industrial robots came out of cages as

collaborative robots.

There is a common misunderstanding about the definition of collaborative robots. According to EN ISO 10218 part one, part two and ISO TS/15066, collaborative robots are defined as follows (Shikany, 2014):

- A collaborative robot is a device that is usable in a collaborative operation,
- Collaborative operation (Part 1, 3.4) - the process that robot with a specified task, should work in collaboration with a human in a determined workspace,
- Collaborative workspace (from TS 15066, 3.3) - the area that a human and robot system works simultaneously during the production process.

As stated in the definitions above, the robot is not alone any time.

1.2.1. ISO Standards for Collaborative Robots

According to EN ISO 10218 Part 1, 5.10; Part 2,5.11, there are four methods for collaborative operation and a collaborative application could use at least one of the methods described below (Shea, 2016).

- **Safety Rated Monitored Stop:** This technique enables the interaction between the robot and the human under certain conditions.
  - The stop condition should define before the human operator enters the specified area,
  - Power required to drive should provide continuously,
  - Robot movement resumes on although the human operator quits the specified area. Any sign does not require for the movement of the robot,
  - If stop-condition breaks, protective stop cuts-in.
- **Hand Guiding:** The robot should be hand-operated to allow the human operator to grasp and manipulate the device.
  - The robot provides safety-rated monitored stop condition before the human enters the workspace. System power should be up,
  - Motion or manipulation activate when operator handles the device,
  - Operation continues even though the operator quits the workspace.

- **Speed and Separation Monitoring:** Operator and the robot system can move in a shared workspace at the same time.
  - There should be a minimum protective separation distance between the human and the robot,
  - Protective separation distance can be adjustable by a protective device,
  - Speed should reduce when keeping minimum protective separation distance,
  - If minimum protective separation distance violates, an emergency stop occurs.
- **Power and Force Limiting:** Deliberate or indeliberate interactions between the robot and the human operator can happen.
  - Specially design robot system needed for power and force limiting,
  - Forces exerted by robot system must be limited,
  - When a physical interaction occurs, the robot system should react.

1.2.2. History of Collaborative Robots

Cobots were first mentioned in the invention in 1996 by J. Edward Colgate and Michael Peshkin (Van, 1996). The patent approved by US (Peshkin and Colgate, 1999) in 1996, defines collaborative robots as ”an apparatus and method for direct physical interaction between a person and a general purpose manipulator controlled by a computer.”

Instead of the cobot term, the General Motors members used Intelligent Assistive Devices (IAD) alternatingly. These devices used in automotive assembly and material handling processes. In 2002, a safety standard for these devices was introduced. At the same year, Cobotics (Cranes Today, 2003) put onto the market lots of cobot models.

The first collaborative robot of KUKA, LBR 3, lunched in 2004. This robot was a result of almost ten-year contributions between KUKA and German Aerospace Center. In the later years, KUKA concentrated on collaborative robot technology and released KUKA LBR 4 to the KUKA LBR iiwa in 2008 and 2013, respectively (KUKA, 2018).

Universal Robots, another leading company in collaborative robots, designed its first cobot, UR5, in 2008. Then UR10 (2012) and UR3 (2015) models have followed UR5 model, respectively (Universal Robots, 2018).

Baxter, an industrial collaborative robot from Rethink Robotics, was introduced in the market in 2012. Sawyer robot, which is smaller and faster than Baxter, was released for high precision operations in 2015 (Rethink, 2018).

In 2015, Even Fanuc release its first collaborative robot with a heavy payload, named Fanuc CR-35iA, later released smaller collaborative robots like Fanuc CR-4iA, CR-7iA, and CR-7/L in 2016 (Fanuc, 2018).

1.2.3. Collaborative Robot Applications

Collaborative robots which are gaining popularity rapidly, have various application areas. Some of them are as follows:

- **Aerospace:**Since the aerospace industry works with large and heavy parts, the demand for collaborative robots is limited. However, they take advantage of the safety-rated monitored stop which is an important technique of cobots, and used it in traditional, high-payload robots. For example, the whole system does not shut down during the cleaning task.

  Baxter and UR robots take place for the small pick and place operations. Also, in test applications which require repetitive motions, Baxter robots are in use for ergonomic reasons. In the study by Angerer et al. (2011), researchers presents a novel automation system for preforming processes in aerospace industries by using KUKA robot.

  There are not many applications suited for collaborative robots in this area. So, the price of cobots is not the primary reason. As a result, future designs have to be more functional to take place in aerospace.

- **Automotive:**Like aerospace industry, collaborative robots are useful for applications requires ergonomic concerns like the grunt, dirty and dangerous works. Power and force limiting robots are easy to install and more advantageous than traditional robots in installation case which means less time and space and saving on cost. The automotive industry expects relatively high payloads like minimum 30 kg. However, PFLRs(Power and Force Limited Robots) have limited payloads about 10kg. Although the PFLRs like Baxter or UR is useful for safety conditions, the expectations of them are more speed and distance for the manufacturing process. Universal Robots have some case studies with leading companies such as Nissan and

Continental in automotive applications i.e. machine tending, pick and place, and assembly (Universal Robots, 2018).

- **Electronics:**There is a higher demand in the electronics industry as compared with the aerospace and automotive industries. Injection molding, creating circuit boards and final assembly are some applications which require high speed, precision, and flexibility. PFLRs are not capable of these tasks since they are not precise. On the other hand, they have light payloads and, are capable of the circuit board assembly line. Since they are easy to set up and use, one can prefer them to traditional robots. Still, the electronics industry expects better machine vision and feeders from collaborative robots. Sawyer robot takes place in electronics industry with in-circuit testing applications (Rethink, 2018).

- **Life Sciences:**Collaborative robots are preferred in life sciences operations in laboratories. They are useful for prescription preparation, drug recovery and research in disease compounds. Unlike traditional robots, they require less training for any scientists. Some engineers in life sciences think as collaborative robots are not precise or reliable. However, they are not aware of the situation that collaborative robots must not be reliable or precise for these applications and Increase in productivity after installation is the right answer. Some case studies in laboratory and testing applications with AGH University is conducted by Universal Robots (Universal Robots, 2018).

To conclude that, in the aerospace and automotive industry, the desires from collaborative robots are heavier payloads and increase in speeds. In life sciences, users expect easy to programming and an increase in precision. In the electronics industry, reducing the deployment costs and return on investment are problems to overcome.

1.2.4. Industrial Robots vs Collaborative Robots

Before focusing on today's collaborative robots, it is better to compare them with traditional industrial robots as a rival. There are some advantages and disadvantages of both types of robots (Greenfield, 2017).

Advantages of Cobots

- It can work together with an employee safely,

- It does not need to cages, so the deployment is not only cheap but also flexible,

- It is easy to programme by using the graphical user interface,
- Return on investment period is about twelve months. Also, it reduces production cost per unit up to twenty percent.

Disadvantages of Cobots

- Cobots require detailed risk assessment according to the defined safety standards via ISO. If safety precautions are not fully cover, fencing costs can arise,
- Safety conditions cause low tip speeds. The more safety conditions, the more expenditure requires,
- The payload, tip speed, precision is limited,
- It is dependent on an operator.

Advantages of Industrial Robots

- Even it has high payloads it is faster and more accurate than an operator,
- It is fully automated and faster that is no need to an operator in unsafe cages,
- Return on investment period is about between twelve and eighteen months,
- It can be used in collaborative applications with appropriate risk assessment.

Disadvantages of Industrial Robots

- It is not suitable for the small-scale enterprise since it reaches high speeds,
- Fixed deployments are costly,
- Changing the process is almost impossible,
- Programming expertize is required.

1.2.5. Light-weight Collaborative Robots

Industrial robots perform tasks with high repeatability and accuracy. So, thesystem should have not only high rigidity and power capacity but also a quick response in spite of load and own body weight.

Table 1.1. Light-weight robot arms' parameters (Source: Rodi et al., 2014)

LWR Type	DoFs	Range (mm)	Weight (kg)	Payload (kg)	Repeatability (mm)	Tip Speed (mm/s)	Compliance
Barret	7	1000	25	4	+/- 0.10	3.00	No
KR Agilus 6R700	6	706	50	6	+/- 0.03	2.00	No
LWA Powerball	6	700	12.5	6	+/- 0.06		No
LWA PA10	7	930	35	10	+/- 0.10	1.55	No
SIA5F	7	559	30	5	+/- 0.06		No
VS-6577G-B	6	854	26	7	+/- 0.03		No
LBR iiwa 7R800	7	800	22.3	7	+/- 0.10	8.2	Yes
UR5	6	850	18.4	5	+/- 0.10	1.00	Yes

It is inspired by human arms when designing collaborative robots as light-weight robot arms. However, it is still irrational to compare the weights of them. Today, the main properties to handle in this area are "decreasing the weight of the arm, increasing the payload up to human physical capabilities, achieving desired compliance of joints, and decreasing energy consumption" (Rodi et al., 2014). Some of light-weight robots' parameters of leading manufacturers according to these design requirements, are displayed in Table 1.1. Also, some of these robots are shown as in the Figure 1.2.

1.2.6. Actuation Systems in Robotics

An actuators is a part of a robotic system which changes the energy to various desired outputs. In robots, a motion or drive are originated from the actuator. They resemble to the muscles in humans. Their use depends on stability, weight and, precision given by the robot. In robotics, there are three types of actuators depending on the load.

- **Hydraulic Actuators:**They are powerful actuators that can exert high torques or forces at the output. So, high impedance features are shown in these actuators. They are suitable to work with heavy pieces of equipment. They require more control and accuracy since it works by using incompressible oil. On the other hand, they are the most expensive actuators that requires periodic maintenances. Also, they are not only the dirty systems but also the most dangerous and hazardous structures for

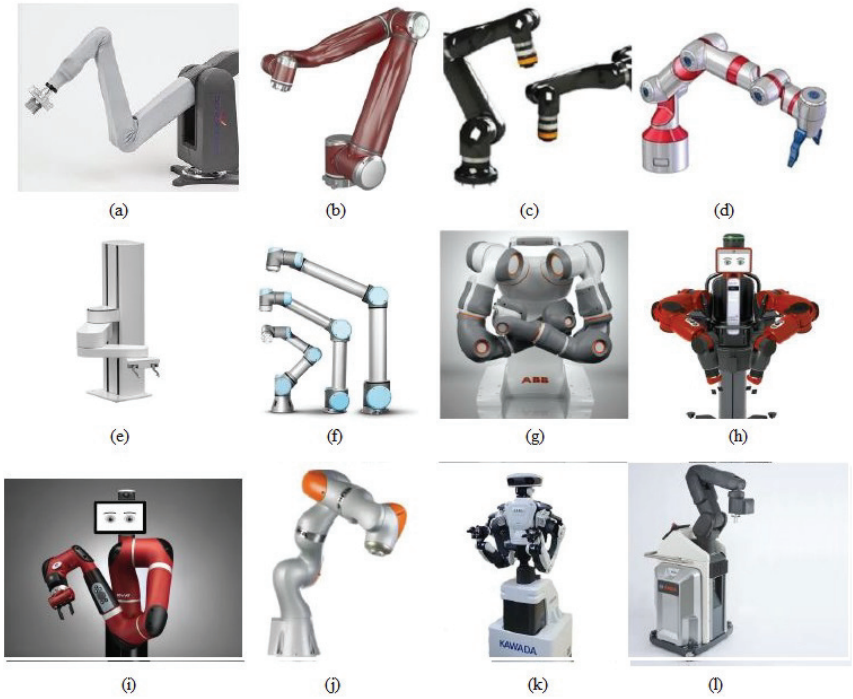

Figure 1.2. Examples of light-weight robot arms: a) BioRob Arm by Bionic Robotics, b) Speedy 10 by MABI, c) Roberta by Gomtec, d) Prob 1R by F&P Personal Robotics, , e) PF400 by Precise Automation , f) UR5 by Universal Robots, g) Yumi by ABB, h) Baxter by Rethink Robotics, i) Sawyer by Rethink Robotics, j) iiwa by KUKA, k) NEXTAGE by Kawada Industries, l) APAS by BOSCH (Source: Robotiq (2018))

people. They compose of hydraulic cylinders, valves and motors.

- **Pneumatic Actuators:**They are inexpensive actuators that are used in small-sized robots. Also, they move fast and compliant actuators with low impedance. They compose of pneumatic cylinders and motors. They have clean operations. Similar to hydraulic actuators, pneumatic actuators require periodic maintenances. They are not suitable for varying speed and suffer from low motion. They compose of pneumatic cylinders and pneumatic motors.

- **Electrical Actuators:** They are the most common actuators seen in the robots. They are the fastest actuators in whole actuator family and require high accuracy and repeatability. These features make electrical actuators more reliable and controllable. However, they are the more expensive than pneumatic solutions and complicated to install. They compose of DC, AC and stepper motors (CLR, 2018).

1.2.7. Actuation Systems in Light-weight Collaborative Robots

It is possible to find a wide variety of examples of actuation systems when lightweight collaborative robots are analyzed. Unfortunately, the hydraulic actuation systems are not one of these systems. They are suitable for the applications that require high speed and heavy load. Still, there are micro-hydraulic actuators to be used in lightweight collaborative robots.

Although the number of pneumatic actuators is greater than the hydraulic actuators, they have some drawbacks. It is hard to control the position precisely because of their nonlinear nature. Also, they are slow systems to respond to torque changes. They are not suitable for lightweight collaborative robots as their size considered. However, they become attractive to lightweight cobots since they provide the required torque with low inertia and friction. In general, pneumatic and electrical actuators form hybrid actuators.

The most common types of actuators in lightweight cobots are electrical actuators. Because of safety and performance limitations, electrical actuators prefer. Easiness of control, compliant natures, providing high precisions and being small in size catch the actuators on. All of these actuation systems will be explained in detail in the literature survey section.

1.3. Aim of the Thesis

The main aim of the thesis is the analysis and modeling of an actuation system to be used in a light-weight collaborative robot and its experimental verification. For this purpose:

- An actuation system that is in use in a collaborative robot is configured,
- The actuation system is modeled,
- The model is verified through experimentation.

Collaborative robots are the new approach in industrial automation. Actuator system design is an active field of research in the design of collaborative robots. As it is stated above, electrical actuation systems are widely used in lightweight collaborative robots. A Brushless DC motor and a planetary gear with high reduction are preferred as an actuation system in cobots due to the reasons that this actuation system combination has almost zero backlash and high torque density in low volumes.

1.4. Thesis Outline

This thesis consists of 5 chapters:

In chapter 2, the literature survey on collaborative robots is given. Joint types of collaborative robots are investigated in two parts: patented cobots and cobots in scientific studies. Typical joint components of cobots and their models are researched.

In chapter 3, the methodology is presented by introducing the test setup and simulation setup. Modeling of the proposed system is given in detail.

In chapter 4, results are exhibited by providing the comparison between experimental and theoretical calculations.

In chapter 5, the results are discussed and conclusions are addressed along with the summary of the thesis and future works.

CHAPTER 2

LITERATURE SURVEY

Nowadays, traditional industrial robots can be described as heavy, expensive, not suitable for multitasking and they are dangerous systems for humans in the same work environment. Due to these reasons, they fail to satisfy the changing needs of industry. Consequently, industrial robots do not meet the requirements of small and medium enterprises (SMEs) since they need to be modifiable, safe and high ROI (return on investment) systems. At this point, developing collaborative robots hit the spot (Appo, 2018). Light-weight industrial robots are an active field of research and it seems they revolutionize many industrial processes (Bogue, 2016). They are called collaborative robots or in short, cobots. The most significant feature of them is working directly with people in cooperation. Their advantages over traditional industrial robots are:

- Low costs and saving space as a result of removing safety fences;
- Easy to programme which enables faster implementation of functions;
- Short repayment period due to higher productivity and lower costs.

Although cobots receive a higher demand in the industry, there are still many difficulties to overcome. In accordance, actuation systems of these robots must be taken into consideration. In the following sections, actuation systems and their components used in light-weight collaborative robots are investigated in order to propose a suitable solution to model an actuation system to be used in modeling cobots.

2.1. Types of Actuation Systems for Cobots

Human-centered robotics requires direct cooperation between the human operator and the robot manipulator. Bandwidth, the capability to exerting maximum force and torque, and accessibility of workspace are indispensable performance metrics required in such applications. In brief, these systems not only focus on safety requirements but also satisfy the performance criteria needed in the industry (Zinn et al., 2004). In this context, actuation systems must be examined carefully. Hydraulic actuators have the highest torque and power output capabilities over their counterparts. So, they exhibit high

stiffness and are not suitable for safety required applications. Pneumatic actuators are very compliant systems which guarantee an inherent safety. However, they fail to achieve high bandwidth capabilities. As a result, electromagnetic actuators are the major actuation technology used in collaborative robots instead of hydraulic and pneumatic ones. New electromagnetic actuator based approaches have been introduced to fulfill the safety and performance requirements of collaborative robots. These approaches take place in the literature as follows:

1. Joint Torque Controlled Actuation
2. Series Elastic Actuation (SEA)
3. Distributed Macro-Mini Actuation (DM2)
4. Hybrid Pneumatic-Electric Actuation (HPEA)

2.1.1. Joint Torque Controlled Actuation

In this kind of actuation approach, actuation systems should be capable of providing accurate joint torques since force and motion are controlled in parallel. On the other hand, these capabilities are highly limited because of nonlinear effects such as cogging, backlash, and friction which are in the nature of electromagnetic based actuation systems used in industrial robots. In the study by D. Vischer and O. Khatib (1995), high-performance torque-controlled joints were investigated in the sense of sensor design and joint control. Although the designed sensor ensured high mechanical robustness, it was not sensitive to electrical noise. They used two manipulators to examine the control. Controllers were not compatible with the manipulators with different characteristics. These developments have shown that nonlinearities and friction inherited in the actuators should have been reduced in order to achieve high performance in joint torque control.

One of the first collaborative lightweight robots design was DLR's LWR I with joint torque controlled actuation. DLR's light-weight robot LWR I shown in Figure 2.1 with 7-DoF and kinematic redundancy is developed as a light-weight robot arm (Hirzinger et al., 2000). Its weight and payload capability are 18 kg and nearly 9 kg, respectively. It was not suitable in terms of safety with its 1:600 reduction provided by the double-planetary gear system. Also, it did not fully satisfy the robustness condition and had complexity due to its inductive torque sensing.

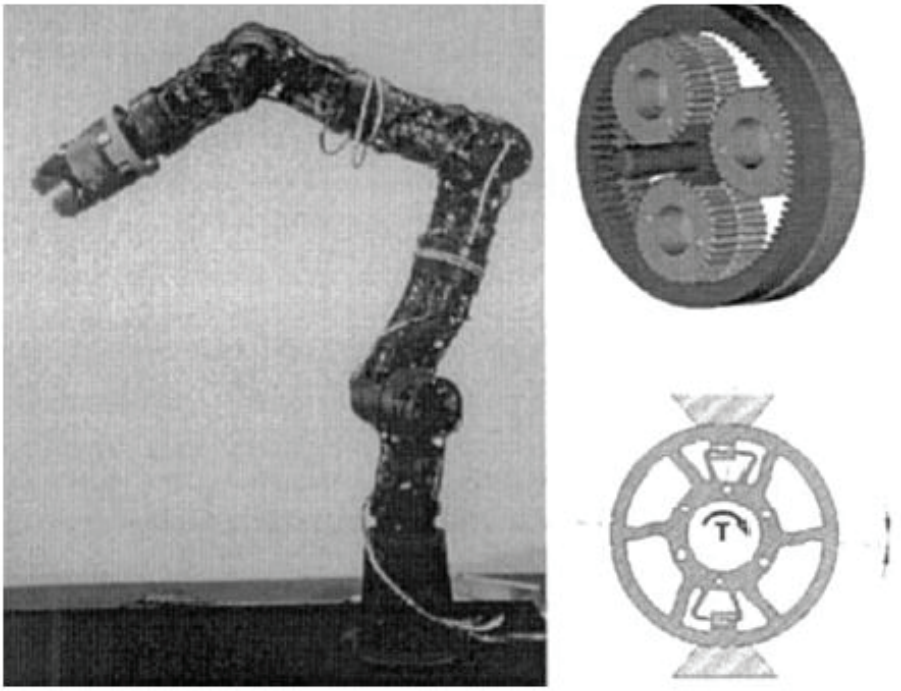

Figure 2.1. DLR's LWR I with double-planetary gears and inductive torque sensing (Source: Hirzinger et al., 2000)

LWR II is also developed in DLR's robotics laboratory. The parts of the designed multi-sensory joints are presented in Hirzinger et al. (2001). The multi-sensory design is implemented on each joint which is composed of a torque sensor, a link position sensor, and a motor position sensor in addition to a brushless DC Motor, a harmonic drive gear, and an electromagnetic brake, which are shown in Figure 2.2. The integrated joint torque sensors allowed implementation of complex control algorithms like force, vibration damping and stiffness control. However, some modifications on the joint structure such as reducing weight by using lighter components and materials were still required.

In the work by Hirzinger et al. (2004), a new modular arm concept is introduced. They aimed to design a fully modular system which includes only mechanical and electronic parts. Thus, it was aimed to configure different types of joints in a short span of time. Another objective of the design was reducing the motor's weight and power losses. Finally, they came up with high-energy providing ROBODRIVE motors which reduced the weight and power losses by half. LWR III has been developed by using these ROBODRIVER motors.

In the study by Albu-Schäffer et al. (2007), a new generation torque-controlled light-weight robot, DLR LWR, is presented. The main aim was to develop a light-weight

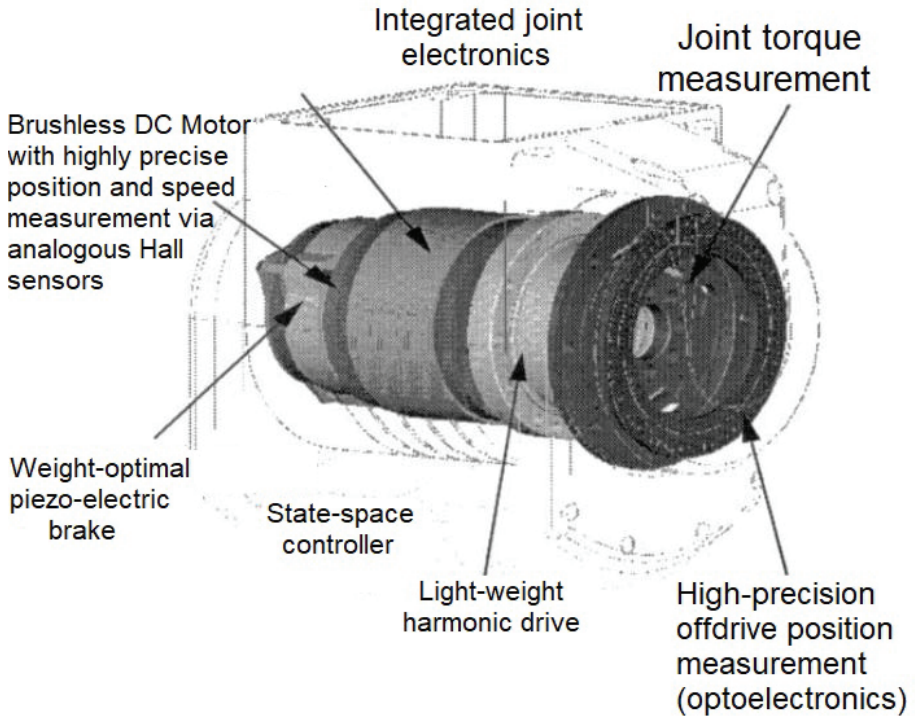

Figure 2.2. Intelligent joint

(Source: Hirzinger et al., 2001)

robot that resembles the human arm's kinematic redundancy and has a high payload to weight ratio. At this stage, they developed a robot with 7-DoF, which has a 15 kg weight and almost 15 kg payload capacity. The capability of nearly 1:1 payload to weight ratio is ensured by using new motor technology and light-weight harmonic drives providing high power density. In addition to torque sensors, link position and motor position sensors are used in each joint, and it enables the robot to be used both in assembly, and manufacturing fields with direct cooperation with a human operator safely. Also, cross roller bearings enable to decouple disturbing forces and torques. Joint level control is performed by a signal processor in each joint, and not only the robot dynamics but also the Cartesian control is implemented by a central computer. The LWR technology transfer to KUKA has paved the way for these robot arms in the market. The modular joint design is shown in Figure 2.3.

The technology transfer between the DLR and KUKA showed better results with the improved version, the LWR4, as it is compared with previous versions. Some modifications in gear units and cable channel are made, and they came up with a device which is cheaper, easier to use and more reliable. Also, servo control and joint control software

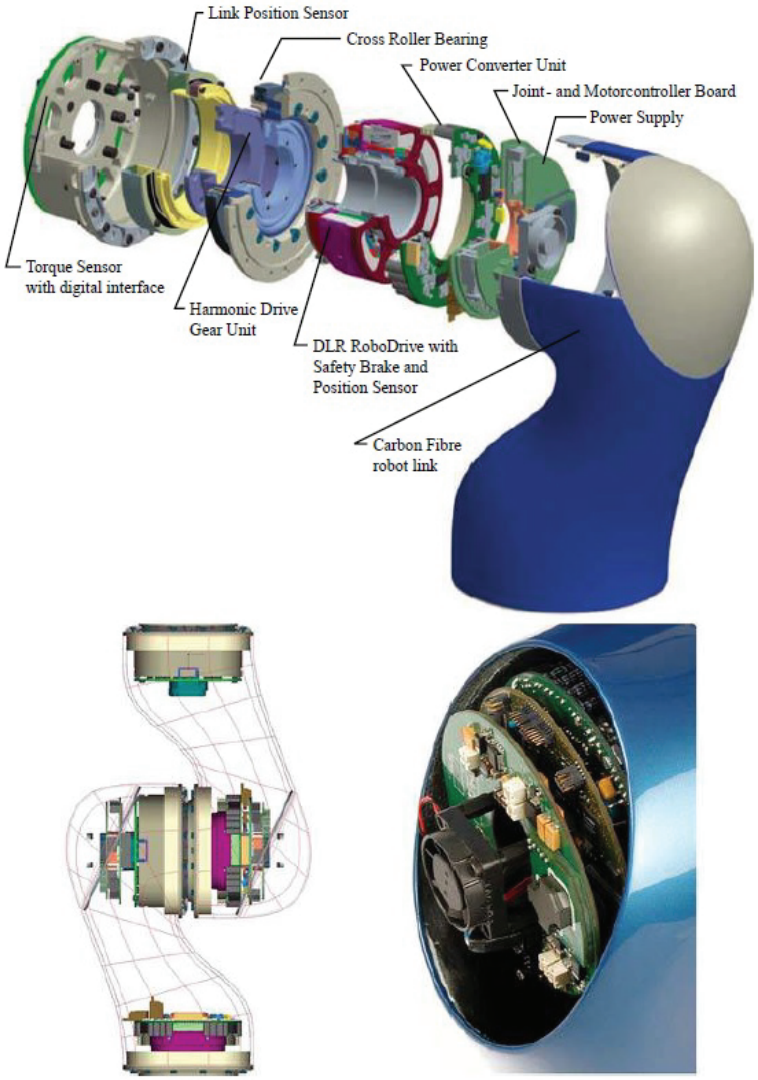

Figure 2.3. The overall design of LWR joint

(Source: Albu-Schäffer et al., 2007)

are revised, and the latencies are significantly reduced. The user-friendliness of the robot is improved by introducing some new software such as virtual walls and contact detection (Bischoff et al., 2010). Some applications of LWR are as follows:

- *DESIRE - Mobile dual arm robot with 4-finger hands:* It is a BMBF sponsored project shown in Figure 2.4 (a). In order to integrate the robots into common usage, it is aimed to boost the capability of manipulating and perceiving the objects.

- *SMErobot - The worker's third hand:* It is an EU-funded project shown in Figure 2.4 (b). It is aimed to make the pieces ready for the human operator to perform welding tasks.

- *PHRIENDS - Safe human-robot interaction:* It is also an EU-funded project shown in Figure 2.4 (c). Physical contact is studied and evaluated by the results obtained from SMErobot project. It is probably the first steps for sharing workspace by a human operator and a robot.

- The first industrial applications involved placing rubber closures in manufacturing shown in Figure 2.4 (d). Also, at Machine Tool World Exposition (EMO) trade fair 2007, machine loading and unloading operation is presented as shown in Figure 2.4 (e).

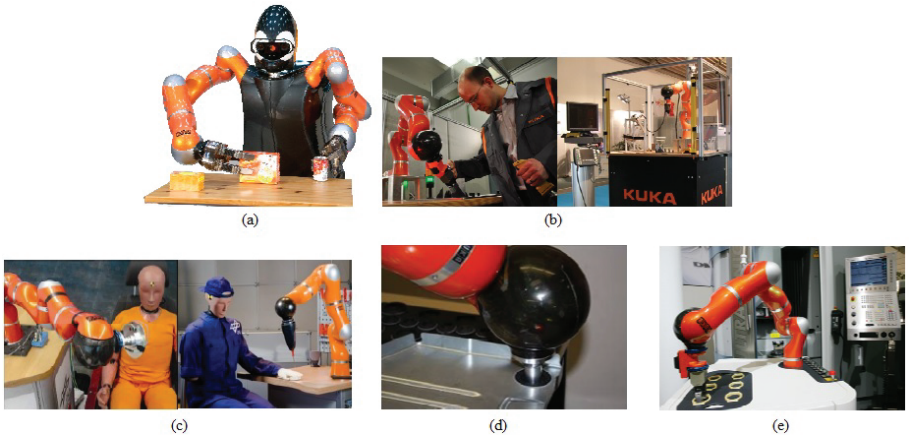

Figure 2.4. (a) DESIRE technology, (b) SMErobot's welding operation, (c) Safety demonstration of PHIRENDS, (d) Manufacturing scenario by placing rubber closures, (e) loading/unloading machine (Source: Bischoff et al., 2010)

Another low-cost robot arm Franka Emika (2018) is has a similar modular actuation-sensor components as drives of the robot (Rader et al., 2017). Universal Robots (2018) and Kinova (2018) which are promising commercially available collaborative robot arms, they also use compact sensor-actuator units with the similar structures.Additionally, UR and ABB Yumi are actuated by brushless DC motors, and they can be controlled either by joint torque control or joint impedance control methodologies (Haddadin et al., 2017).

2.1.2. Series Elastic Actuation (SEA)

In high impedance actuators (e.g., traditional geared electromagnetic actuators) there is a trade-off between high torque density and reflected inertia which is amplified

by the square of gear reduction. It results in a lack of safety thus an elastic element is attached between the output of the actuator and the link of the robot arm. These systems are called series elastic actuators or shortly, SEA (Zinn et al., 2004). The main advantage of series elastic actuators is low output impedance which corresponds to compliance or safety, in the provided frequency spectrum. The high-frequency impedance is limited by the placed elastic element, and the low-frequency impedance is restricted by adding a linear feedback system to the output of the actuator. The topology of the SEA is as shown in Figure 2.5.

Although there are similarities between the topologies of SEA and joint torque control actuation, control schemes of these approaches differ. A high gain PD controller is suitable for the SEA with low stiffness. However, it is not suitable for the joint torque controlled actuation because of its stiff nature.

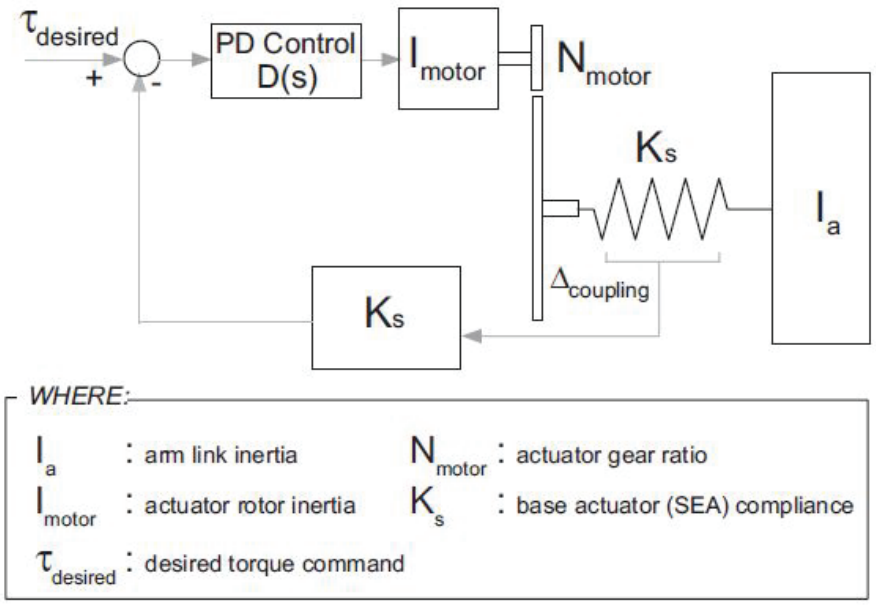

Figure 2.5. Series elastic actuation topology

(Source: Zinn et al., 2004)

In the study by Lens et al. (2010), mechanical design of the BioRob robot arm shown in Figure 2.6 (a) is evaluated and its solutions in the market are investigated. BioRob robot arm is inspired by the elastic muscle tendon equipment in which joints are composed of DC motors with four cables and springs to provide elasticity. Also, in addition to the sensors that measure the motor shafts' angular position and angular joint/link position sensors are employed to enhance Cartesian space positioning accuracy.

As it is compared with its counterparts, BioRob robot arm has low mass and inertia with similar speed and reachable range characteristics. Thus, the kinetic energy is minimized, and the robot arm is made safe even collision detection is not used. It is suitable for pick and place operations as shown in Figure 2.6 (b) with a maximum payload of 0.5 kg and it has relatively lower power consumption.

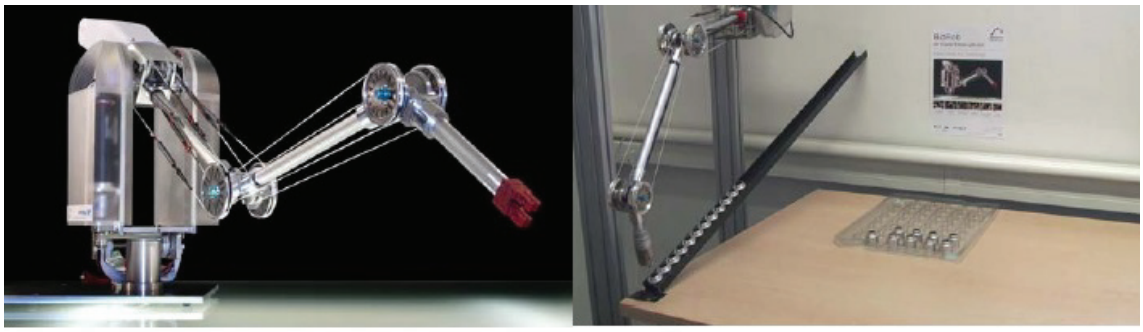

(a) (b)

Figure 2.6. (a) BioRob-X4 demonstrator, (b) Pick and place operation
(Source: Lens et al., 2010)

A new actuation concept, Series-Parallel Elastic Actuation (SPEA), is introduced in the work by Mathijssen et al. (2014). The problem tackled in this study is the stress on the motor when it is coupled to the load in series. Another problem is the use of inefficient gears which results in increasing the total weight of the robot and energy losses due to high reduction ratios when DC motors with low torque capabilities are used. In SPEA concept, shown in Figure 2.7, springs are positioned in parallel, and every spring could be tightened and fixed the joint. The rotational input is converted to two sequential phases which are motion and dwell phases. In the motion phase, the output is in motion. On the other hand in dwell phase, input rotates without any constraint while the output is blocked. Each spring in parallel can be in pretensioned, unpretensioned or, pretensioning states. Since each spring can be locked in any state, the stress on motor reduced. The SPEA concept is implemented with two prototypes with different mechanisms. Although it reduced the motor torque, energy efficiency is increased.

In the study by Fernández et al. (2016) which is conducted within the framework of the European project FourByThree, it is aimed to combine two formerly used concepts. One of them is active compliance control in which joint torques are estimated by using a dynamic model and motor currents. The other is using passive elastic elements which not only provides safety due to the intentional or unintentional contact but also estimates torque values. In the embedded electronics part, three motor current sensors are used.

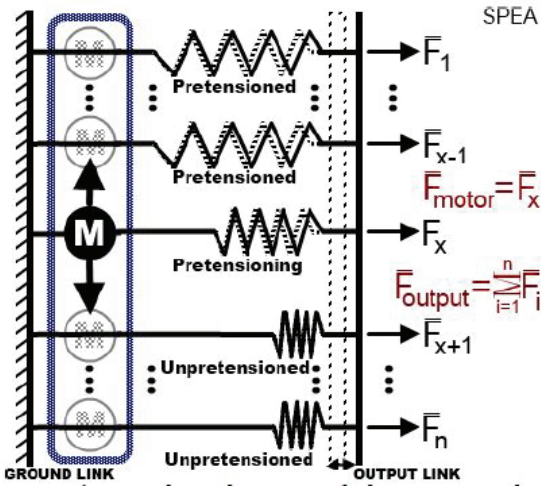

Figure 2.7. The schematic of SPEA with n parallel springs

(Source: Mathijssen et al., 2014)

Absolute encoders with high resolutions are placed before and after the gear to measure the motor position and gear's output shaft position. An additional absolute encoder is placed after the elastic element to measure link position.

The 28Nm-actuator shown in Figure 2.8 (a), is originated from the former design of the project CAPIO7 in which an elastic element was used. This element composes of small disc springs, shown in Figure 2.8 (b), that are placed at both sides of shaft which rotates with the motor's output shaft.

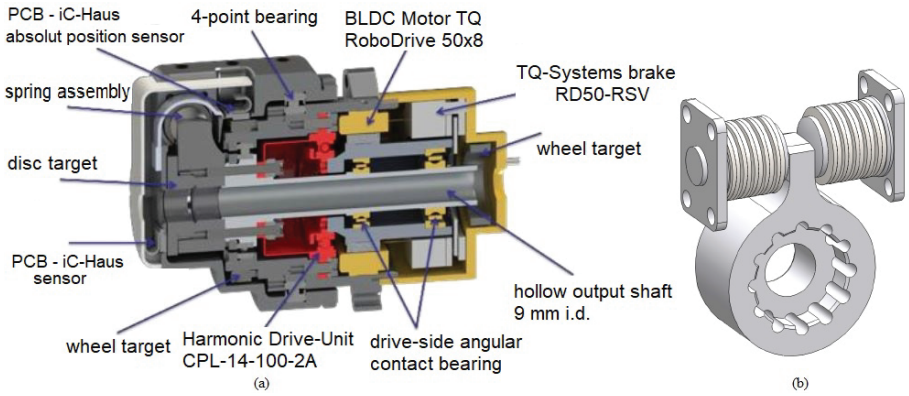

Figure 2.8. (a) Series elastic actuator type I: 28Nm, (b) Elastic element with spring discs (Source: Fernández et al., 2016)

In 50Nm-actuator shown in Figure 2.9 (a) design case, coil type springs are developed as elastic elements. The spring coupling shown in Figure 2.9 (b) has shown linear

characteristic in terms of desired stiffness, within a range of $5\,^{\circ}$s. Then, a subtle increase in stiffness is displayed. It is aimed to prevent the spring not to reach a fully compressed state at the maximum torque. For this reason, second spring is used and operated after 5 $5\,^{\circ}$ of compression.

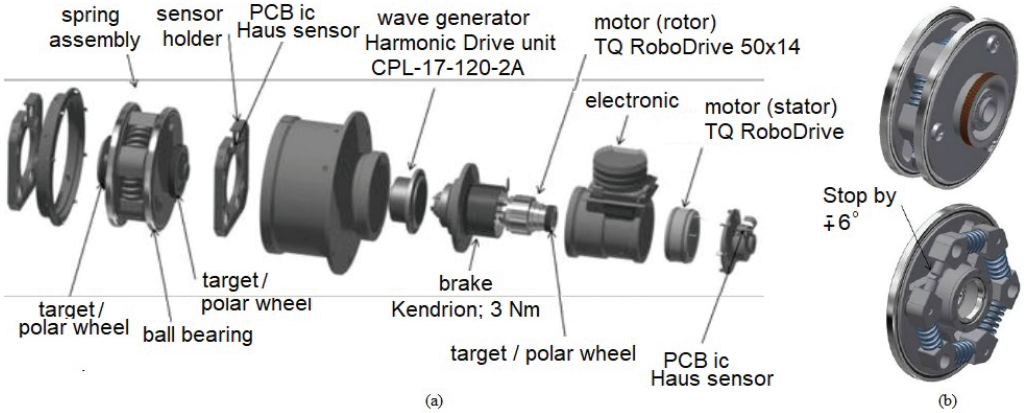

Figure 2.9. (a) Series elastic actuator type II: 50Nm, (b) Elastic element with coil springs (Source: Fernández et al., 2016)

In the study by Bodie et al. (2016), a manipulator named ANYpulator is developed in order to provide safe interaction between robots and their environments. The effective inertia at the output is reduced by decoupling the gearbox and output with an elastic element. Also, contact force control method is used in this work and this method limits the forces with the environment.

ANYdrive joint structure shown in Figure 2.10, is the actuation systems of ANYpulator. These structures are constructed as modular structures which include brushless DC motors, backlash-free harmonic drive gears and torsional springs. In addition to these, there are absolute encoders with 17 bit resolution in each module which not only calculates output position but also measures spring deflection.

Besides these actuators, the commercial Baxter and Sawyer robots are composed of series elastic actuators. In their actuation systems, there are motors and gearboxes to drive the elastic spring element which drives the joint (Guizzo and Ackerman, 2012). Actuators exhibit more compliant and less stiff features. Also forces are measured by measuring the deflections of the springs.

Figure 2.10. ANYdrive robot joint

(Source: ANYbotics, 2018)

2.1.3. Distributed Macro-Mini Approach (DM2)

In addition to above-mentioned approaches, Distributed Macro-Mini Actuation, has been developed. In the study by Zinn et al. (2004), Distributed Macro-Mini Actuation is introduced to overcome the safety and performance restrictions of joint torque controlled and series elastic actuation, respectively. Thus, this approach is the combination of previous methods. In the Distributed Macro-Mini Actuation or shortly DM2 approach, shown in Figure 2.11., there is a couple of actuators parallel to each other and they are placed in specific locations on the manipulator. The main benefit of this actuation system is to reduce both the reflected inertia of the actuator and the whole weight of the manipulator. The torque generation is divided into two components which differ from each other in terms of their frequency span. Hence, the required torque is distributed to these actuation components on the robot arm (Zinn et al., 2004).

In the first part of the approach shown in Figure 2.11 (a), torque is generated by two components as it is mentioned above and the torque sums in parallel. The main advantage of this part is related to the position or force control and disturbance rejection tasks which require low-frequency position tracking and high-frequency torques, respectively. In the second part of the approach shown in Figure 2.11 (b), it is aimed to divide the low-frequency and high-frequency actuators among the robot arm. Thus, the contributions of actuators will be impedance minimization and control bandwidth maximization according to their locations. For this purpose, series elastic actuator, the low-frequency component,

is located far away from the actuated joint since its magnitude contribution is larger than the high-frequency component. So, the SEA is located at the base and provides considerable reduction in inertia and weight of the manipulator. By locating the high-frequency components closer to the joints causes generation of high-frequency torque.

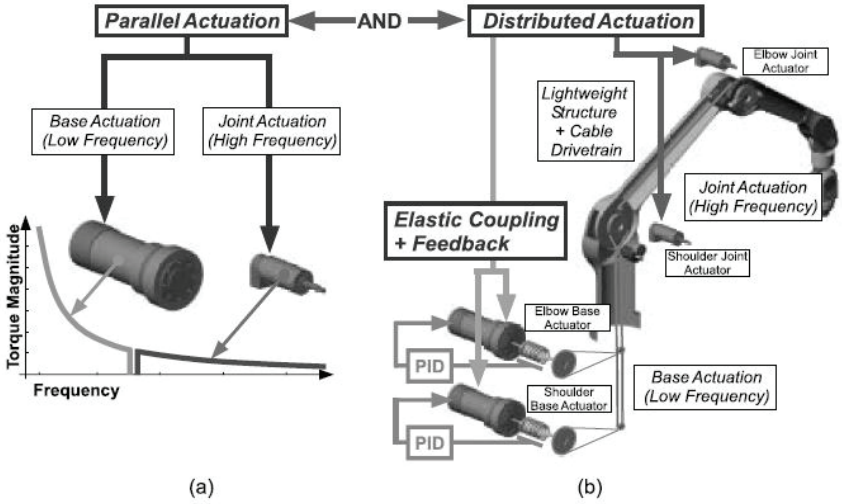

Figure 2.11. DM2 approach (a) Dividing of torque into parallel actuators, (b) Low-frequency components are placed far away from the actuated joint; high-frequency components are placed at the actuated joint (Source: Zinn et al., 2004)

In the study by Shin et al. (2010), a human-friendly one DoF elbow with DM2 actuation approach is developed. It is a revised version of Stanford Safety Robot (Stanford Robotics, 2018), S2p, which exhibits compliant characteristic in addition to high power by pneumatic artificial muscles. In its composition, mini electrical actuators, pressure regulators and plastic links are used as shown in Figure 2.12.

In their work, instead of two larger pneumatic muscles used in S2p, four pneumatic muscles are used. Thus, both response time and reachable space characteristics are improved. By the modification of pressure regulators with proportional valves, the actuators are controlled swiftly and smoothly. The system components without pneumatic muscles are surrounded by a thin-walled structure, thereby light-weight and robust design is established. When this design is compared with previous pneumatic muscles alone structure, system performance is considerably improved due to reducing link length and enlargement of the diameter of the link. In this way, back pressure is minimized, and the length of the air path is reduced.

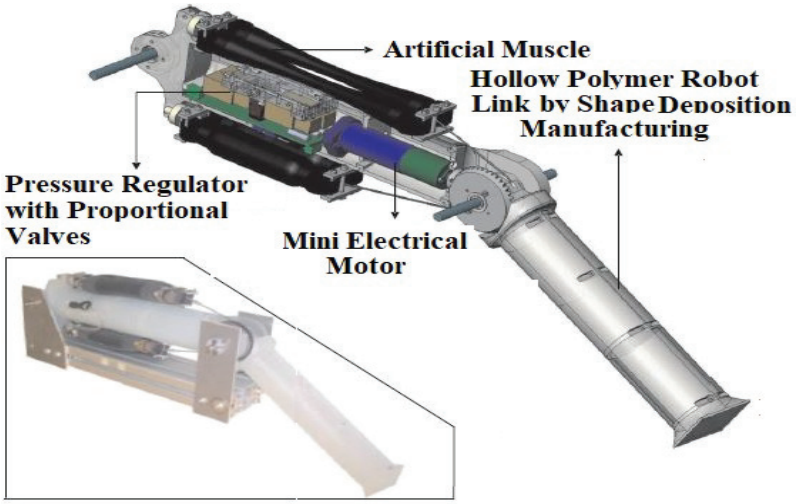

Figure 2.12. Developed DM2 actuator design

(Source: Shin et al., 2010)

2.1.4. Hybrid Pneumatic-Electric Actuation (HPEA)

At the end of the 20th century, electric actuators are the mainstream in robotics since they have advantages like accurate control, clean operation, and easy implementation, over other actuators. However, they are not suitable for their oversize and heavy structure for large power applications. At this point, pneumatic actuators are a reasonable approach that provided higher power at low weights, better compliance, high speed and different transmission techniques with a simple design. As a result, they could be used in an industrial application due to their light-weight and compact design characteristics.

In the study by Takemura et al. (2000), a pneumatic-electric hybrid motor is constructed as shown in Figure 2.13. The main actuation element in the construction is the pneumatic motor while the electric motor is used as a stabilizing device. Motors are mechanically coupled to each other in parallel. In order to magnify torque and provide higher power to weight ratio, a reduction gear between the shaft of vane-type pneumatic motor and the output shaft is used.

In the study of Shin et al. (2008), engineers made a contribution to the Stanford Human Safety Robot (Stanford Robotics, 2018) by designing distributed compact pressure regulator. They aimed to propose a hybrid actuation approach to design a robot arm that is comparable with the human arm. As it is explained in the previous section, Stanford Human Safety Robot is actuated by distributed macro-mini approach. What is new

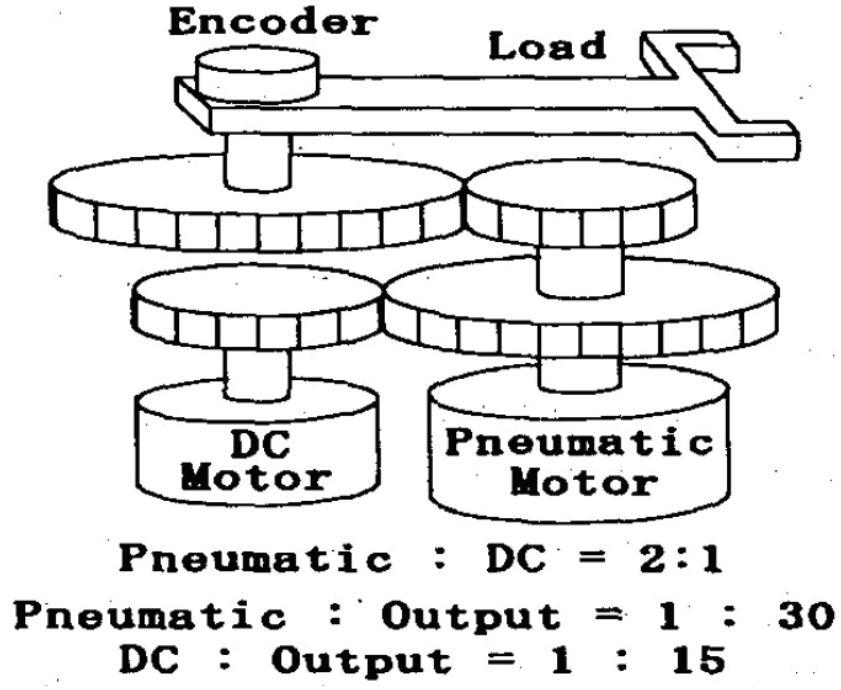

Figure 2.13. Construction of pneumatic-electric actuator

(Source: Takemura et al., 2000)

in this study is the compact pressure regulator. It has a compact design which composed of a solenoid valve, a manifold, a pressure sensor, and a driving circuit as shown in Figure 2.14.

In this design, the valve's flow rate depends on both the orifice dimension and differential pressure across the valve. The pressure difference between pneumatic muscle and compressor is quite higher than the difference between pneumatic muscle and atmosphere. It makes pressuring rate greater than the exhaust rate. This unbalanced flow rate results in oscillations in the arm due to the pressurizing and depressurizing. To overcome this problem, they are inserted a depressurizing valve. Furthermore, the complicated piping structure is prevented by the manifold design. It also decreases the air flow resistance with its compact design.

In the study by Bone and Chen (2012), they propose a novel hybrid actuator for robotic applications. They have used a pneumatic cylinder and a DC motor which work in parallel to each other. Also, they prevent using high ratio transmission system to reduce the joint friction and its dangerous effects. As shown in Figure 2.15, the pneumatic cylinder moves vertically and drives the rack gear and the linear slide. The DC motor drives a pinion gear. Instead of using rotary pneumatic motor mentioned in the Takemura et al.,

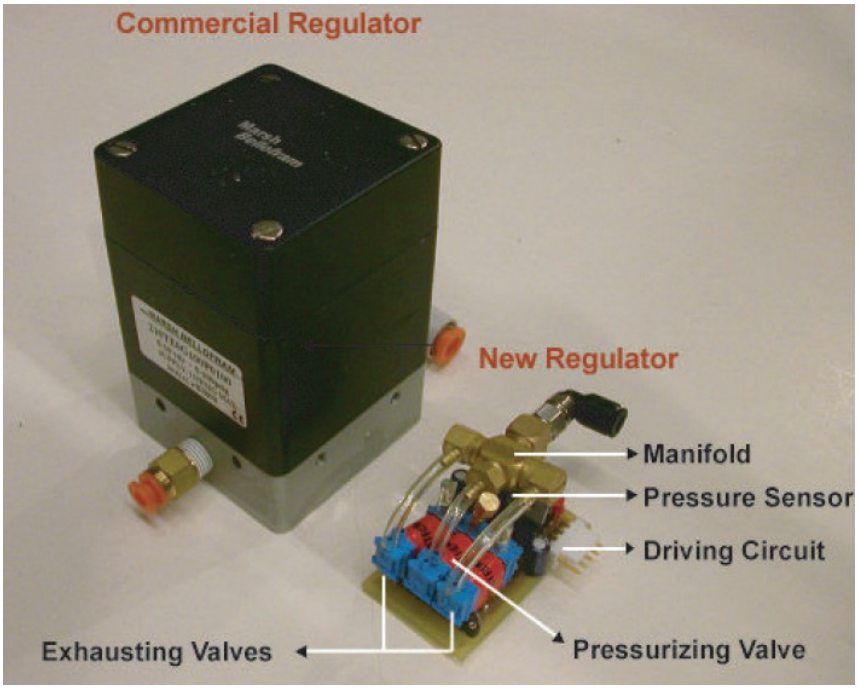

Figure 2.14. The pressure regulator

(Source: Shin et al., 2008)

2000's study above, Bone and Chen use pneumatic cylinder since they cause less friction than pneumatic motors. Also, the friction torque caused by high ratio transmission systems is diminished by using pinion and output gears. Another advantage of the design is making the area of the piston greater than the area of the rod side. Thus, the maximum pneumatic forces cope with the gravity force that acts on the arm.

In the study of Ashby and Bone (2016), they present a novel rotary hybrid pneumatic-electric actuator (HPEA) that is suitable for collaborative applications. It has various advantages over the prior HPEAs. The design is mainly composed of four pneumatic cylinders parallel with a small DC motor as shown in Figure 2.16. In this design, the electric motor is connected directly to the output shaft instead of gears in previous studies by Takemura et al. (2000), Shin et al. (2008) and, Bone and Chen (2012). Thus, friction and backlash are eliminated by ruling out the gears. Also, mechanical impedance is not amplified by high gear ratios. In the study of Bone and Chen (2012), the angle of the output shaft was measured by inferring the piston's position or an encoder coupled to a gear. However, it is measured directly in this design and provides a more precise measurement. Moreover, as it is compared with the work of Shin et al. (2008), although the design is less compact, it allows both retraction forces and pneumatic extensions to transmit the pneu-

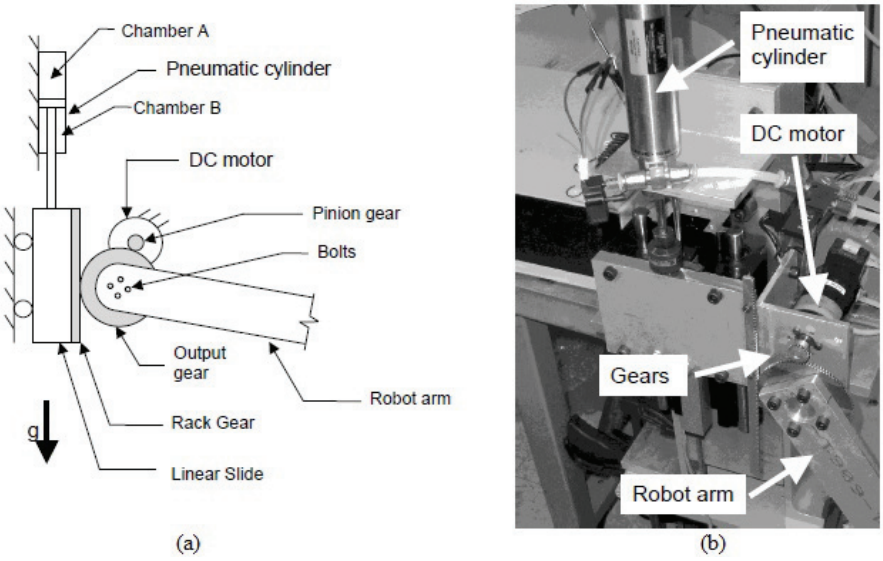

Figure 2.15. The hybrid actuator design

(Source: Bone and Chen, 2012)

matic power instead of using only retraction forces. Furthermore, by using low friction pneumatic cylinders instead of a rotary pneumatic motor or pneumatic artificial muscles, position control is improved, and energy losses due to friction are diminished as it is compared with the studies of Takemura et al. (2000) and Shin et al. (2008). The comparison between the new HPEA and previous designs are tabulated in Table 2.1.

Table 2.1. Comparison of new HPEA's (Source: Ashby and Bone, 2016)

Specifications	Takemura et al. (2000)	Shin et al. (2008)	Bone and Chen (2012)	New HPEA
Maximum continuous torque (Nm)	10.9	7.1	10	37.7
Ratio of motor torque to load torque (%)	14	14	10	3
Static friction torque at output shaft (Nm)	>9.7	N/A	0.1	0.23
Moment of inertia at output shaft (kgm^2)	$>1.5 \times 10^{-3}$	$>9.1 \times 10^{-4}$	6.4×10^{-5}	2×10^{-3}

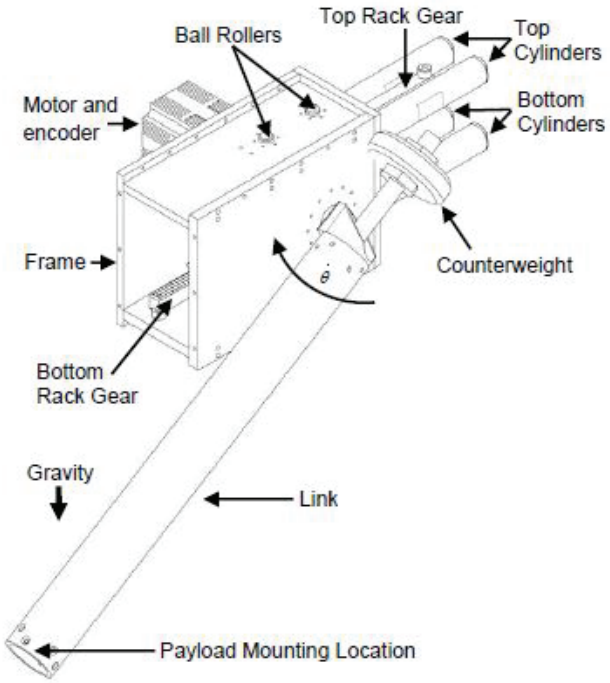

Figure 2.16. The rotary hybrid actuator

(Source: Ashby and Bone, 2016)

2.2. Typical Components of the Actuation Systems for Cobots

The actuation system approaches are investigated in the previous section in detail. In this section, the components of the actuation systems are discussed to choose the efficient configuration to be modeled. Types of motors, transmission systems, and sensors and their dynamic equations are introduced in the next sub-sections.

2.2.1. Electric Motors

A motor is an indispensable part of an actuation system to drive the joints. Although there are pneumatic systems proposed for collaborative robots, electrical motors are generally used in light-weight collaborative robots as stated in the previous section. Types of electrical motors and their mathematical models are stated below.

2.2.1.1. DC Motors

The main parts of DC motor are rotor and stator. The armature is placed on the rotor in a brushed DC motor while the stator with magnetic poles is made of specific windings or stationary magnets. The current is induced in the rotor windings via brushes which stay in touch with the copper tapes at the end of the rotor. The copper tapes are commutator strips which are attached to the windings of the rotor. The transverse section of a two pole DC motor is as shown in Figure 2.17.

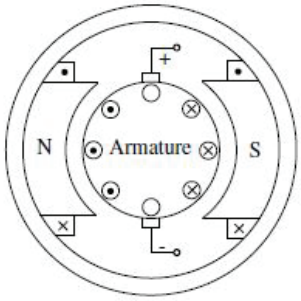

Figure 2.17. The transverse section of a two pole DC motor

(Source: Sen, 1997)

When the motion of the rotor occurs, the brushes move among the strips. So, the current flows along the conductors. According to these, force vectors are constituted on the rotor windings which are tangential to the outer surface of the rotor. As a result, torque is generated. DC motors operate by a DC voltage source. The speed generation in a DC motor is a straightforward action which is regulated by varying the supply voltage. To increase the efficiency, solid-state converters like controlled rectifiers and choppers shown in Figure 2.18, are used. Variations of DC voltage is obtained from rectifiers. In addition, choppers are composed of switches which turn the motor at a high rate. Current is induced as the superposition of on and off states of the switch shown in Figure 2.19.

The equivalent circuit of a DC motor is shown in Figure 2.20. Vs, i, R and L are DC supply voltage, armature current, resistance, and inductance, respectively. The back-emf is denoted by e. The motor can be modeled mathematically according to Equation 2.1 and 2.2.

$$V_s = Ri + L\frac{\mathrm{d}i}{\mathrm{d}t} + e \tag{2.1}$$

$$T_e = k_f\omega_m + J\frac{\mathrm{d}\omega_m}{\mathrm{d}t} + T_L \tag{2.2}$$

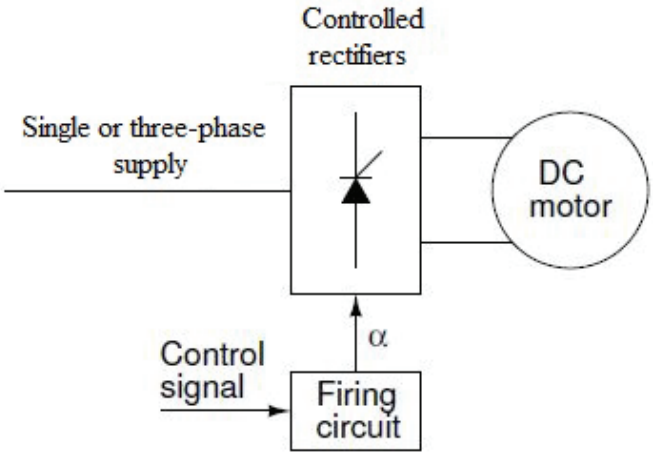

Figure 2.18. DC motor operation by varying DC voltage

(Source: Sen, 1997)

where T_e, k_f, J, T_L are the electrical torque, friction constant, inertia of the rotor and the load torque, respectively. Electrical torque and back-emf are formulated as shown in Equation 2.3 and 2.4:

$$e = k_e \omega_m \tag{2.3}$$

$$T_e = k_t \omega_m \tag{2.4}$$

where k_e and $k_t$are back-emf constant and torque constant, respectively. In order to model the DC motor, Equation 2.1 and 2.2 can be reformulated as follows:

$$\frac{\mathrm{d}i}{\mathrm{d}t} = -\frac{R}{L}i - \frac{k_e}{L}\omega_m + \frac{1}{L}V_s \tag{2.5}$$

$$\frac{\mathrm{d}\omega_m}{\mathrm{d}t} = \frac{k_t}{J}i - \frac{k_f}{J}\omega_m - \frac{1}{J}T_L \tag{2.6}$$

The mathematical model of the DC motor can be obtained in state-space approach as follows:

$$\begin{bmatrix} \dot{i} \\ \dot{\omega}_m \\ \dot{\theta}_m \end{bmatrix} = \begin{bmatrix} -\frac{R}{L} & -\frac{k_e}{L} & 0 \\ \frac{k_t}{J} & -\frac{k_f}{J} & 0 \\ 0 & 1 & 0 \end{bmatrix} \begin{bmatrix} i \\ \omega_m \\ \theta_m \end{bmatrix} + \begin{bmatrix} \frac{1}{L} & 0 \\ 0 & -\frac{1}{J} \\ 0 & 0 \end{bmatrix} \begin{bmatrix} V_s \\ T_L \end{bmatrix} \tag{2.7}$$

$$\begin{bmatrix} i \\ \omega_m \\ \theta_m \\ T_e \end{bmatrix} = \begin{bmatrix} 1 & 0 & 0 \\ 0 & 1 & 0 \\ 0 & 0 & 1 \\ k_t & 0 & 0 \end{bmatrix} \begin{bmatrix} i \\ \omega_m \\ \theta_m \end{bmatrix} \tag{2.8}$$

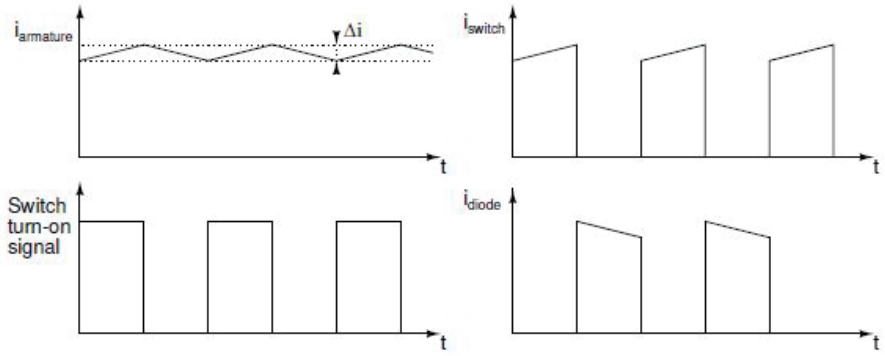

Figure 2.19. Current waveforms in a chopper

(Source: Harnefors, 2002)

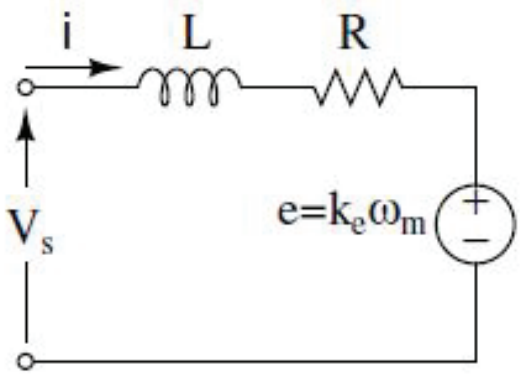

Figure 2.20. DC motor equivalent circuit

(Source: Harnefors, 2002)

2.2.1.2. Brushless DC Motors

A brushless DC motor as the name implies is a DC motor without brushes and the commutators. To control the armature currents, it has position sensors and an inverter. It is an electronically commutated device instead of mechanical commutator used in traditional DC motors. They have various advantages such as higher efficiency and speed ranges, better speed-torque characteristics, long operation life and, noiseless operation over traditional DC motors. Brushless DC motor or in short, BLDC motors, can be either be a trapezoidal type or sinusoidal type. It is caused by the shape of the induced back-emf on the stator windings. Trapezoidal type BLDC motors must be supplied with quasi-square currents to prevent torque ripples. On the other hand, sinusoidal type BLDC

motors must be supplied with sinusoidal currents for the same purpose. As comparison between them, sinusoidal BLDC motors require complex structures since they need highly precise position detection continuously. In contrast, trapezoidal BLDC motors are cheap, efficient and simple compared to sinusoidal BLDC motors (Sen, 1997). Most of the BLDC motors are in three-phase configuration since this configuration offers an optimal combination of efficiency and minimized torque ripples. Also, it is reasonable for precise control and it requires electronic devices for the control of stator currents (Texas Instruments, 1997). The position detection is provided by three Hall sensors which are tiny magnets connected usually to rear end of motor's shaft as shown in Figure 2.21.

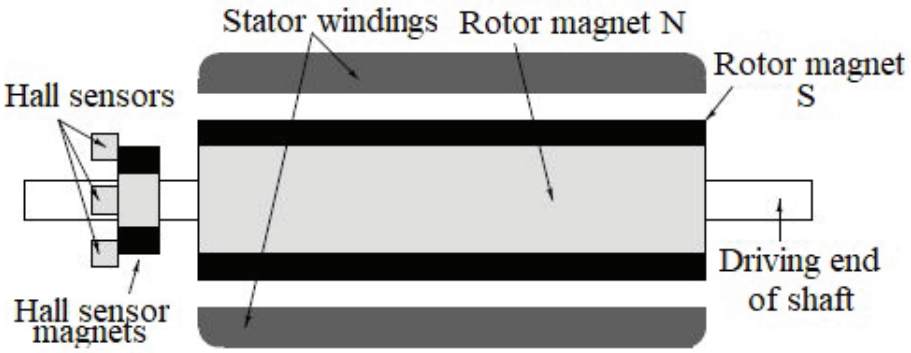

Figure 2.21. Cross-section of a BLDC motor

(Source: Yedamale, 2003)

In three-phase BLDC motor operation, two of the phases are in on-state while one of them is in off-state since two-phase generates the highest torque. Rotor position state change is sensed by three Hall-effect sensors in every $60\,^{\circ}$ as shown in Figure 2.22. In Figure 2.23, the cross-section of the three-phase BLDC motor and its energizing sequence is shown. Each $60\,^{\circ}$ interval starts when the gap between the stator and rotor field lines are $120\,^{\circ}$. The gap between the stator and rotor field lines are $60\,^{\circ}$ at the end of each interval. When the field lines are perpendicular to each other, maximum torque is provided. Current commutation is performed by a six-step inverter shown in Figure 2.24 which composed of MOSFET switches. The switching sequence, current directions and the states of Hall-effect sensors are tabulated in Table 2.2.

Table 2.2. Swithing sequence of BLDC motor

Switching interval	Seq. number	Pos. sensors			Switch closed		Phase Current		
		H1	H2	H3			A	B	C
0 °-60 °	1	1	0	0	Q1	Q4	+	-	off
60 °-120 °	2	1	1	0	Q1	Q6	+	off	-
120 °-180 °	3	0	1	0	Q3	Q6	off	+	-
180 °-240 °	4	0	1	1	Q3	Q2	-	+	off
240 °-300 °	5	0	0	1	Q5	Q2	-	off	+
300 °-360 °	6	1	0	1	Q5	Q4	off	-	+

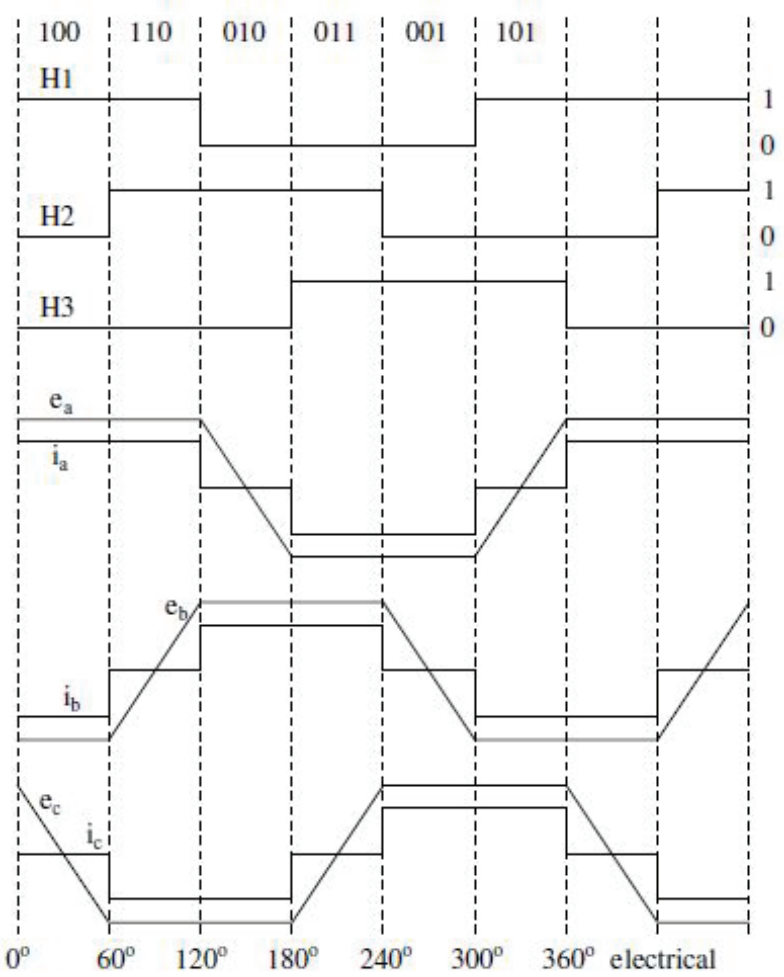

Figure 2.22. Ideal back-emfs (e_i's), phase currents and states of Hall sensors

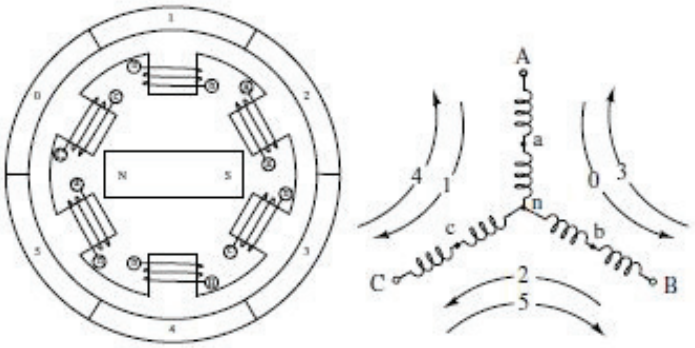

Figure 2.23. Transverse section of BLDC and energizing sequence

(Source: Brown, 2002)

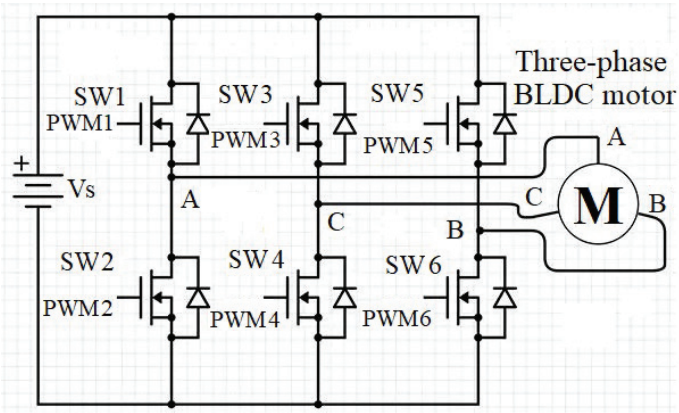

Figure 2.24. BLDC drive scheme

The mathematical model of the three-phase brushless DC motor is based on the following equations:

$$V_{ab} = R(i_a - i_b) + L\frac{\mathrm{d}i}{\mathrm{d}t}(i_a - i_b) + e_a - e_b \tag{2.9}$$

$$V_{bc} = R(i_b - i_c) + L\frac{\mathrm{d}i}{\mathrm{d}t}(i_b - i_c) + e_b - e_c \tag{2.10}$$

$$V_{ca} = R(i_c - i_a) + L\frac{\mathrm{d}i}{\mathrm{d}t}(i_c - i_a) + e_c - e_a \tag{2.11}$$

$$T_e = k_f\omega_m + J\frac{\mathrm{d}\omega_m}{\mathrm{d}t} + T_L \tag{2.12}$$

where a, b, and c denote phases and V, i, and e, represent phase to phase voltages, phase currents and phase back-emf voltages, respectively. T_e and T_L are the electrical and load

torque. R and L are phase resistance and inductance, respectively. J is the inertia of the rotor, k_f is the viscous friction constant and ω_m is the rotor speed. The phase back-emf voltages and the electrical torque is written as

$$e_a = \frac{k_e}{2}\omega_m Tr(\theta_e) \tag{2.13}$$

$$e_b = \frac{k_e}{2}\omega_m Tr(\theta_e - \frac{2\pi}{3}) \tag{2.14}$$

$$e_c = \frac{k_e}{2}\omega_m Tr(\theta_e - \frac{4\pi}{3}) \tag{2.15}$$

$$T_e = \frac{k_t}{2}[Tr(\theta_e)i_a + Tr(\theta_e - \frac{2\pi}{3})i_b + Tr(\theta_e - \frac{4\pi}{3})i_c] \tag{2.16}$$

where k_e and k_t are the back-emf constant and torque constants. θ_e is the electrical angle which is the multiplication of rotor angles and the number of pole pairs ($\theta_e = \frac{p}{2}\theta_m$). The function $Tr(.)$ is the trapezoidal waveform of the back-emf. The detailed formulation of the trapezoidal waveform is written as

$$e_a = \left\{ \begin{array}{cc} (6E/\pi)\theta_e & 0 < \theta_e < \pi/6 \\ E & \pi/6 < \theta_e < 5\pi/6 \\ -(6E/\pi)\theta_e + 6E & 5\pi/6 < \theta_e < 7\pi/6 \\ -E & 7\pi/6 < \theta_e < 11\pi/6 \\ (6E/\pi)\theta_e - 12E & 11\pi/6 < \theta_e < 2\pi \end{array} \right\} \tag{2.17}$$

$$e_b = \left\{ \begin{array}{cc} -E & 0 < \theta_e < \pi/2 \\ (6E/\pi)\theta_e - 4E & \pi/2 < \theta_e < 5\pi/6 \\ E & 5\pi/6 < \theta_e < 9\pi/6 \\ -(6E/\pi)\theta_e + 10E & 9\pi/6 < \theta_e < 11\pi/6 \\ -E & 11\pi/6 < \theta_e < 2\pi \end{array} \right\} \tag{2.18}$$

$$e_c = \left\{ \begin{array}{cc} -E & 0 < \theta_e < \pi/6 \\ -(6E/\pi)\theta_e + 2E & \pi/6 < \theta_e < \pi/2 \\ -E & \pi/2 < \theta_e < 7\pi/6 \\ (6E/\pi)\theta_e - 8E & 7\pi/6 < \theta_e < 9\pi/6 \\ E & 9\pi/6 < \theta_e < 2\pi \end{array} \right\} \tag{2.19}$$

The voltage equations 2.9 through 2.11 are the combinations of each other. By the help of the current relation formulated in Equation 2.20, voltage equations are reduced to two

equations as shown in Equation 2.21 and 2.22.

$$i_a + i_b + i_c = 0 \tag{2.20}$$

$$V_{ab} = R(i_a - i_b) + L\frac{\mathrm{d}i}{\mathrm{d}t}(i_a - i_b) + e_a - e_b \tag{2.21}$$

$$V_{bc} = R(i_a + 2i_b) + L\frac{\mathrm{d}i}{\mathrm{d}t}(i_a + 2i_b) + e_b - e_c \tag{2.22}$$

The state-space model of the BLDC motor is expressed based on the previous equations as a state equation in Equation 2.23 and an output equation in Equation 2.24.

$$\begin{bmatrix} \dot{i}_a \\ \dot{i}_b \\ \dot{\omega}_m \\ \dot{\theta}_m \end{bmatrix} = \begin{bmatrix} -\frac{R}{L} & 0 & 0 & 0 \\ 0 & -\frac{R}{L} & 0 & 0 \\ 0 & 0 & -\frac{k_f}{J} & 0 \\ 0 & 0 & 1 & 0 \end{bmatrix} \begin{bmatrix} i_a \\ i_b \\ \omega_m \\ \theta_m \end{bmatrix} + \begin{bmatrix} \frac{2}{3L} & \frac{1}{3L} & 0 \\ -\frac{1}{3L} & \frac{1}{3L} & 0 \\ 0 & 0 & \frac{1}{J} \\ 0 & 0 & 0 \end{bmatrix} \begin{bmatrix} V_{ab} - e_{ab} \\ V_{bc} - e_{bc} \\ T_e - T_L \end{bmatrix} \tag{2.23}$$

$$\begin{bmatrix} i_a \\ i_b \\ i_c \\ \omega_m \\ \theta_m \end{bmatrix} = \begin{bmatrix} 1 & 0 & 0 & 0 \\ 0 & 1 & 0 & 0 \\ -1 & -1 & 0 & 0 \\ 0 & 0 & 1 & 0 \\ 0 & 0 & 0 & 1 \end{bmatrix} \begin{bmatrix} i_a \\ i_b \\ \omega_m \\ \theta_m \end{bmatrix} \tag{2.24}$$

To increase computational efficiency and simplification, models usually are transferred to the rotating reference frame. However, it is not usable in this situation since the supply voltage is not sinusoidal.

2.2.2. Transmission Systems

Transmission systems have a crucial role in human-robot interfaces. Capstan drives are one of the examples of these systems, which are frequently used in the design of haptic systems. However, generally gear-based transmission systems are used in industrial systems. They reduce the speed of the motor and amplify the torque since commonly electric motors have higher operation speed than the required speeds at the joints. As a result of this smaller motors can be used to drive the same robot link with reduced speeds. Planetary gears, harmonic drives, and cycloidal gears are commonly used gears in light-weight cobots. The main advantage of these gears when they are used in lightweight robots is that they have higher reduction ratio within a smaller enclosure. Thus, smaller

motor with relatively smaller mass can be chosen for the same task. Characteristics and dynamic equations of these common transmission systems are given in the following sections.

2.2.2.1. Planetary Gears

Planetary gears are composed of four main parts which are the sun gear, ring gear, planet gears, and rigid carrier (Figure 2.25). Planet gears are supported by a rigid carrier and the other components, external sun gear and internal ring gear, work mounted to this carrier. In the system, input power is divided into parallel conduction lines, speed is considerably reduced, and torque is boosted. So, higher power to weight ratio is obtained. Hence, they are used in various applications in robotics, automotive and aerospace industries.

Planetary gears can be configured according to the specific cases. Planetary gear operations are tabulated in the Table 2.3.

Table 2.3. Planetary gear configurations (Source: Campbell, 2017)

Sun Gear	**Carrier**	**Ring Gear**	**Speed**	**Torque**	**Direction**
Input	Output	Held	Maximum reduction	Increase	Same as input
Held	Output	Input	Maximum reduction	Increase	Same as input
Output	Input	Held	Maximum increase	Reduction	Same as input
Held	Input	Output	Minimum increase	Reduction	Same as input
Input	Held	Output	Reduction	Increase	Reverse of input
Output	Held	Input	Increase	Reduction	Reverse of input
When any two members are held together, speed and direction are the same as input. Direct 1:1 drive occurs.					
When no member is held or locked together, output can not occur. The result is a neutral condition.					

Dynamic equations of a planetary gear is as follows (Maxon Formulae Handbook, 2018):

$$n_{in} = n_L i_G \tag{2.25}$$

$$M_{in} = \frac{M_L}{i_G \eta} \tag{2.26}$$

$$i_G = \frac{z_1 + z_3}{z_1} \tag{2.27}$$

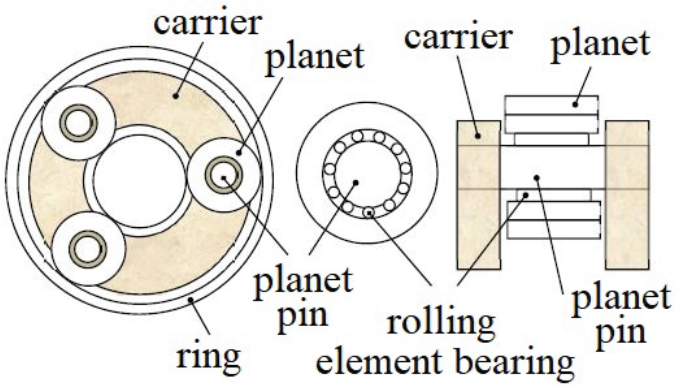

Figure 2.25. Components of the planetary gear set

(Source: Sondkar and Kahraman, 2013)

where n_{in}, n_L and, i_G are input speed, load speed and reduction ratio in the speed of ratio equation. In Equation 2.26, M_{in}, M_L and η are input torque, load torque and efficiency, respectively. In Equation 2.27, z_1 and z_3 are the number of teeth of sun wheel and internal gear, respectively.

2.2.2.2. Harmonic Drive

The Harmonic drive is a type of reducer which offers low backlash and compact design. It consists of three parts shown in Figure 2.26, which are listed below.

- **Circular spline:** It is a steel cylinder with internal teeth.
- **Flex spline:** It is a flexible steel cylinder with external teeth in addition to a flange for best fitting.
- **Wave generator:** It is an elliptical hub composed of ball bearings. This hub is the input of the gear and acts as a torque converter.

It has various advantages over other gear mechanisms. Some of these advantages are:

- Efficient torque transmission,
- Low clearance, almost zero backlash,
- High gear ratio in single step,
- High torsional stiffness in wide range of speeds.

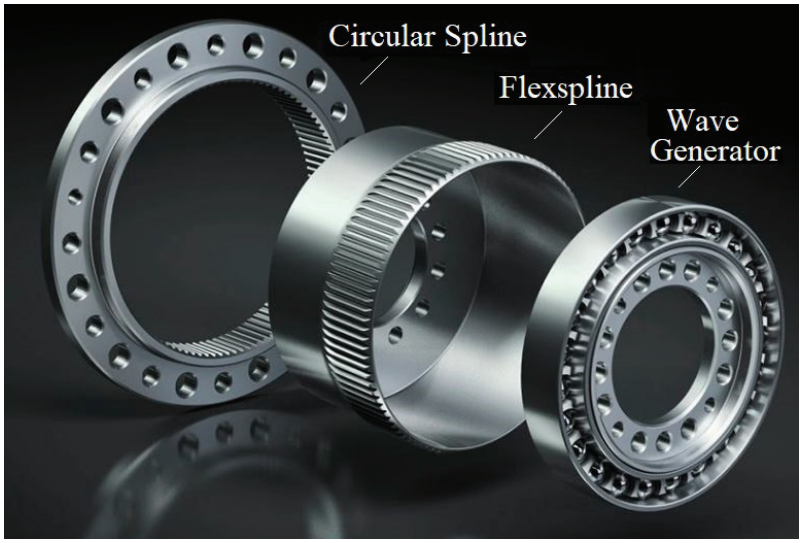

Figure 2.26. Parts of a harmonic drive

(Source: Testa, 2017)

The dynamic model of the harmonic drive is written as

$$i_G = -\frac{360^\circ}{\frac{2}{d}360^\circ} = -\frac{d}{2} \tag{2.28}$$

where d is the total number of teeth of flex spline and i_G is the reduction ratio. The dynamic equations of a case study of motor-gearbox-power consumer system shown in Figure 2.27 are expressed as

$$J_m\ddot{q}_m = T_m - T_l \tag{2.29}$$

$$J_l\ddot{q}_l = i_G T_m - T_l \tag{2.30}$$

$$T_l = K_{el}(q_m - i_G q_l) + D_{el}(\dot{q}_m - i_G\dot{q}_l) \tag{2.31}$$

where K_{el}, D_{el}, T_m and, T_l are torsional stiffness, dumping coefficient, motor torque and power consumer torque, respectively. Also q_m, $\dot{q}_m$ and $\ddot{q}_m$ are position, velocity and the acceleration of the motor while q_l, $\dot{q}_l$ and $\ddot{q}_l$ are position, velocity and the acceleration of the power consumer.

2.2.2.3. Cycloidal Gears

A cycloidal gearbox, shown in Figure 2.28, is composed of four parts which are an input shaft, a single or a compound cycloidal cam, cam followers and an output shaft. The input shaft is connected to the drive unit which causes the rotation of the cycloidal

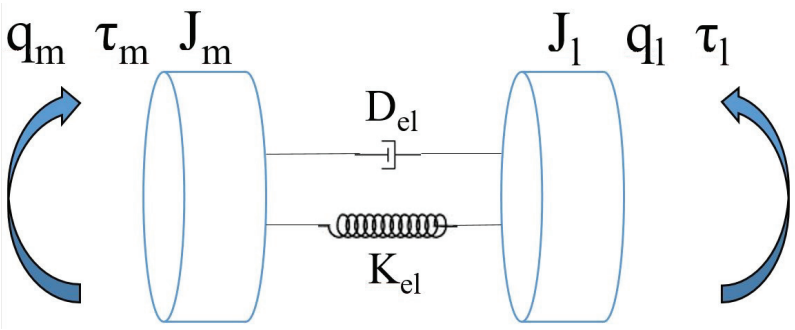

Figure 2.27. Dynamic model of motor-gearbox-power consumer

(Source: Testa, 2017)

cam. Cycloidal cams can either be a single or compound reducers, which may be attached to a second or third cycloidal cam for double and triple reduction, respectively. They can provide reduction ratios from 10:1 up to 300:1. Since they have no stages, they provide better footprint than planetary gears.

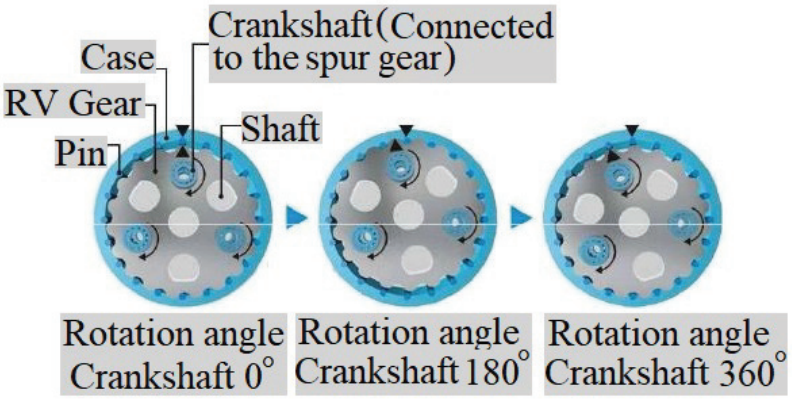

Figure 2.28. A cycloidal gear

(Source: Nabstecco, 2018)

Cycloidal gears have good performance on larger loads. They can be driven with less power since they work at higher gear ratios. It is better to use cycloidal gears in high position accuracy required applications. The dynamic equation of the cycloidal gear is as follows:

$$r = \frac{P - L}{L} \tag{2.32}$$

In Equation 2.32, r, P and L are the reduction ratio, the number of the ring gear pins, and number of lobes on the cycloidal disc, respectively.

As the efficiencies of the transmission systems are compared, planetary gears provides the highest efficiency while harmonic drives offer the lowest efficieny (Sensinger and Lipsey, 2012) and (Onvio, 2018).

2.2.3. Sensors

Sensors are required to provide information on some certain system characteristics of an actuation systems such as position, velocity and torque. These sensors can also provide necessary information to analyze and identify the actuation system. Until this point, Hall sensors were mentioned as they are used to detect the position of the rotor in BLDC motors. The other types of sensors that are used in lightweight collaborative robots for motion-related sensing are encoders, resolvers and DC tachometers. Also, torque sensors have a critical role on the design and application of cobots. Commonly used motion and torque sensors are described in this section.

2.2.3.1. Encoders

Encoders convert the change in angular or linear position information to an electrical signal. An encoder can be rotary or linear, optical or magnetic, and absolute or incremental. A basic single-channel optical encoder is as shown in Figure 2.29. It is composed of a light source, mask, disk, photo sensors, and electronics. Due to the rotation of encoder's shaft, the light passes through the disk and photo sensors perceives the changes as the observed state changes in between light and dark. Electronic part outputs an electrical square-wave signal according to the light and dark states.

Another type of encoders is quadrature encoders. In this approach, two lines are added to the coded disk as channels A and B as shown in Figure 2.30. They track each other with a half cycle offset. If the encoder changes direction channel B reaches the high-state first, and direction of rotation is determined. A third channel named as Z or index can be added to the encoder, and it outputs a pulse per revolution.

According to the principle of operation, the other type of encoder is the magnetic encoder. It uses the magnetic field instead of light sequences to determine the position. Due to the strength of the magnetic field, a magnetic connected to the rotating shaft triggers the plate composed of magnetic sensors. Although the resolution of the magnetic encoders is improved, optical encoders provide higher resolution up to 20 bits. On the

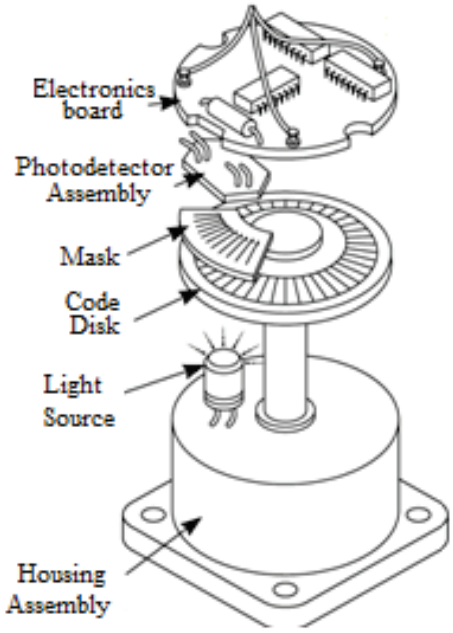

Figure 2.29. Components of Optical Encoder

(Source: Anaheim Automation, 2018)

other hand, optical encoders are vulnerable to external effects such as dirt, liquid or vibrations however, magnetic encoders are resistant to these conditions. Both types of encoders have a gap in between the transmitter and the receiver however, this gap must be kept clean in optical encoders.

2.2.3.2. Resolvers

Resolvers resemble the motors with their rotor-stator structure. There is a reference signal on the rotor. When it rotates, an output signal which is directly proportional to the angle of the rotation of the rotor, is generated. A resolver composes of one input and two output windings (Figure 2.31). As the reference, AC signal is introduced to the input windings R1 and R2, it is induced at the rotor, and it passes through output windings S1-S2 and S3-S4. The magnitude of the sinusoidal output voltage is proportional to the angle of the resolver's rotor. Similar to the quadrature encoder, the direction of rotation is determined with respect to the leading or lagging of sine and cosine signals at the output.

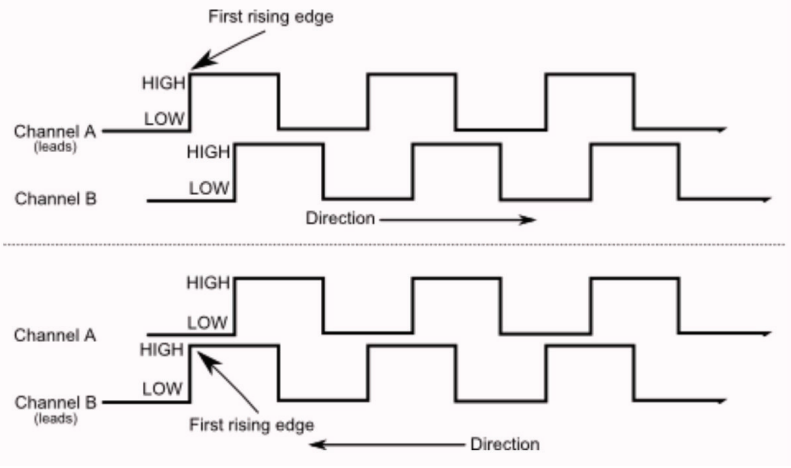

Figure 2.30. Quadrature Encoder

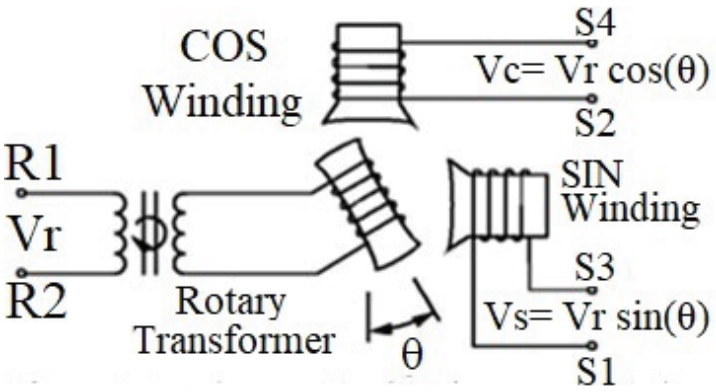

Figure 2.31. A basic resolver

(Source: Lewotsky, 2012)

2.2.3.3. DC Tachometers

DC tachometers are electromagnetic tools that are coupled to the motor shaft, and outputs a voltage signal proportional to the rotation speed. The direction of rotation is determined according to the output signals' polarity. They are composed of tachometer rotor, brushes, and magnets as shown in Figure 2.32 They are the simplest and straight-forward way to measure the speed.

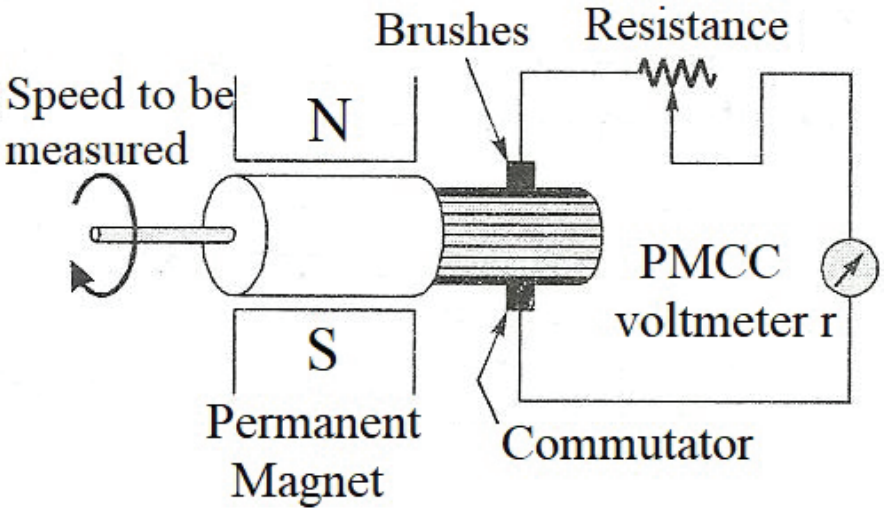

Figure 2.32. Structure of a DC tachometer

(Source: T&M World, 2018)

2.2.3.4. Hall-Effect Sensors

A Hall-effect sensor is a magnetic sensors. As the name implies, it is invented by Edwin Hall in 1879. When a perpendicular magnetic field is applied to a current-carrying conductor, a potential difference is generated on the conductor. Due to the magnetic field, a Lorentz force causes to move electrons to the end of the conductor, and the potential difference occurs across the ends. The generated voltage is called Hall voltage. It is zero, and electrons are uniformly distributed when the magnetic field is not applied shown in Figure 2.33. As the magnetic field is applied, electrons are not uniformly distributed, and cause Hall voltage which is proportional to the cross product of the current and magnetic field. The main advantages of Hall sensors are their low cost and power consumption, long lifetime, and its reliability and sensitivity.

2.2.3.5. Torque Sensors

Torque sensors are an integral part of a collaborative robot, and they are used to sense the physical human-robot interaction. They convert the mechanical torque information to electrical output signals. Torque sensing technology is based on the strain gauges suitably placed to the shaft. As the torque is applied on the shaft, torsion occurs in the

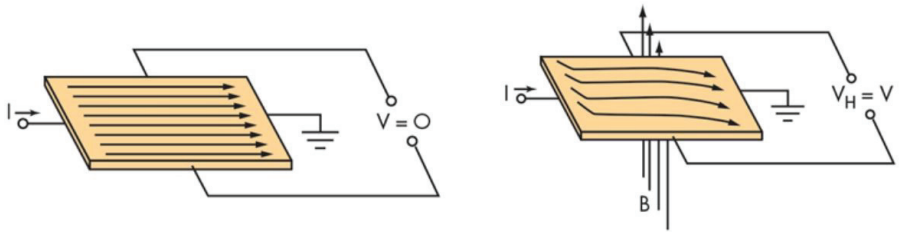

Figure 2.33. Hall voltage according to the magnetic field

(Source: Khader, 2018)

shaft, and shear stresses are induced. To get an electrical output signal, there are four strain gauges which are connected to as a Wheatstone bridge with temperature-resistive elements. Due to the excitation voltage supplied to the bridge and the resistance change of the strain gauge attached to the shaft (due to the induced torque on the shaft), an electrical output proportional to the torque is obtained.

There are two types of torque sensors: reaction and rotary. Reaction torque sensors have a stationary structure with no movable parts. They are fixed to an inertial frame and measure the static torque. In contrast, rotary torque sensors have a rotating shaft coupled with a housing. In general, they are placed between a driving mechanism and a load. The torsional stress created in the shaft produces dynamic torque.

2.2.3.6. Brakes

Safety is an indispensable feature for the interaction between the operator and the robot system in cobots. Apart from the other safety precautions like control algorithms, brakes are optional devices that provide additional safety in cobots. Although there are various brakes used in industrial robots, electromagnetic brakes are among the most popular in cobot applications (Figure 2.34). This brake comprises of a stationary electromagnet. The armature of the brake is pinned to a flat spring of which is pinned to shaft hub. Then, this hub connects to the machine shaft. A magnetic field is created by applying an electrical power to an electromagnetic coil shown in Figure 2.34 (a). So, magnetic force is created and it pulls the armature through an air gap to the face of the magnet. Due to the friction connection between the armature and the magnet, shaft tends to slow and stop. When the electrical power is off, shown in Figure 2.34 (b), the flat spring pulls the armature through the air gap and the armature goes away from the magnet. Then, the

shaft freely rotates due to the air gap between the magnet and the armature.

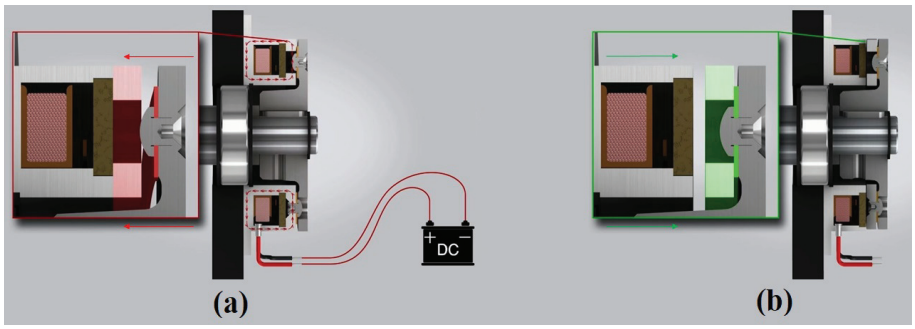

Figure 2.34. Operation of electromagnetic brakes

(Source: KEB, 2018)

2.3. Conclusion

In this section, various actuation systems used in light-weight collaborative robots are investigated. All configurations have certain advantages and disadvantages with respect to their counterparts. However, the joint torque control method is more suitable due to its modular structure, safety and performance metrics. Therefore, joint torque control actuation systems and their components are investigated in detail. As a result, an actuation system that resembles the UR5 robot's actuation system is selected to be studied in this thesis work. This actuation system has features as small in size, light-weight, flexible, high payload capacity and safety. The whole system is composed of a BLDC motor, a planetary gearhead, an encoder, and a torque sensor.

CHAPTER 3

METHODOLOGY

This section is composed of two parts which are simulation test setup and experimental test setup. In the experimental test setup, the procedure followed to configure the actuation system is presented and explained in detail. For the simulation test setup, different simulation models (DC equivalent, Simscape and comprehensive models) are developed in MATLAB Simulink environment.

3.1. Experimental Test Setup

As it is previously mentioned in the literature survey, an actuation system is configure to be composed of a brushless DC motor, a planetary gearhead, an encoder, and a rotary torque sensor. There are also a magneto-rheological (MR) brake and a belt-pulley system as complementary parts to perform load tests. System is monitored and controlled via a data acquisition card and an external servo driver. The experimental test setup and its flowchart are as shown in Figure 3.1 and Figure 3.2, respectively.

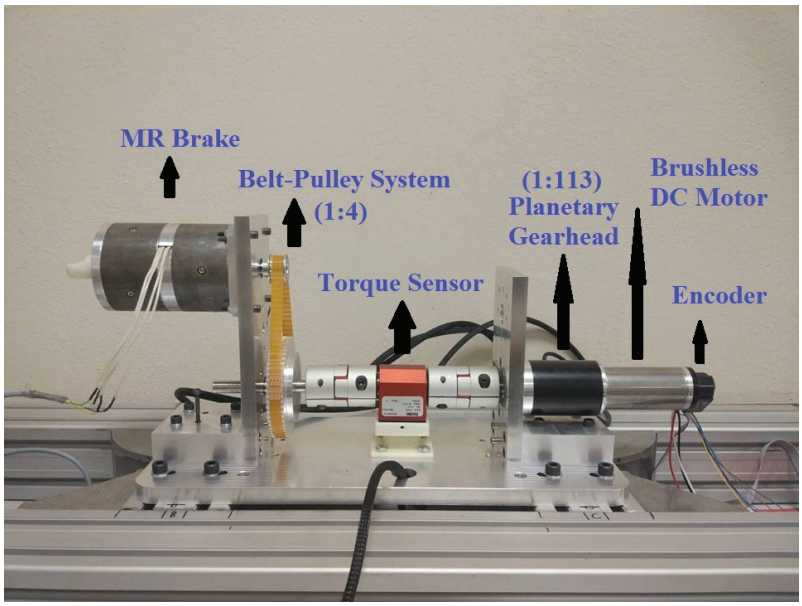

Figure 3.1. The experimental test setup

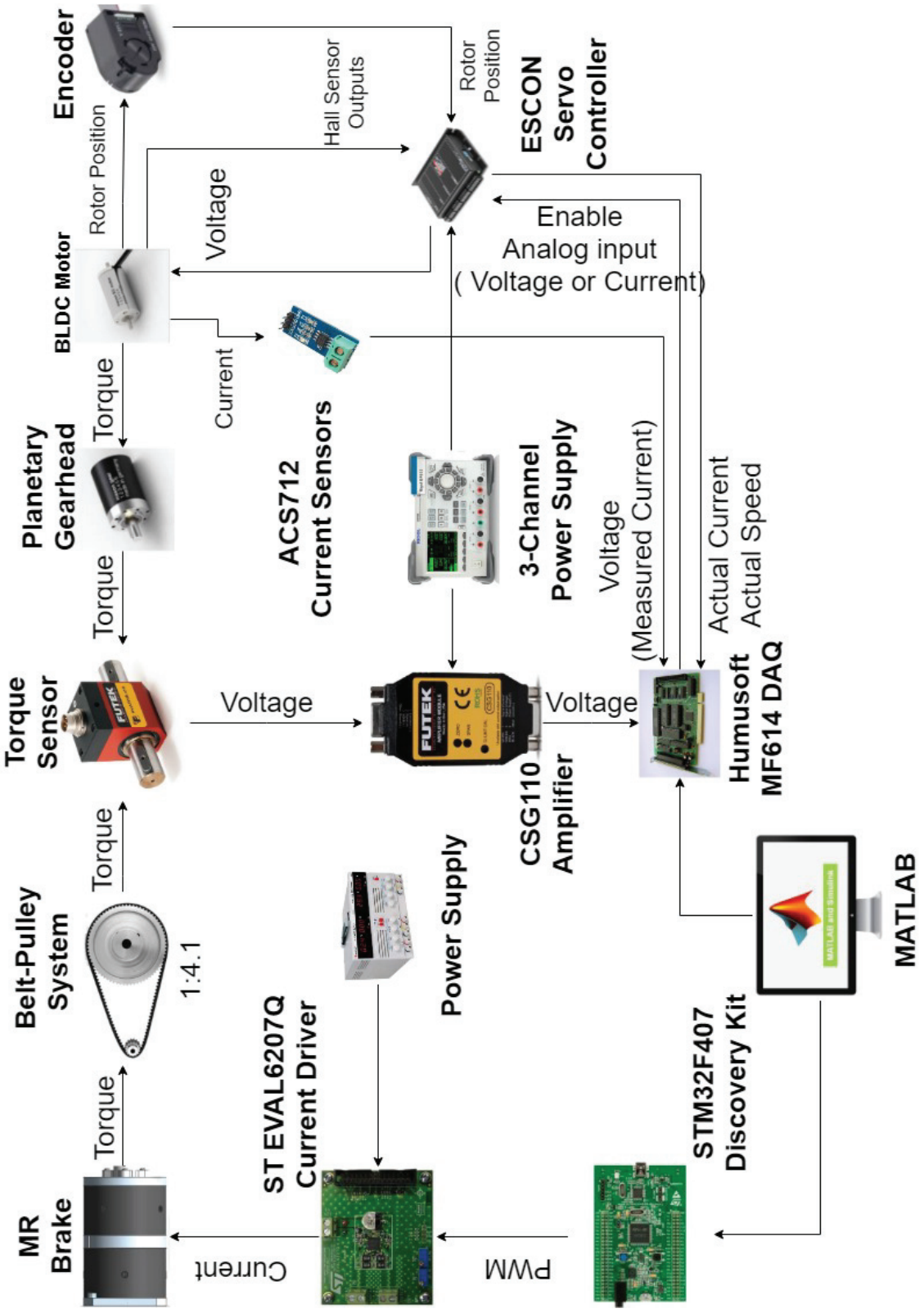

Figure 3.2. The flowchart of the system

The main aim in constructing this experimental test setup is to run tests to collects data which are to be used in building and validating a comprehensive model of the actuation system of a cobot. BLDC motor used as the actuator is a Maxon EC 40, 40 mm diameter, 170 Watt motor with the part number 393023. The motor is integrated with three Hall sensors, and its specifications are given in Table 3.1. The specification sheet provided by Maxon company is presented in Appendix A.

Table 3.1. Maxon EC 40, 170 Watt Brushless DC motor specifications (Source: Maxon Motor Catalog, 2018)

	Maxon Motor Data	**Value**	**Unit**
	Values at nominal voltage		
1	Nominal Voltage	24	V
2	No load speed	9840	rpm
3	No load current	386	mA
4	Nominal speed	9120	rpm
5	Nominal torque	165	mNm
6	Nominal current	7.39	A
7	Stall torque	2660	mNm
8	Stall current	115	A
9	Maximum efficiency	89	%
	Characteristics		
10	Terminal resistance phase to phase	0.209	Ω
11	Terminal inductance phase to phase	0.0843	mH
12	Torque constant	23.2	mNm/A
13	Speed constant	412	rpm/V
14	Speed/torque gradient	3.71	rpm/mNm
15	Mechanical time constant	2.09	ms
16	Rotor inertia	53.8	gcm^2
29	Number of pole pairs	1	-
30	Number of phases	3	-
31	Weight of motor	580	g

Maxon GP 52 C coded 52 mm diameter planetary gearhead with part number 223095 is used as the transmission system. It has a high gear ratio of 113:1, and its specifications are given in Table 3.2 below. The specification sheet provided by the manufacturer is given in Appendix A.

Maxon HEDL 5540 encoder, used as the motor position sensor, has three channels and it is capable of sensing 500 counts per turn (or pulses per revolution). Its part number is 110516. It is a digital incremental encoder which operates up to 100 KHz and 12000

Table 3.2. Maxon Planetary gearhead GP 52 C, 4–30 Nm specifications (Source: Maxon Motor Catalog, 2018)

	Maxon Gear Data	**Value**	**Unit**
	Gearhead Data		
1	Reduction	113:1	-
2	Absolute reduction	338/3	-
3	Maximum motor shaft diameter	8	mm
4	Number of stages	3	-
5	Max. continuous torque	30	Nm
6	Max. intermittent torque at gear output	45	Nm
7	Max. efficiency	75	%
8	Weight	770	g
9	Average backlash no load	1.0	°
10	Mass inertia	9.3	gcm^2
11	Gearhead length L1	0.209	mm

rpm. The specification sheet of the encoder is presented in Appendix A.

Maxon ESCON 50/5 servo controller shown in Figure 3.3 with part number 409510 is used to drive the motor and it is capable of providing output of the monitored signals such as speed and current. Also, motor parameters are set by ESCON Studio software which works with this servo controller. The specifications of the servo controller (servo drive) are given in Table 3.3.

Figure 3.3. ESCON 50/5 Servo Controller
(Source: Maxon Motor Catalog, 2018)

Humusoft MF614 multifunction I/O card shown in Figure 3.4 is used in the system as a data acquisition card (DAQ). It is connected to the computer as a PCI card, and it

Table 3.3. ESCON 50/5 Servo Controller specifications (Source: Maxon Motor Catalog, 2018)

Electrical Rating	Nominal Operating Voltage	10...50 VDC
	Output Current I_{cont} / I_{max} (<20 s)	5A / 15A
	Maximum efficiency	95 %
	Max. speed DC motor	Limited by max. permissible speed (motor) and max. output voltage (controller)
	Max. speed EC motor	150000 rpm (1 pole pair)
	Analog Input 1 Analog Input 2	Resolution 12-bit ; -10V...+10V; differential
Inputs Outputs	Analog Input 1 Analog Input 2	Resolution 12-bit ; -4V...+4V; referenced to GND
	Digital Input 1 Digital Input 2	+2.4...+36 VDC
	Digital Input/Output 3 Digital Input/Output 4	+2.4...+36 VDC
	Hall sensor signals	H1, H2, H3
	Encoder signals	A, A\, B, B\(max. 1 MHz)
Voltage Outputs	Auxiliary output voltage	+5 VDC ($(I_L \leq 10$ mA)
	Hall sensor supply voltage	+5 VDC ($(I_L \leq 30$ mA)
	Encoder supply voltage	+5 VDC ($(I_L \leq 70$ mA)
Potentiometers	Potentiometer P1 Potentiometer P2	240°; linear
Motor Connections	DC Motor	+ Motor, - Motor
	EC Motor	Motor winding 1, 2, and 3
Interface	USB 2.0 / USB 3.0	full speed

is compatible with Real Time Toolbox in MATLAB. The specifications of DAQ are as follows (Humusoft, 2018):

- 100 kHz throughput 12 bit A/D converters with four selectable input ranges ($\pm$10V, $\pm$5V, 0-10V, 0-5V), 8 channel input multiplexer, and sample/hold circuit
- 12 bit D/A converters with $\pm$10V output range
- 8 bit digital input and output ports
- 4 quadrature encoder inputs and 5 timers/counters.

Futek TRS300 is used as the torque sensor in the system. It is shaft to shaft rotary torque sensor which measures the torque values up to 10 Nm and has 955 Nm/rad

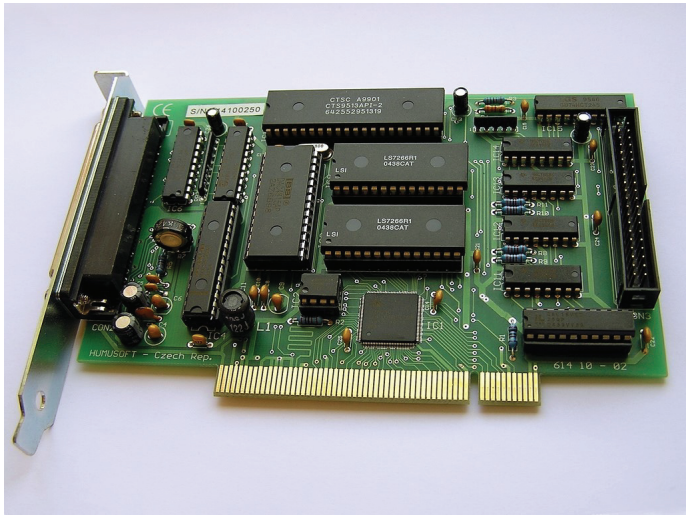

Figure 3.4. Humusoft MF 614 I/O Card

(Source: Humusoft, 2018)

torsional stiffness value. It makes use of strain gauge technology and operates up to 3000 rpm by slip-ring signal transmission. The specifications of the torque sensor are as shown in Figure 3.5.

Futek CSG110 Amplifier is not only a general purpose amplifier but also a calibration tool for the rotary torque sensor. It provides multiple outputs to the user to adjust the output according to the application. The output options are ± 5 VDC, ± 10 VDC, $0-20$ mA, $4-20$ mA, $0-16$ mA, $5-25$ mA. In the test setup, ± 5 VDC output option is selected. CSG110 amplifier steps up the 2 mV/V signal to ± 5V analog signal. It also has a low-pass filter. The torque sensor is calibrated according to the Wheatstone bridge and interchangeable resistors as described in Futek (2018). The specifications of CSG110 amplifier are shown in Figure 3.6.

Two-directional MR Brake designed in the IZTECH Robotics Lab is used with the belt-pulley system to simulate the load in the experimental test setup. Its rated torque is about 3.84 Nm with 62 rad/s bandwidth, and it weighs 3.570 kg (Karabulut, 2017). The belt-pulley system has a ratio of 4.1.

STM32F4DISCOVERY kit and ST L6207Q Evaluation board are used for driving the MR Brake with current input. The real-time experiments are performed by STM support package in Matlab.

ACS712 current sensor modules are used for validating the phase currents of the BLDC motor. It is a Hall-Effect based linear current sensor which can measure both AC and DC current. It is composed of a Hall sensor circuit with a copper conduction

SPECIFICATIONS	
PERFORMANCE	
Nonlinearity	±0.2% of RO
Hysteresis	±0.1% of RO
Nonrepeatability	±0.2% of RO
Rotational Speed	3000 Max
ELECTRICAL	
Rated Output (RO)	2 mV/V nom
Excitation (VDC or VAC)	5 to 11
Bridge Resistance	350 Ohm nom
Connection	6 pin Binder Series #581 (09-0323-99-06)
MECHANICAL	
Safe Overload	150% of RO
Material	Aluminum 6061 (Housing) Steel Alloy (Shaft)
IP Rating	IP40
TEMPERATURE	
Operating Temperature	14 to 194°F (–10 to 90°C)
Compensated Temperature	41 to 122°F (5 to 50°C)
Temperature Shift Zero	±0.01% of RO/°F (±0.02% of RO/°C)
Temperature Shift Span	±0.01% of RO/°F (±0.02% of RO/°C)
CALIBRATION	
Calibration Test Excitation	10 VDC
Calibration (standard)	Certificate of Conformance
Calibration (available)	5-pt CW & CCW
Shunt Calibration Value	With sensor fully connected jump pins 1 & 6 to generate 2 mV/V nom output

Figure 3.5. Futek TRS300 shaft to shaft rotary torque sensor specifications (Source: Futek, 2018)

path where the magnetic field is generated by flowing applied current. Integrated Hall IC senses the current and converts into a proportional voltage. It offers 5 A, 20 A, and 30 A current measurement according to the chip inside. 5 A modules are used for per phase which is connected in series to the phase windings. The specifications of the current sensor modules are given in Table 3.4.

The current sensor module and its wiring diagram is shown in Figure 3.7 (a) and (b).

In the experimental test setup shown in Figure 3.1, aluminum sigma profiles are used for a rigid structure when connecting the components of the setup. There is an aluminum base plate is manufactured and fixed to the sigma profiles by screws. This

Electrical Specifications				
Parameter	Min	Typical	Max	Unit
Power Supply[6]	14		26	VDC
Current Draw[7]		30		mA
Output Impedance (Voltage)		< 1 Ohms		Ohms
Output Impedance (Current)			700	Ohms
Sensor Impedance	100			Ohms
Bandwidth	1000		25000	Hz
Common Mode Rejection Ration	120			dB
Noise		15		mVp-p
Output Span Range	-10		10	% of Rated Output
Output Zero Range	-10		10	% of Rated Output
Gain Drift with Temperature	-25	X	25	PPM of FSR per degree Celsius
Gain Non-Linearity	-0.001	X	0.001	% of FSR
Zero Drift with Temperature	-25	X	25	PPM of FSR per degree Celsius

Figure 3.6. Futek CSG110 strain gauge universal amplifier specifications (Source: Futek, 2018)

Table 3.4. Current sensor module specifications (Source: Allegromicro, 2018)

	5A Module
Supply Voltage (VCC)	5 VDC Nominal
Measurement Range	-5 to +5 Amps
Voltage at 0A	VCC/2 (nominally 2.5 VDC)
Scale Factor	185 mV per Amp
Chip	ACS712ELC-05B

base plate not only provides additional rigidity but also prevents the misalignment of the screwed blocks on it. Three guide pins between the base plate and L-shaped blocks are used. Also, two guide pins are used inside of each L-shaped blocks to prevent possible misalignments since misalignment of the shafts is an important problem. A possible misalignment can cause undesirable effects on the measurements such as sinusoidal fluctuations measured torque signal. In addition to these, two deep groove ball bearings are placed at output shafts of the MR brake and the gearhead. A double row design angular contact ball bearing is used as bedding of the large diameter pulley's shaft since the stress over the long L-shaped block is greater than the other L-shaped block because of 3.570 kg MR brake. The rotary torque sensor shafts are connected with the elastic couplings to the pulley shaft and gear shaft. Also, a 3D-printed material is used to house the torque sensor, which is fixed to the base plate.

Experimental tests are designed to be performed with and without load both in

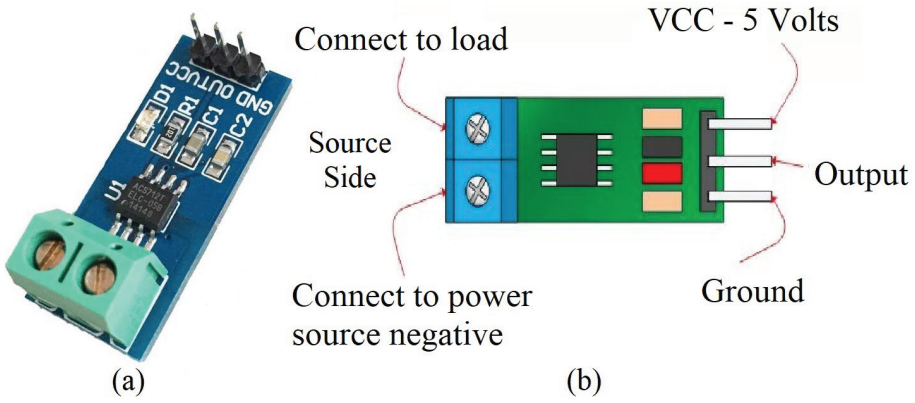

Figure 3.7. (a) The current sensor module, (b) Wiring diagram of the module (Source: Allegromicro, 2018)

voltage or current modes in which voltage or current is given to the system as input signals, respectively. In return, various information such as actual current, position and speed are acquired from the setup. The flow of information is presented in Figure 3.2 and explained in detail in the following paragraphs.

The system is driven by the ESCON controller which offers voltage and current modes. The demands for voltages or currents to be applied are sent to the ESCON controller from the host PC running Matlab via the Humusoft DAQ. During the no-load tests, current sensors, ESCON controller and Humusoft DAQ are used only. In both operation modes (voltage and current), a digital enable signal, and analog set voltage corresponding to the demanded voltage or current output from the ESCON controller is sent from the Humusoft DAQ to the ESCON controller. ESCON studio software receives back motor's measured speed and current, encoder counts, and operating temperature. It allows to record the temperature of the motor windings and determine the actual terminal resistances according to Equation 3.1. These data are presented in the graphical user interface of the ESCON studio software and they can be recorded.

$$R_{TW} = R_{mot}[1 + \alpha_{Cu}(T_W - 25°C)] \tag{3.1}$$

where T_W, R_{TW}, R_{mot}, and α_{Cu} are winding temperature, winding resistance at the actual temperature, terminal resistance of the motor and resistance coefficient of copper.

As a first step of the experimental test setup configuration, motor parameters are recorded in the ESCON controller by using ESCON Studio Startup wizard. Since the maximum continuous speed of the gear is 6000 rpm, the maximum permissible speed is

set to this value. The digital incremental encoder resolution is defined as 500 counts per turn. Speed control mode with static IxR compensation is chosen however, the compensation coefficient is set to be zero to prevent effects of control in the model. There are two analog outputs in both operation modes. One of them is the measured speed value which is mapped to ± 4 V for ± 6000 rpm in both no-load and load tests. The other one is the measured current value which is mapped to ± 4 V for ± 0.6 A and ± 4 A in no-load and load tests, respectively. The rotor position is obtained by the encoder attached at the rear end of the motor's rotor. According to this measurement, speed of the motor is calculated by the ESCON controller. Motor speed and current measurements are processed and sent from the ESCON controller to the Humusoft DAQ via analog channels. Additionally, phase currents on the motor windings are measured by identical current sensors connected to the motor windings in series. The measured phase current are sent to the Humusoft DAQ via analog channels as well. The calibration of these phase current sensors are explained in the next sections.

To observe the system with varying loads, an MR Brake is added to the system which provides up to 3.84 Nm as a load. However, it displays a linear torque output up to 2.5 Nm. A belt-pulley system with a ratio of 4.1:1 is attached to the brake's shaft to amplify the resistance torque value up to 10 Nm since the torque sensor measures the torque difference between the input and output shaft up to 10 Nm. ST L6207Q Evaluation board is used as the current driver to vary the resistance torque of the MR Brake. This current driver is controlled by the PWM inputs generated from STM32F407 Discovery kit, which receives the demands from the host PC. While the resistance torque is subjected to the system, the torque sensor is used to measure the torque value between large pulley's output shaft and the planetary gear's output shaft. The output voltage of the torque sensor is amplified by CSG110 Amplifier to ± 5 VDC. A three-channel power supply is used to supply enegry to the ESCON controller and in load tests it supplies energy also to the CSG110 Amplifier. The output of the amplifier is acquired from an analog input channel of the Humusoft DAQ. The detailed explanation of the torque sensor's calibration is given in the next sections.

3.1.1. Calibration of the Current Sensor

The connection details of the current sensor is given in Figure 3.7. First of all, the load side of the sensor is connected between the BLDC motor phase windings and the ESCON controller while the output side of the sensor is connected to an analog input

channel of the Humusoft DAQ. Three 5 A current sensors are connected to the BLDC motor phase windings in series.

The supply voltage of the sensor is 5 VDC, and when there is no current driven through the sensor, it gives 2.5 VDC output. The sensor output is checked if it outputs 2.5 VDC when no current is supplied to the motor and the deviation from this values is used for the calibration. In addition, the output of the current sensor depends on the polarity at the load end of the device. If it is connected as illustrated in Figure 3.7 (b), the output will rise from 2.5 VDC as the current is increased. In contrast, if it is connected in the opposite way, the output will decrease from the 2.5 VDC. Since the sensor has a scale factor with a 185 mV per Amp, the output is divided by 0.185 to calculate the actual current supplied to the motor windings.

The current values are also measured and then processed by an algorithm implemented in the ESCON Controller. It enables to validate the actual currents by comparing two measurement techniques.

3.1.2. Calibration of the Torque Sensor

Calibration of the torque sensor is done by calibrating the CSG110 amplifier which is shown in Figure 3.8. Calibration is performed without applying a load and shunt resistor acts as the load in the calibration process. All of the connections of the amplifier and its switch configurations must be done according to the user manual (REF), and the amplifier must be connected to the data acquisition card for reading voltage or current values. The steps of shunt calibration are as follows making use of the components denoted in Figure 3.8:

1. Determine the value of the shunt resistor.
2. Connect the shunt resistor in the spot labeled ‘RSH’.
3. Press the shunt button.
4. Adjust the span with a screwdriver to the expected output, while the shunt button is enabled.
5. Set the shunt button to off-state and set the voltage to zero.

In the beginning, it is required to measure the bridge and shunt resistor values. The bridge resistor is the resistance of the Wheatstone bridge within the torque sensor.

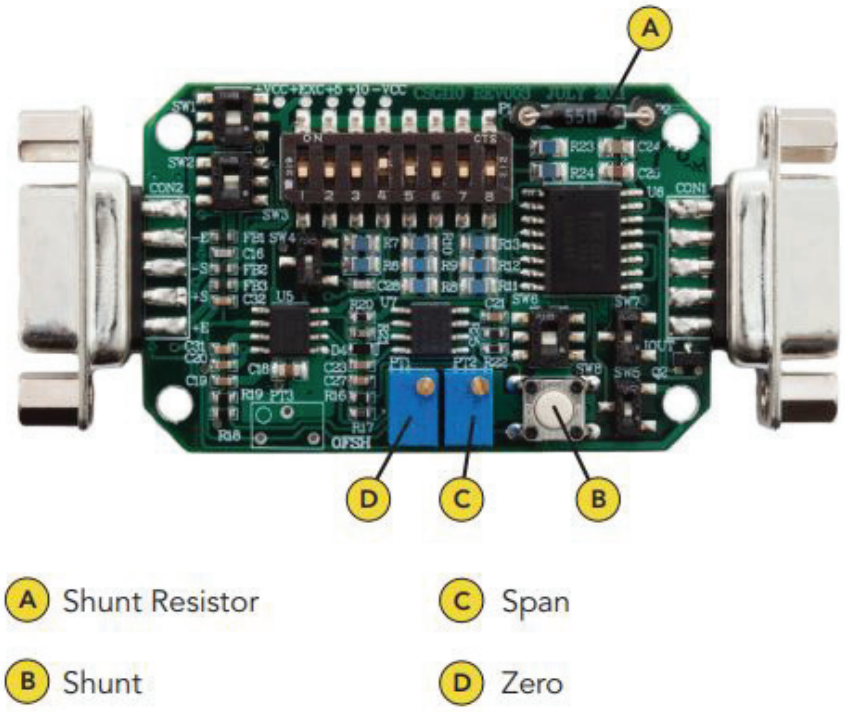

Figure 3.8. Shunt calibration pins of CSG110 Amplifier

(Source: Futek, 2018)

It is determined as 350 Ω by measuring the resistance across the 'Signal' + and 'Signal –' wires of the torque sensor. The shunt resistor is measured as 60.4 kΩ. According to the Shunt Calibration Calculator provided by Futek, the output voltage is calculated as 1.44449 mV/V where the sensor's actual output voltage is 1.9982 mV/V. So, the simulated load would be approximately 72% of the rated output. Therefore, the span is adjusted to 3.6 VDC to correlate with the simulated load since the excitation voltage is 5.0 VDC. Then, the shunt button is set to off-state, the voltage is set to zero, and the process is monitored by the data acquisition card's analog channel. In this condition, 10 Nm load is mapped to 5 VDC.

The calibration process is also performed with predefined loads placed at the shaft of the pulley coupled with torque sensor's shaft while BLDC motor's rotor motion is constrained as shown in Figure 3.9. The sensor measures the torque difference between the input and output shafts. An aluminum rod is used as the moment arm. Then, various calibrated weights are attached to the end of the moment arm and thus, moments are applied to the system shown in Figure 3.10.

A water gage is placed on the aluminum rod to ensure that the moment arm is par-

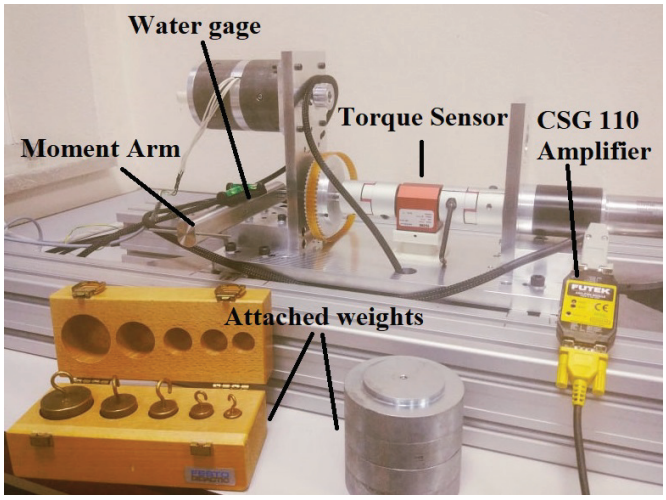

Figure 3.9. Calibration of the torque sensor with predefined loads

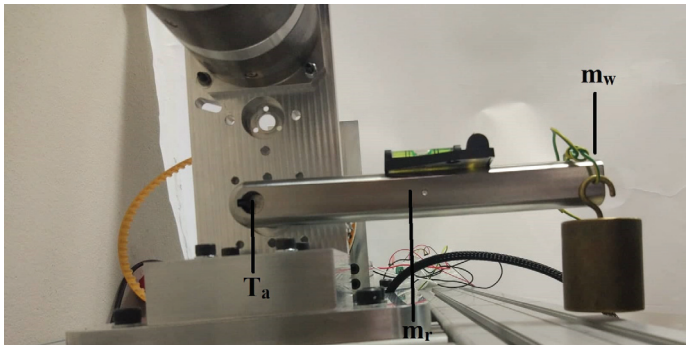

Figure 3.10. Verification of the calibration of the torque sensor with predefined loads

allel to the base frame. The applied torques are calculated by Equation 3.2 and the measurements via the torque sensor are monitored through Humusoft DAQ's analog channel.

$$T_a = m_r d + m_w l \tag{3.2}$$

In Equation 3.2, T_a is the applied torque, m_r is the weight of the moment arm, m_w is the total weight of the attached calibrated weights at the end of the moment arm, d is the distance between the center of the shaft and the center of gravity of the moment arm, and l is the distance between the center of the shaft and attached calibrated weights. As a result of the calibration process, the relationship between applied torque and measured voltage is given in Figure 3.11. Then, a curve is fit to determine formula representing the relationship between applied torque and the measured voltage. The relation is formulated as shown in Equation 3.3.

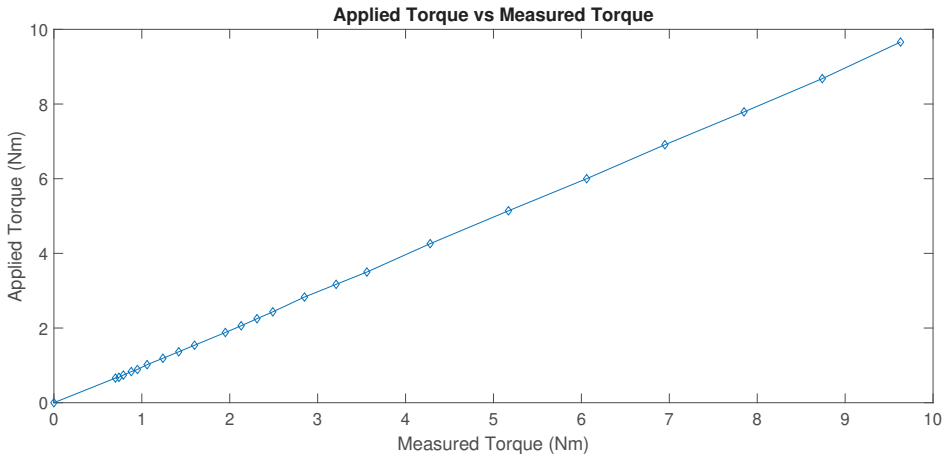

Figure 3.11. Applied torque versus measured torque

$$y = 0.9971x + 0.05587 \tag{3.3}$$

In Equation 3.3, y and x are the applied torque and the measured torque, respectively. Root mean square error (RMSE) between the measured and applied values of torque is calculated as 0.02328 Nm. If the applied torque is assumed to be equal to the measured torque, the root mean square error is calculated as 0.0504 Nm.

3.2. Simulation Test Setup

In this section, three different simulation techniques of the system are demonstrated for no-load and load cases. Simulations are performed in the MATLAB Simulink environment. Due to the compatibility reasons, the experimental tests are conducted in MATLAB version 2014a. The actual inputs and outputs are stored in version 2014a and evaluated in version 2018a.

All of three different models investigate the relation between the voltage input and speed output of the system. In addition to these models, the current-speed frequency response tests are performed in the no-load condition. The modeling techniques are as follows:

- DC equivalent model
- Simscape model
- Comprehensive model

3.2.1. DC Equivalent Model

In the DC equivalent model, the three-phase structure of the brushless DC motor is reduced to a single-phase structure. Therefore, the DC motor equations 2.1 through 2.8 in the Literature Survey is valid in this case.

3.2.2. Simscape Model

Simscape is a library in Simulink environment, and this library enables to build the model of physical components. In order to model the experimental test setup, Simscape library is used in this model. 'Permanent Magnet Synchronous Machine (PMSM)' and 'Universal Bridge' blocks are used to build the BLDC motor and the motor's commutation while 'Planetary Gear' block is used to build the planetary gear in the experimental test setup.

PMSM block models the dynamics of the three-phase permanent magnet synchronous machine either in motor or generator mode. The operation mode depends on the mechanical torque which is positive for motor mode and negative for generator mode. The block represents the electrical and mechanical parts of the machine for a second-order state-space model. Also, it has sinusoidal and trapezoidal models according to the back EMF waveforms. Since the BLDC motor in the test setup is a trapezoidal type three-phase motor, the block generates three trapezoidal back EMF waveforms. In three-phase configuration, the stator windings are assumed to be connected in wye (Y) to an internal neutral point. In the parameters tab of the block, motor parameters such as stator phase resistance and inductance, inertia, viscous friction coefficient, pole pairs and static friction are given to the block individually. Except viscous damping and static friction, other parameters are given according to the specification sheet of the BLDC motor. Static friction and viscous friction coefficient are obtained experimentally. Additionally, the machine constant can be specified as either flux linkage, torque constant or voltage constant. The machine constant can be specified either torque constant or voltage constant since these constants are given in motor's specification sheet. There is also another tab in the block which enables to compute parameters from standard manufacturer specifications. Motor's specifications mentioned in parameters tab are used in the block, and it computes and applies the block parameters. The block outputs stator currents, stator back EMFs, rotor speed, electromagnetic torque and Hall effect signals. In the model, Hall effect signals

are decoded and phase current signs are determined according to the Table 2.2. Then, the switch (gate) configuration is obtained according to the sign of the phase currents given in Table 2.2. The switch configuration is fed to the Universal Bridge block which implements a universal three-phase power converter, which can composed of up to 6 power switches. As it is stated in the BLDC drive scheme in Figure 2.24, the type of power electronic components is chosen as MOSFET/Diodes. According to the supplied voltage input signal and switching sequence (gate) input, two on-state phases are determined by the block and sent to the PMSM block. Planetary Gear block consists of sun-planet and ring-planet subcomponent blocks, and provides speed reduction. According to the Table 2.3, the speed input is connected to sun gear, ring gear is locked, and output is obtained by carrier. Thus, reduction in speed and increase in torque are provided. The direction of the output is same as the input direction.

3.2.3. Comprehensive Model

In the comprehensive model of the system, the three-phase structure of the brushless DC motor and the planetary gearhead are modeled in detail. The model is composed of the current generation, emf generation, mechanical, commutation and inverter subsystems. In current generation subsystem, the phase currents are obtained by the Equations 2.9 through 2.11. In mechanical subsystem, the speed of the motor is determined by the Equations 2.12 and 2.16. Then, back-emf is generated according to the Equations 2.13 through 2.15. In commutation and inverter subsystem phase voltages are determined according to the Equations 2.20 through 2.22 and the rotor position angle.

3.2.4. Transfer Function Model - Frequency Response

In transfer function model, the relationship between the input current and the speed output is investigated. For this purpose, DC equivalent model's current-speed equations 2.2 and 2.4 are used. The transfer function is calculated in frequency domain, and it is compared with the measured values.

The same inputs are given to all models, and the system responses are observed. The experimental tests are performed in current mode for the frequency response test. For the other models, experimental tests are performed in voltage mode.

CHAPTER 4

RESULTS

In the previous chapter, a total of four simulation models are introduced for the selected actuation system. According to these models, some specific tests are performed in order to validate the actuation system models. A voltage input signal is composed to rise to a specific constant voltage with a ramp profile, which is given to the experimental test setup in both load and no-load conditions. Additionally, frequency response test is conducted in no load condition. Hence, the driven current of the system is obtained by ESCON controller and current sensors placed on the motor windings. Also, the speed at the gear shaft is obtained by ESCON controller. The given inputs and experimental results are stored. Then, same inputs are given to simulation models, and experimental results are compared with the simulation results. The results are presented in the following sections.

4.1. DC Equivalent Model Test Results

Simulations are carried out in Matlab 9.1 (R2018A) and Simulink using the fixed step solver $ode4(Runge - Kutta)$. The simulation step size is 0.001 s. In order to validate the system with DC equivalent model, voltage input signal is composed to rise to a specific constant voltage with a ramp profile is given to the system at load and no-load experiments. The no-load current output comparison between the test measurements and the model is shown in Figure 4.1.

In transient response part, there is a gain difference between the ESCON measurement and the simulation results. It is caused by the dynamical changes in viscous friction coefficient which is not account for in the simulation test. At steady-state, a more reliably calculated viscous coefficient is used. As a result of this, the root mean square error (RMSE) between ESCON's current measurements and the simulation results at steady state reduces to $7.3559\ 10^{-4}$ A while this value is 0.0162 A in transient state. At steady state, also the no-load current of the BLDC motor is given in its specification sheet to have a tolerance with $\pm 50\%$. Therefore, it can be concluded the current differences are at reasonable ranges.

No-load speed output comparison between experimental tests and the simulation

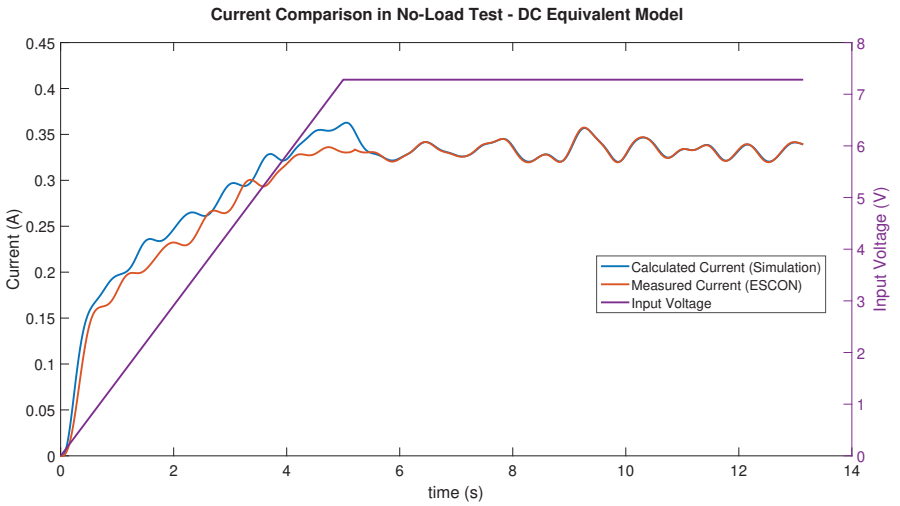

Figure 4.1. DC equivalent model current results at no-load test

test is shown in Figure 4.2. Both speed outputs and voltage input supplied to both simulation and experimental tests are demonstrated in the same graph. Although, the no-load speed of the BLDC motor is given as a tolerance with $\pm 10\%$, the RMSE between ESCON's speed measurements and the simulation results are 0.013 rad/s and 0.0038 rad/s at transient and steady state, respectively.

At no-load tests, combined (transient and steady state) root mean square errors are also calculated. These values are 0.0105 A and 0.0088 rad/s for the current and speed values, respectively.

The load tests are performed by using MR Brake to apply resistive load to the motion of the motor's rotor. Additionally, the coupling is held for short periods of time by a human in order to simulate an unintentional load disturbance due to human robot interaction. The current and speed changes due to the applied resistive torque are investigated. The current changes are as shown in Figure 4.3. The input to the system is the same voltage input profile explained in the previous tests. Applied resistive torque which is measured from the torque sensor is demonstrated at the right y-axis in 4.3 since the changes in current and speed are directly related with the applied torque. A resistive torque is applied to the system between the 9^{th} and 15^{th} seconds by MR brake, and resistive torque by the human brake is applied through for 4 times. The RMSE between ESCON's current measurements and the simulation results is 0.2737 A. The difference is caused by ESCON which gives average values of the current signal.

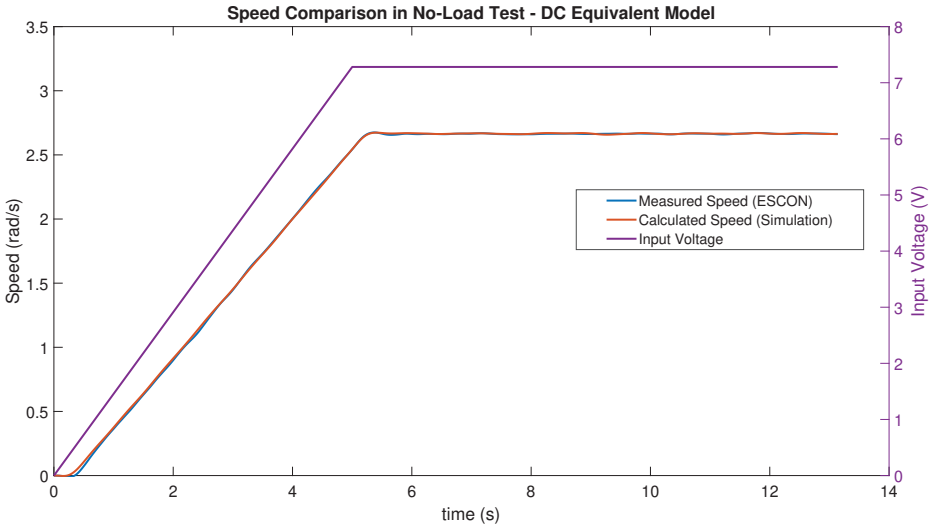

Figure 4.2. DC equivalent model speed results at no-load test

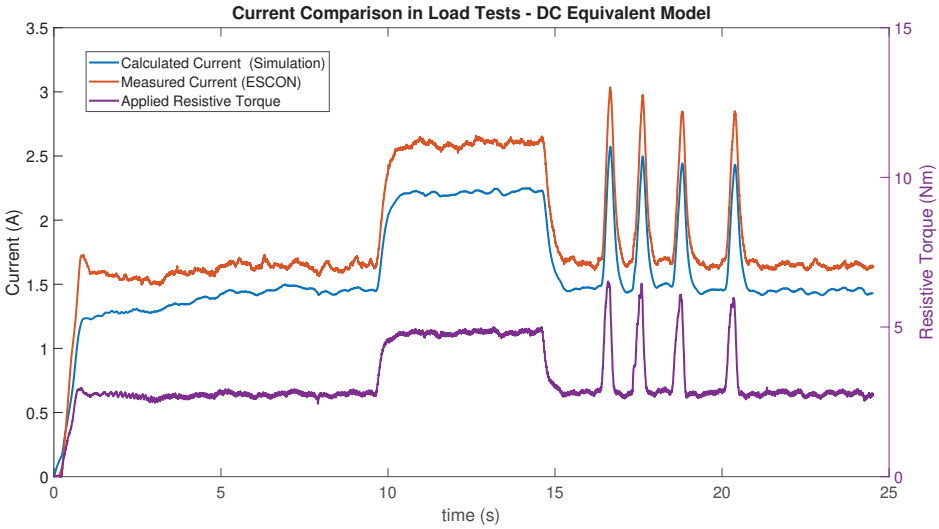

Figure 4.3. DC equivalent model current results at load test

Speed output comparison between the experimental tests and simulation tests under load condition is shown in Figure 4.4. In addition to the intentionally applied torque, the motor-gear system has a constant load caused by the MR brake's static friction and flexibility of the belt-pulley system. Although the summation of these effects are implemented as load torque in the simulation, there is a delay caused by the dynamics of the system that results latency in the transient response. However, due to the variation of the applied torque, decrease in speeds are similar to each other. The RMSE between the ESCON's speed measurements and simulation results are 0.0249 rad/s.

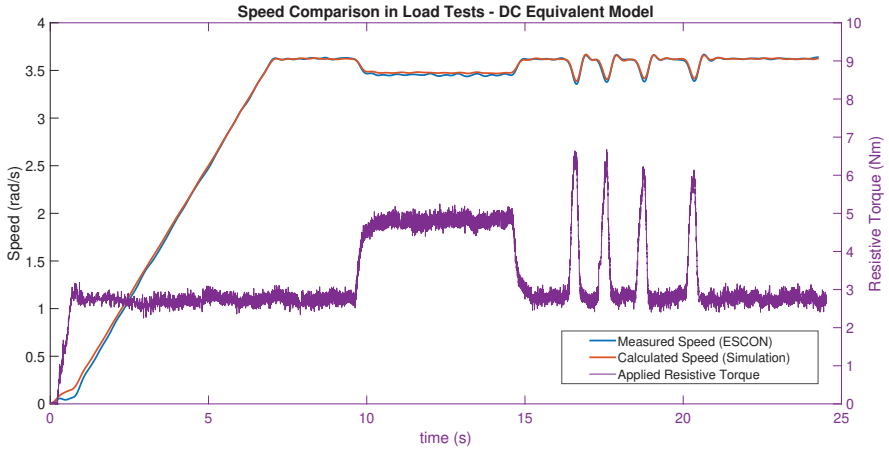

Figure 4.4. DC equivalent model speed results at load test

4.2. Simscape Model Test Results

Simulations are carried out in Matlab 9.1 (R2018A) and Simulink using the fixed step solver $ode4(Runge-Kutta)$. The simulation step size is 0.000001 seconds. In order to validate the system with Simscape model, the same voltage input profile explained in the previous tests are given to the system at no-load and load experiments, respectively. The no-load current output comparison between the test measurements and the model is shown in Figure 4.5 and 4.6.

In Figure 4.5, the phase current values of current sensor and simulation results at the winding B are presented that they are in phase. In Figure 4.6, it is seen that there are certain differences in current values between the sensor and simulation results. These differences are caused by the model in which Simscape blocks are defined as read-only.

Thus, the implementation of the dynamic change of the viscous friction coefficient to the model is denied. Hence, the viscous friction coefficient is defined as a constant value. Also, ESCON's current measurements are not presented with the trapezoidal currents since they are average values and shaped as line. The current sensor and simulation results are presented for all windings in Appendix B.1.

No-load speed output comparison between the experimental tests and the simulation test is shown in Figure 4.7. Both speed outputs and voltage input supplied to both simulation and experimental tests are demonstrated in the same graph. The RMSE between ESCON's speed measurements and the simulation results are 0.0132 rad/s and 0.0038 rad/s at transient and steady state, respectively. Additionally, the combined (transient and steady state) RMSE of the ESCON's speed measurements and the simulation results is calculated as 0.009 rad/s. Hence, no-load speed characteristics of Simscape model are found similar to the no-load speed characteristics of the DC equivalent model as seen in Figure 4.2.

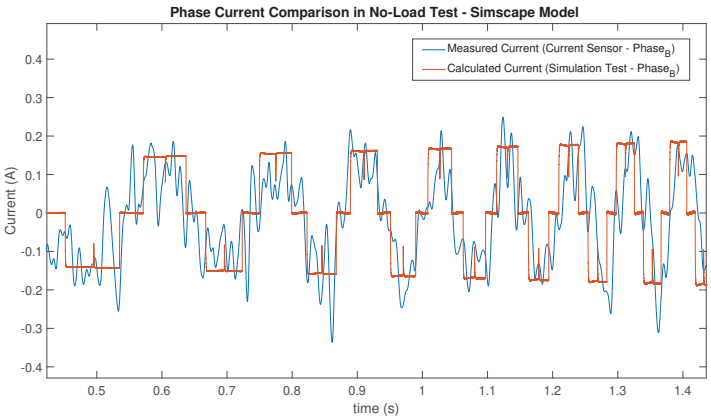

Figure 4.5. Simscape model in phase currents at no-load test on winding B

The load tests are performed by using MR Brake to apply resistive load to the motions of the motor's rotor. Additionally, the coupling is held for short periods of time by a human in order to simulate an unintentional load disturbance due to human robot interaction. The current and speed changes due to the applied resistive torque are investigated. The input to the system is the same voltage input profile explained in the previous tests.

The current output comparison between the test measurements and the model is shown in Figure 4.8 and 4.9. In Figure 4.8, the phase current values of the current sensor and simulation results at the winding B are presented that they are in phase. In Figure 4.9, applied resistive torque which is measured from the torque sensor is demonstrated

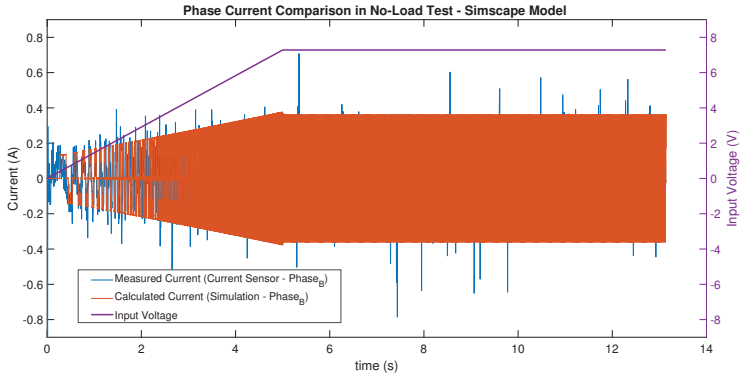

Figure 4.6. Simscape model current results at no-load test on winding B

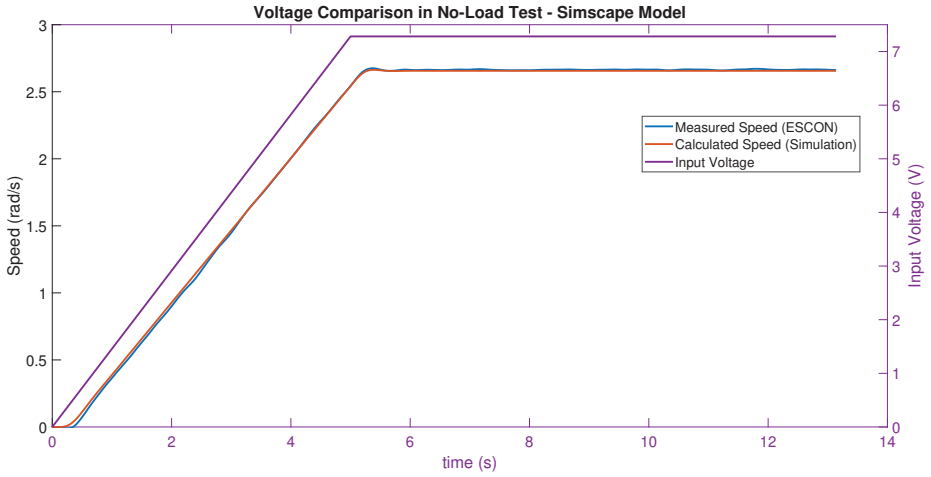

Figure 4.7. Simscape model speed results at no-load test

at the right y-axis in 4.3 since the changes in current and speed are directly related with the applied torque. A resistive torque is applied to the system between the 9^{th} and 15^{th} seconds by MR brake, and resistive torque by the human brake is applied through for 4 times. Similar with the no-load tests, there are certain differences in current values between the sensor and simulation results. As it is stated previously, these differences are caused by the model in which Simscape blocks are defined as read only. Therefore, viscous friction implementation procedure is applied same as in the no-load case. The current sensor and simulation results are presented for all windings in Appendix B.2.

Speed output comparison between the experimental tests and simulation tests under load condition is shown in Figure 4.10. In addition to the intentionally applied torque,

the motor-gear system has a constant load caused by the MR brake's static friction and flexibility of the belt-pulley system. Although the summation of these effects are implemented as load torque in the simulation, there is a delay caused by the dynamics of the system that results latency in the transient response. The RMSE between the ESCON's speed measurement and simulation results is 0.029 rad/s. Although Simscape model has limitations, speed characteristics of Simscape model are found similar to the DC equivalent model in load case.

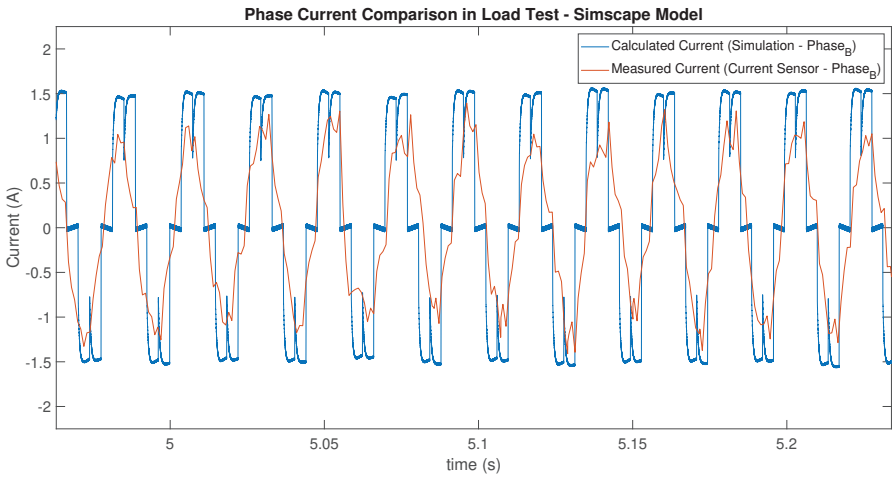

Figure 4.8. Simscape model in phase currents at load test on winding B

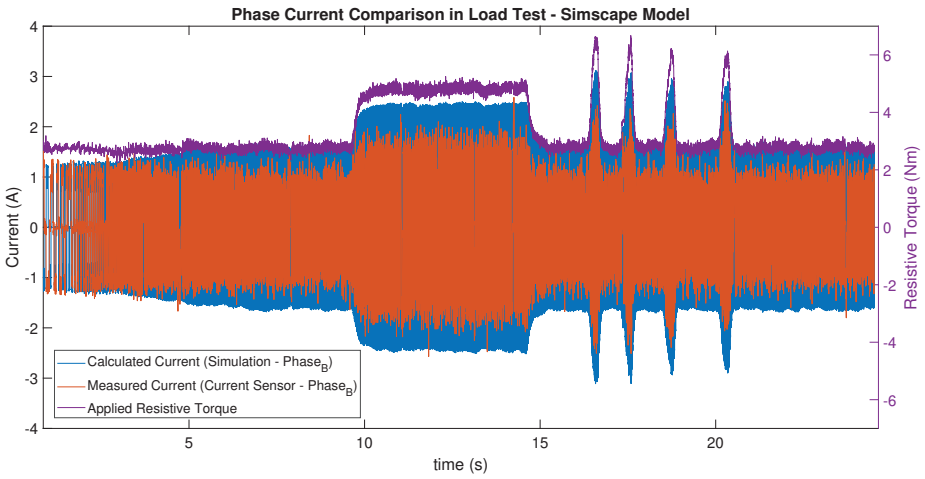

Figure 4.9. Simscape model current results at load test on winding B

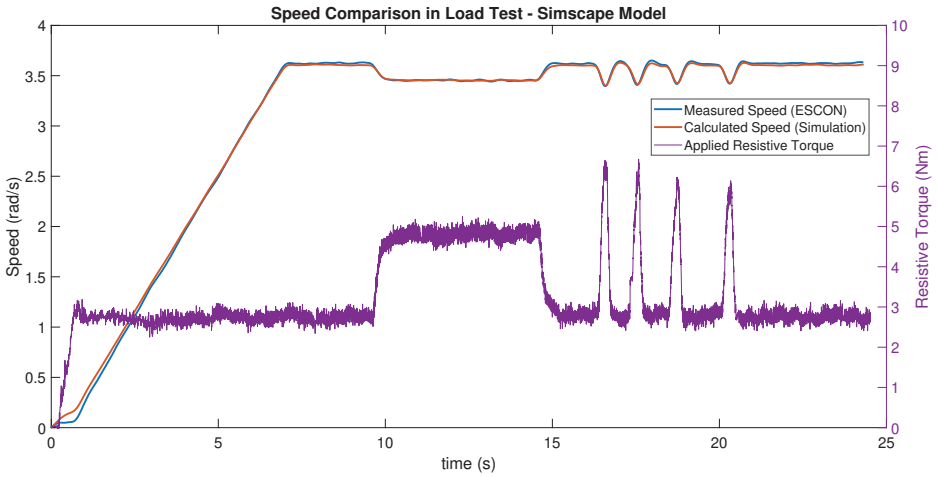

Figure 4.10. Simscape model speed results at load test

4.3. Comprehensive Model Test Results

Simulations are carried out in Matlab 9.1 (R2018A) and Simulink using the fixed step solver $ode4(Runge - Kutta)$. The simulation step size is 0.000001 seconds. In order to validate the system with Comprehensive model, the same voltage input profile explained in the previous tests are given to the system at no-load and load experiments, respectively. The no-load current output comparison between the test measurements and the model is shown in Figure 4.11 and 4.12.

In Figure 4.11, the phase current values of current sensor and simulation results at the winding A are presented that they are in phase. In Figure 4.12, the sensor and simulation results are presented. Although there are differences between measured and calculated currents, these are relatively low differences as they are compared with the Simcape model results shown in 4.6. As it is previously stated, the differences are caused by the limitations of Simscape model. In comprehensive model, the viscous friction coefficient is implemented dynamically. This implementation provides better and more reliable results in terms of currents. The current sensor and simulation results are presented for all windings in Appendix B.3.

No-load speed output comparison between the experimental tests and the simulation test is shown in Figure 4.13. Both speed outputs and voltage input supplied to both simulation and experimental tests are presented in the same graph. The RMSE between ESCON's speed measurements and the simulation results are 0.0134 rad/s and 0.0047

rad/s at transient and steady state, respectively. Additionally, the combined (transient and steady state) RMSE of the ESCON's speed measurements and the simulation results is calculated as 0.0093 rad/s. Hence, no-load speed characteristics of comprehensive model are found similar to the no-load speed characteristics of the DC equivalent and Simscape models as seen in Figure 4.2 and 4.7, respectively.

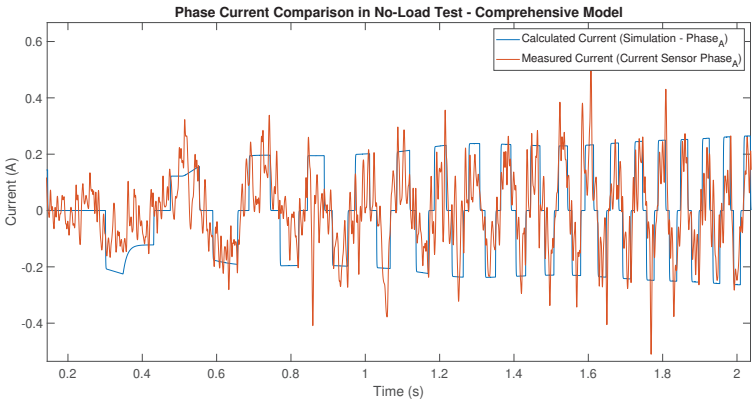

Figure 4.11. Comprehensive model in phase currents at no-load test on winding A

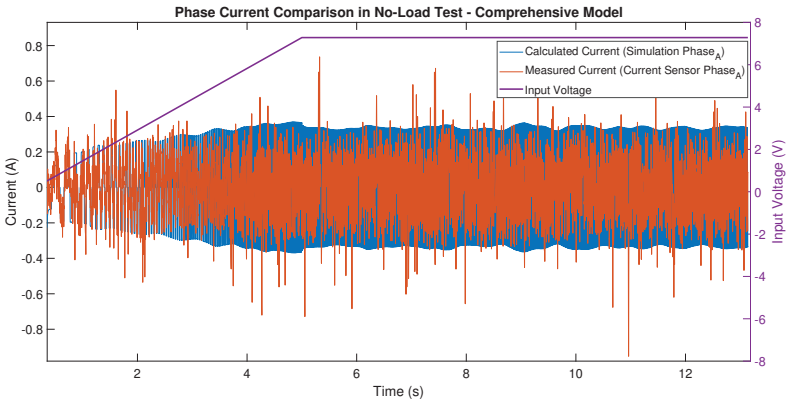

Figure 4.12. Comprehensive model current results at no-load test on winding A

The load tests are performed by holding the coupling for short periods of time by a human in order to simulate an unintentional load disturbance due to human robot interaction. The current and speed changes due to the applied resistive torque are investigated. The input to the system is the same voltage input profile explained in the previous tests.

The current output comparison between the test measurements and the model is shown in Figure 4.14 and 4.15. In Figure 4.14, the phase current values of the current sen-

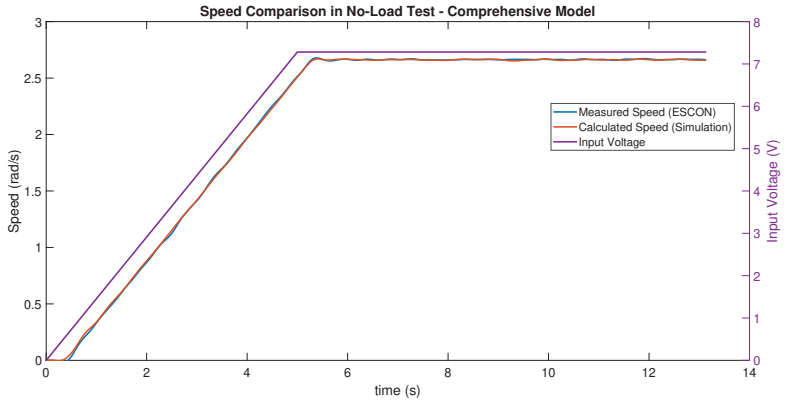

Figure 4.13. Comprehensive model speed results at no-load test

sor and simulation results at the winding A are presented that they are in phase. Applied resistive torque which is measured from the torque sensor is presented at the right y-axis in 4.15 since the changes in current and speed are directly related with the applied torque. A resistive torque is applied through 8 times by the human brake to the system. Similar to the no-load tests, there are differences between measured and calculated currents. These are relatively low differences as they are compared with the Simcape model results shown in 4.9. As it is previously stated, the differences are caused by the limitations of Simscape model. By implementing the viscous friction coefficient dynamically, better and reliable results are obtained in terms of currents. The current sensor and simulation results are presented for all windings in Appendix B.4.

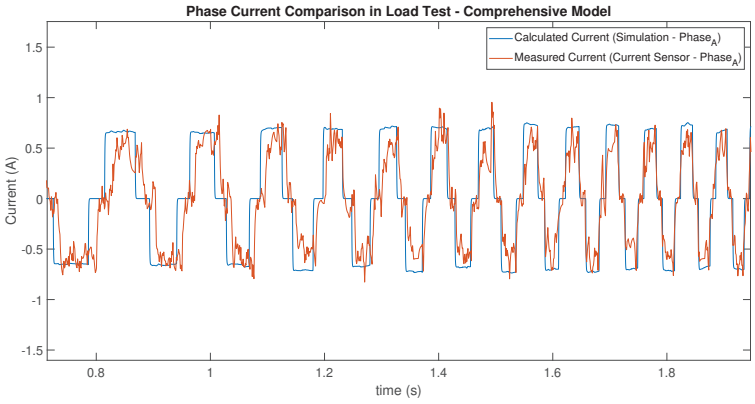

Figure 4.14. Comprehensive model in phase currents at load test on winding A

Speed output comparison between the experimental tests and simulation tests un-

der load condition is shown in Figure 4.16. In addition to the intentionally applied torque, the motor-gear system has a constant load caused by the MR brake's static friction and flexibility of the belt-pulley system. Although the summation of these effects are implemented as load torque in the simulation, there is a delay caused by the dynamics of the system that results latency in the transient response. The RMSE between the ESCON's speed measurement and simulation results is 0.0217 rad/s. In this model, the RMSE of the speed is reduced by the implementation of the viscous friction coeffcient dynamically. Also, comprehensive model is found the most reliable in terms of speed as the RMSE values of the models compared.

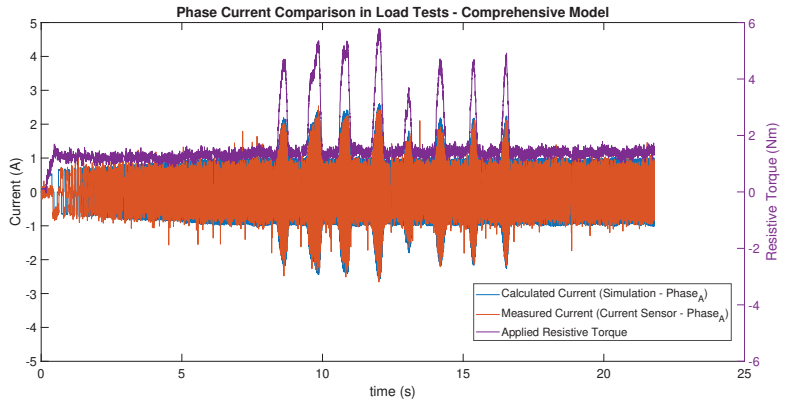

Figure 4.15. Comprehensive model current results at load test on winding A

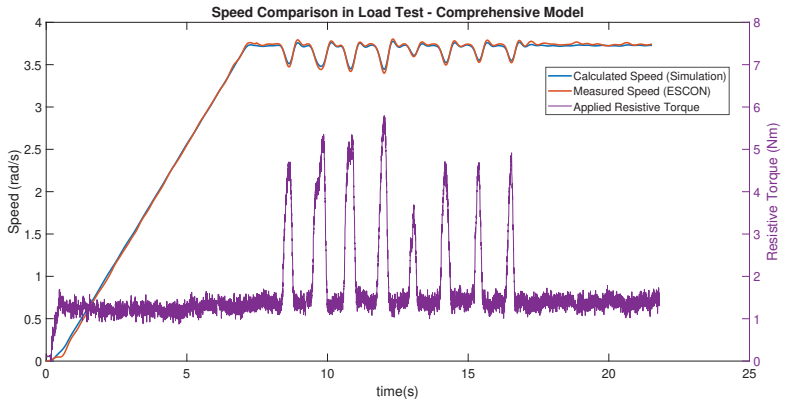

Figure 4.16. Comprehensive model speed results at load test

4.4. Frequency Response Test Results

In addition to the time response tests conducted by three models, frequency response tests are performed in order to validate the system. The BLDC-gear system with an external load is as shown in Figure 4.17. However, frequency response tests are performed without load.

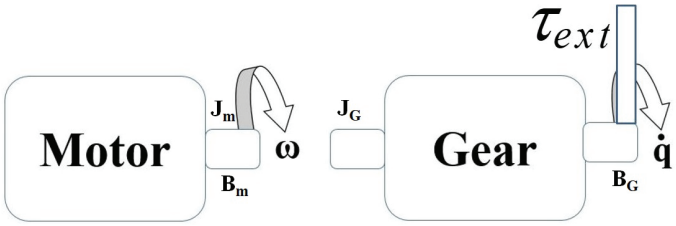

Figure 4.17. The motor gear system

The relationship between the speed of the motor shaft ω and the gear output shaft $\dot{q}$ is given in Equation 4.1.

$$\omega = N\dot{q} \rightarrow \dot{\omega} = N\ddot{q} \tag{4.1}$$

In Equation 4.1, N, $\frac{338}{3}$, is the reduction ratio of the planetary gear. $\dot{\omega}$, $\ddot{q}$, ω and $\dot{q}$ are the acceleration of the motor, acceleration of the gear output, speed at the motor's output shaft, and speed at the gear's output shaft, respectively.

According to the Maxon Motor Catalog (2018), the gear moment of inertia as is given as measured at the gear's input shaft. Gear's viscous friction coefficient is also selected to be measured with respect to the gear's input shaft speed, which is the speed of the motor's output shaft since there is a rigid coupling between the motor's output shaft and the gear's input shaft. In order to conveniently present dynamic equations, all parameters are given corresponding to the motor shaft motion in the Equation 4.2.

$$(J_m\dot{\omega}_m + B_m\omega_m) + (J_G\dot{\omega}_m + B_G\omega_m) = k_t i - T_f - \frac{T_{ext}}{N} \tag{4.2}$$

In Equation 4.2, J_m, J_G, B_m, and B_G are the inertia of the motor, inertia of the gear, viscous friction coefficient of the motor and viscous friction coefficient of the gear at the gear's input shaft, respectively. T_{ext}, N, and k_t are the external load applied to the system, reduction ratio of the gear and the torque constant of the motor, respectively. The torque loss due to the Coulomb friction is calculated experimentally as T_f=2.436 mNm. The

overall equation of the system with respect to the motor output shaft is shown in Equation 4.3.

$$\dot{\omega}_m(J_m + J_G) + \omega_m(B_m + B_G) = k_t i - T_f \tag{4.3}$$

Combining the moment of inertia and the viscous friction coefficient parameters and applying the Laplace transform to the aforementioned equation, the transfer function between the current input and speed output is written in Equation 4.4

$$\frac{\Omega(s)}{I(s)} = \frac{k_t}{J^\star s + B^\star} \tag{4.4}$$

In Equation 4.4, $J^\star$ and $B^\star$ are the combined moment of inertia and combined viscous friction coefficient of the BLDC-gear system, respectively.

The frequency response of the system is investigated for the current input and speed output at no load condition. The current with a constant amplitude of 0.3 A for a range of varying frequencies is given as input. A bias current, which changes sign depending on the direction of motion, is added to the input current which corresponds to the measured Coulomb friction. Then, the speed output is measured and recorded. The amplitude of the output speed corresponding to different frequencies are obtained and presented in Table C.1 at Appendix C. According to the current input - speed output results, Bode diagram of the system is obtained as shown in Figure 4.18.

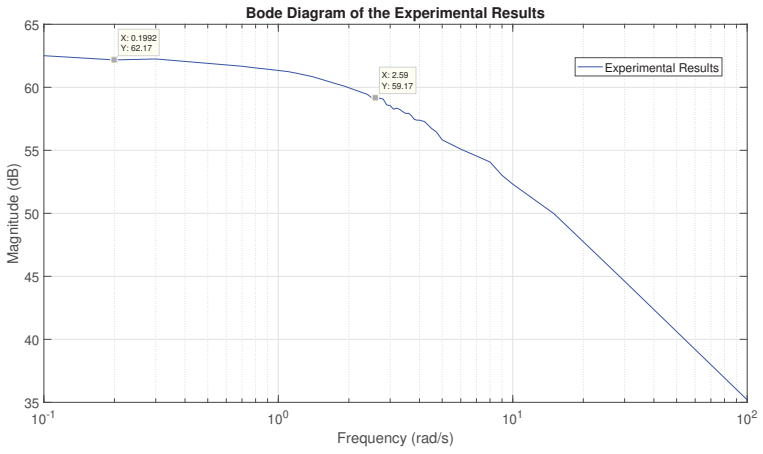

Figure 4.18. Bode diagram of the experimental test

Gain and cut-off frequency are determined as 62.17 dB and 2.59 rad/s from the Bode plot. Accordingly, parameters of the transfer function presented in Equation 4.4 are

obtained by using Equation 4.5.

$$\begin{aligned} 20log(\frac{k_t}{B^\star}) &= 62.17dB \\ \frac{B^\star}{J^\star} &= 2.59rad/s \end{aligned} \tag{4.5}$$

The model parameters are calculated as $B^\star = 1.8\ 10^{-5} Nms/rad$ and $J^\star = 6.95\ 10^{-6} kgm^2$. The transfer function estimated from the experimental results is given in Equation 4.6. In formation of this transfer function the torque constant (k_t) is used directly as its catalog value.

$$\frac{\Omega(s)}{I(s)} = \frac{2.32}{0.0695s + 0.18} \tag{4.6}$$

The Bode diagram of the experimental results and estimated results are sketched together in Figure 4.19.

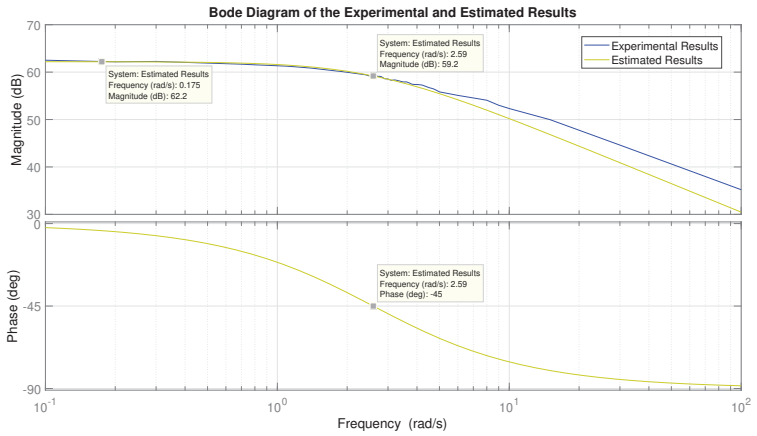

Figure 4.19. Bode diagram of the experimental tests and their estimation

According to the catalog values of the BLDC motor and planetary gear in Maxon Motor Catalog (2018), the current input - speed output transfer function of the system is calculated as presented in Equation 4.7. In this presentation, the viscous friction coefficient that is estimated during the experiments is used since this parameter does not appear in the specification sheets of the motor and the gear.

$$\frac{\Omega(s)}{I(s)} = \frac{2.32}{0.0631s + 0.18} \tag{4.7}$$

The Bode diagram of the estimated transfer function and calculated transfer function are sketched together in Figure 4.20.

Response of the calculated and measured results for a range of frequencies between 0.1 rad/s and 8 rad/s are presented in Figure C.1 through C.15 in Appendix C.

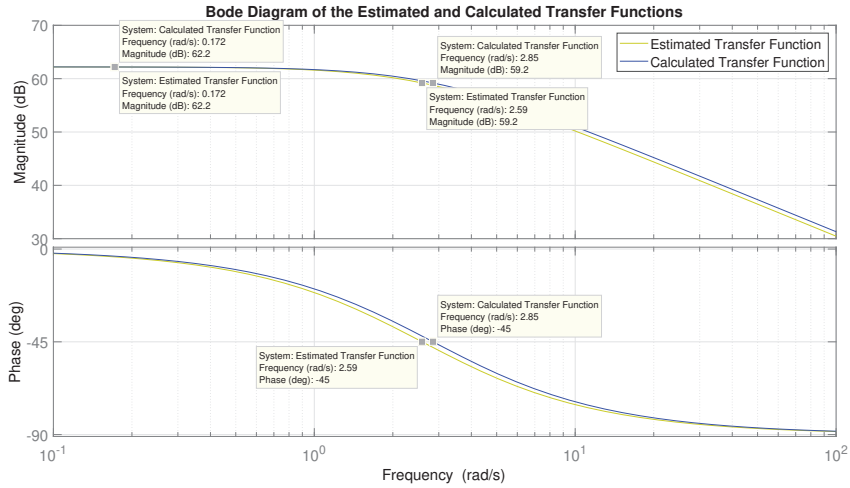

Figure 4.20. Bode diagram of estimated and calculated transfer functions

CHAPTER 5

CONCLUSIONS

Collaborative robots are the new co-workers of the human in industrial automation. They are versatile and light-weight robots when compared to the traditional industrial robots. Safety is an indispensable factor in collaborative robot applications, and ISO has produced new standards in order to provide additional safety.

In this thesis, analysis, modeling and experimental verification of an actuation system to be used in a light-weight collaborative robot are aimed. For this purpose, a variety of actuation systems and their components are investigated. Joint torque controlled actuation scheme is selected because of its modular structure, relatively better performance metrics and safety ratings. Accordingly, an actuation system that resembles Universal Robot's UR5 robot actuation system is selected to be studied.

An experimental test setup with a BLDC motor, a planetary gearhead, an encoder, and a torque sensor, is configured in order to model the actuation system, and verify the model through experimentation. Additionally, a magneto-rheological (MR) brake and a belt-pulley system are used in order to provide resistive torque as a load on the system. In addition to MR brake, the resistive load is applied by manually holding the coupling between the large pulley's output shaft and the torque sensor's output shaft for short periods of time. Thus, an unintentional load resembling a possible human-robot interaction is simulated. During the experimental and simulation tests, current-speed and voltage-speed-current relationships are investigated. The supplied current to the system is measured by ESCON controller and current sensors placed on the motor windings in series. Additionally, speed of the motor shaft is calculated by ESCON controller through measurements received from the encoder attached to the rear end of the motor.

A total of four simulation models are developed in order to analyze the actuation system. According the these models, specific tests are conducted in both load and no-load conditions. Also, frequency response test is performed in no-load condition. The given inputs and measured results are recorded. Then, same inputs are used in simulation tests, and simulation results are compared with the experimental results for the validation of models.

In no-load tests, a specific input voltage is supplied to the system, and supplied current and motor's output shaft's speed is compared between the ESCON measurement

results and simulation test results. In DC equivalent model, according to the RMSE values of the supplied current and the output speed, the differences between the simulation results and ESCON's current and speed measurement results are at reasonable ranges since they are within the tolerance of $\pm 50\%$ and $\pm 10\%$, which are specified in the motor's specification sheet, respectively. In Simscape and comprehensive models, average current calculations received from ESCON are not used but the measurements received from the current sensor are compared with the simulation results since both provide phase current in trapezoidal waveforms. In Simscape model, there are larger differences between the simulation results and current sensor results due to the limitations caused by Simscape blocks when compared with DC equivalent model. The dynamic changes of the viscous friction coefficient is not implemented in this case. However, the viscous friction effect can be implemented as an external load, and the model can be improved as a future work. In comprehensive model, the current differences between the sensor and simulation results are lower than the Simscape model since dynamic change of viscous friction coefficient is implemented in this model. On the other hand, errors in calculation of the motor's output shaft's speed with Simscape model and the comprehensive models show similarities with DC equivalent model results. When the models are compared, DC equivalent and comprehensive models provide more reliable results than Simscape model in terms of currents in no load tests. However, all three models give similar and reliable speed output results. According to the calculated RMSE values, the comprehensive model provides the closest results to the experimental test results. Also, DC equivalent model provides better results than Simscape model in terms of output speed results.

The tests are also performed at load condition. In DC equivalent test, there are considerably larger errors between the results calculated from the simulation test and the measured results for supplied current. These differences are caused by ESCON controller since the controller gives average values of the current signal. Nevertheless, the trend of the supplied current throughout the tests are similar. Similar to the no-load tests, there are larger differences between the current sensor measurements and simulation results received from Simscape model. The model's results can also be improved by adding the dynamic change in viscous friction as an external load to the system. In comprehensive model, current sensor measurements and simulation results are closer to each other when compared with the results obtained from the simulation tests with the Simscape model. On the other hand, speed characteristics of the models under load condition are similar to each other. Same as the no-load case, the comprehensive model provides the closest results to the experimental test results when the speed output RMSE are compared. Also,

DC equivalent model provide better results than Simscape model in terms of output speed results.

In conclusion, DC equivalent and comprehensive models are preferable with respect to the Simscape model. DC equivalent model is a reduced model and it is easy to implement. On the other hand, the comprehensive model, as the name implies, is a detailed model of three-phase BLDC motor configuration. It provides not only the closest results to the experimental results but it also provides additional information about the system such as phase currents and stator's back EMF voltages. Future works of this study includes the controller design based on the procured models which would possibly lead the way to designing compliance control for the actuation system to be used in human-robot interaction scenarios.

REFERENCES

Albu-Schäffer, A., S. Haddadin, C. Ott, A. Stemmer, T. Wimböck, and G. Hirzinger (2007). The dlr lightweight robot: design and control concepts for robots in human environments. *Industrial Robot: the international journal of robotics research and application 34*(5), 376–385.

Allegromicro (2018). Allegro MicroSystems, LLC, https://www.allegromicro.com/.

Anaheim Automation (2018). Anaheim Automation website, https://www.anaheimautomation.com/manuals/forms/encoder-guide.php.

Angerer, A., C. Ehinger, A. Hoffmann, W. Reif, and G. Reinhart (2011). Design of an automation system for preforming processes in aerospace industries. *2011 IEEE International Conference on Automation Science and Engineering*, 557–562.

ANYbotics (2018). ANYbotics website, https://www.anybotics.com/anydrive/.

Appo, M. (2018). Hardware-agnostic compliant control ros package for collaborative industrial manipulators. Master's thesis, University of Tartu, Faculty of Science and Technology, Institute of Technology.

Ashby, G. and G. M. Bone (2016, July). Improved hybrid pneumatic-electric actuator for robot arms. In *2016 IEEE International Conference on Advanced Intelligent Mechatronics (AIM)*, pp. 100–106.

Bischoff, R., J. Kurth, G. Schreiber, R. Koeppe, A. Albu-Schaeffer, A. Beyer, O. Eiberger, S. Haddadin, A. Stemmer, G. Grunwald, and G. Hirzinger (2010, June). The kuka-dlr lightweight robot arm - a new reference platform for robotics research and manufacturing. In *ISR 2010 (41st International Symposium on Robotics) and ROBOTIK 2010 (6th German Conference on Robotics)*, pp. 1–8.

Bodie, K., C. D. Bellicoso, and M. Hutter (2016, Oct). Anypulator: Design and control of a safe robotic arm. In *2016 IEEE/RSJ International Conference on Intelligent Robots and Systems (IROS)*, pp. 1119–1125.

Bogue, R. (2016). Europe continues to lead the way in the collaborative robot business. *Industrial Robot: the international journal of robotics research and application 43*(1), 6–11.

Bone, G. M. and X. Chen (2012, June). Position control of hybrid pneumatic-electric actuators. In *2012 American Control Conference (ACC)*, pp. 1793–1799.

Brown, W. (2002). Brushless DC Motor Control Made Easy, ww1.microchip.com/downloads/en/appnotes/00857a.pdf.

Campbell, K. (2017). High-speed induction motor with an integrated gearbox for propulsion. G2 pro gradu, diplomityö.

CLR (2018). CLR website, https://clr.es/blog/en/electrical-actuators-robotics/.

Cranes Today (2003). Stanley moves into materials handling with Cobotics acquisition, http://www.cranestodaymagazine.com/news/stanley-moves-into-materials-handling-with-cobotics-acquisition.

D. Vischer and O. Khatib (1995). Design and development of high-performance torque-controlled joints. *IEEE Transactions on Robotics and Automation 11*(4), 537–544.

Fanuc (2018). Fanuc website, https://www.fanuc.com/.

Fernández, J., H. Sprengel, M. Mallwitz, M. Zipper, B. Yu, and V. Bargsten (2016, 10). *Designing Modular Series-Elastic Actuators For Safe Human-Robot Collaboration In Industrial Settings: Proceedings of the 19th International Conference on CLAWAR 2016*, pp. 135–142.

Franka Emika (2018). Franka Emika website, https://www.franka.de/.

Futek (2018). Futek website, http://www.futek.com/index.aspx.

Greenfield, D. (2017). Automation World, https://www.automationworld.com/choosing-between-cobots-and-industrial-robots.

Guizzo, E. and E. Ackerman (2012, October). The rise of the robot worker. *IEEE Spectrum 49*(10), 34–41.

Haddadin, S., A. D. Luca, and A. Albu-Schäffer (2017, Dec). Robot collisions: A survey on detection, isolation, and identification. *IEEE Transactions on Robotics 33*(6), 1292–1312.

Harnefors, L. (2002). *Control of Variable-speed Drives*. Applied Signal Processing and Control, Department of Electronics, Mälardalen University.

Hirzinger, G., A. Albu-Schaffer, M. Hahnle, I. Schaefer, and N. Sporer (2001, May). On a new generation of torque controlled light-weight robots. In *Proceedings 2001 ICRA. IEEE International Conference on Robotics and Automation (Cat. No.01CH37164)*, Volume 4, pp. 3356–3363 vol.4.

Hirzinger, G., J. Butterfafl, M. Fischer, M. Grcbenstein, I. Schaefer, N. Sporer, and G. Ae (2000). A mechatronics approach to the design of lightweight arms and multifingered hands. In *Proceedings of the IEEE International Conference on Robotics and Automation (ICRA*, pp. 46–54.

Hirzinger, G., N. Sporer, M. Schedl, J. Butterfaß, and M. Grebenstein (2004). Torque-controlled lightweight arms and articulated hands: Do we reach technological limits now? *The International Journal of Robotics Research 23*(4-5), 331–340.

Humusoft (2018). Humusoft^{TM}website, https://www.humusoft.cz/datacq/.

IFR (2012). International Federation of Robotics, History of Industrial Robots - From the first installation until today. Brochure.

Jabil (2018). Industrial Robot Applications, https://www.jabil.com/insights/blog-main/ten-popular-industrial-robot-applications.html.

Karabulut, G. (2017). Development of mr-fluid based semi-active dampers to be used in haptic devices. Master's thesis, İzmir Institute of Technology.

KEB (2018). KEB Electromagnetic Brakes, https://kebblog.com/how-it-works-power-on-brake/.

Khader, M. (2018). Electronics Design, https://www.electronicdesign.com/analog/hall-effect-sensing-makes-sense-building-automation-portables.

Kinova (2018). Kinova website, https://www.kinovarobotics.com/en/.

KUKA (2018). KUKA website, https://www.kuka.com/en-us.

Lens, T., J. Kunz, O. v. Stryk, C. Trommer, and A. Karguth (2010, June). Biorob-arm: A quickly deployable and intrinsically safe, light- weight robot arm for service robotics applications. In *ISR 2010 (41st International Symposium on Robotics) and ROBOTIK 2010 (6th German Conference on Robotics)*, pp. 1–6.

Lewotsky, K. (2012). Resolvers Track Motion in Harsh Environments, https://www.motioncontrolonline.org/content-detail.cfm/motion-control-technical-features/resolvers-track-motion-in-harsh-environments/content-id/850.

Mathijssen, G., R. Furnémont, R. Van Ham, D. Lefeber, and B. Vanderborght (2014, 06). From series elastic actuation to series-parallel elastic actuation.

Maxon Formulae Handbook (2018). Maxon Formulae Handbook, maxon motor ag website, https://www.maxonmotor.com/maxon/view/news/medienmitteilung-formelsammlung.

Maxon Motor Catalog (2018). Maxon Motor AG Product Catalog website, https://www.maxonmotor.com/maxon/view/catalog/.

Nabstecco (2018). Nabstecco website, https://www.nabtesco.de/fileadmin/user-upload/downloads/produkt-kataloge nab-uebersichtsbr-en-web.pdf.

Onvio (2018). Onvio website, https://www.onviollc.com/planetary-vs-cycloidal-gearbox-technology-component-case-studies/.

Peshkin, M. and J. E. Colgate (1999). Cobots. *Industrial Robot: An International*

Journal 26(5), 335–341.

Rader, S., L. Kaul, P. Weiner, and T. Asfour (2017, July). Highly integrated sensor-actuator-controller units for modular robot design. In *2017 IEEE International Conference on Advanced Intelligent Mechatronics (AIM)*, pp. 1160–1166.

Rethink (2018). Rethink Robotics website, https://www.rethinkrobotics.com/.

Robotiq (2018). Robotiq website, https://blog.robotiq.com.

Rodi, A., B. Miloradovi, and S. Popi (2014). On developing lightweight robot-arm of anthropomorphic characteristics.

Sen, P. (1997). *Principles of Electric Machines and Power Electronics*. Wiley.

Sensinger, J. W. and J. H. Lipsey (2012, May). Cycloid vs. harmonic drives for use in high ratio, single stage robotic transmissions. In *2012 IEEE International Conference on Robotics and Automation*, pp. 4130–4135.

Shea, R. N. (2016). Collaborative Robot Technical Specification ISO/TS 15066 Update.

Shikany, A. (2014). Collaborative Robots - End User Industry Insights.

Shin, D., I. Sardellitti, and O. Khatib (2008, May). A hybrid actuation approach for human-friendly robot design. In *2008 IEEE International Conference on Robotics and Automation*, pp. 1747–1752.

Shin, D., I. Sardellitti, Y.-L. Park, O. Khatib, and M. Cutkosky (2010). Design and control of a bio-inspired human-friendly robot. *The International Journal of Robotics Research 29*(5), 571–584.

Singh, B., N. Sellappan, and Kumaradhas (2013). Evolution of Industrial Robots and their Applications.

Sondkar, P. and A. Kahraman (2013). A dynamic model of a double-helical planetary gear set. *Mechanism and Machine Theory 70*, 157 – 174.

Stanford Robotics (2018). Human Friendly Robot Design, https://cs.stanford.edu/groups/manips/projects/humanfriendlyrobotics.html.

Takemura, F., S. R. Pandian, Y. Nagase, H. Mizutani, Y. Hayakawa, and S. Kawamura (2000, Oct). Control of a hybrid pneumatic/electric motor. In *Proceedings. 2000 IEEE/RSJ International Conference on Intelligent Robots and Systems (IROS 2000) (Cat. No.00CH37113)*, Volume 1, pp. 209–214 vol.1.

Testa, G. (2017). Experimental stiffness identification in the joints of a lightweight robot.

Texas Instruments (1997). DSP Solutions for BLDC Motors, www.ti.com/lit/an/bpra055/bpra055.pdf.

T&M World (2018). Test and Measurement World, http://www.test-and-measurement-world.com/terminology/dc-tachometer-generator-vs-ac-tachometer-generator.html.

Universal Robots (2018). Universal Robots website, https://www.universal-robots.com/.

Van, J. (1996). Mechanical Advantage, Chicago Tribune, https://www.chicagotribune.com/news/ct-xpm-1996-12-11-9612110101-story.htm.

Yedamale, P. (2003). Brushless DC Motor Fundamentals, ww1.microchip.com/downloads/en/appnotes/00885a.pdf.

Zinn, M., O. Khatib, and B. Roth (2004, April). A new actuation approach for human friendly robot design. In *IEEE International Conference on Robotics and Automation, 2004. Proceedings. ICRA '04. 2004*, Volume 1, pp. 249–254 Vol.1.

APPENDIX A

TECHNICAL SPECIFICATIONS OF MAXON BLDC MOTOR, PLANETARY GEARHEAD AND ENCODER

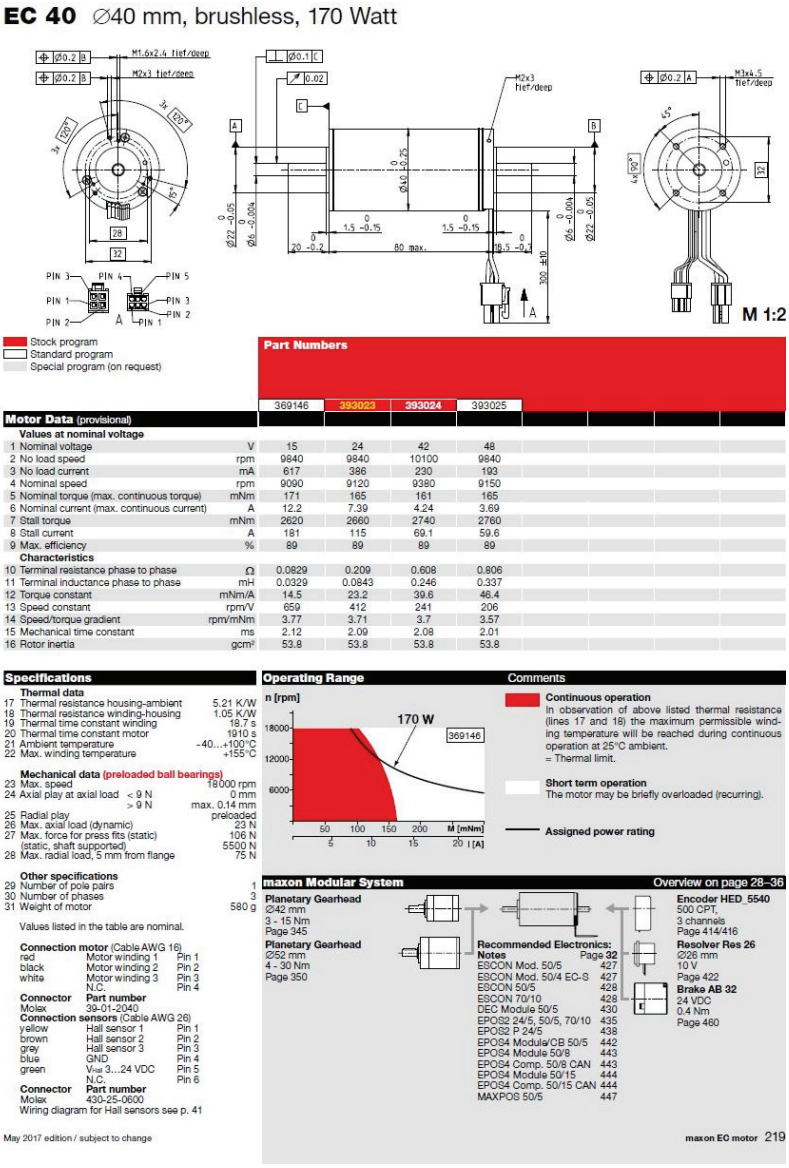

EC 40 ∅40 mm, brushless, 170 Watt

M 1:2

Stock program
Standard program
Special program (on request)

Part Numbers

		369146	393023	393024	393025
Motor Data (provisional)					
Values at nominal voltage					
1 Nominal voltage	V	15	24	42	48
2 No load speed	rpm	9840	9840	10100	9840
3 No load current	mA	617	386	230	193
4 Nominal speed	rpm	9090	9120	9380	9150
5 Nominal torque (max. continuous torque)	mNm	171	165	161	165
6 Nominal current (max. continuous current)	A	12.2	7.39	4.24	3.69
7 Stall torque	mNm	2620	2660	2740	2760
8 Stall current	A	181	115	69.1	59.6
9 Max. efficiency	%	89	89	89	89
Characteristics					
10 Terminal resistance phase to phase	Ω	0.0829	0.209	0.608	0.806
11 Terminal inductance phase to phase	mH	0.0329	0.0843	0.246	0.337
12 Torque constant	mNm/A	14.5	23.2	39.6	46.4
13 Speed constant	rpm/V	659	412	241	206
14 Speed/torque gradient	rpm/mNm	3.77	3.71	3.7	3.57
15 Mechanical time constant	ms	2.12	2.09	2.08	2.01
16 Rotor inertia	gcm²	53.8	53.8	53.8	53.8

Specifications

Thermal data

17	Thermal resistance housing-ambient	5.21 K/W
18	Thermal resistance winding-housing	1.05 K/W
19	Thermal time constant winding	18.7 s
20	Thermal time constant motor	1910 s
21	Ambient temperature	-40...+100°C
22	Max. winding temperature	+155°C

Mechanical data (preloaded ball bearings)

23	Max. speed		18000 rpm
24	Axial play at axial load	< 9 N	0 mm
		> 9 N	max. 0.14 mm
25	Radial play		preloaded
26	Max. axial load (dynamic)		23 N
27	Max. force for press fits (static)		106 N
	(static, shaft supported)		5500 N
28	Max. radial load, 5 mm from flange		75 N

Other specifications

29	Number of pole pairs	1
30	Number of phases	3
31	Weight of motor	580 g

Values listed in the table are nominal.

Connection motor (Cable AWG 16)

red	Motor winding 1	Pin 1
black	Motor winding 2	Pin 2
white	Motor winding 3	Pin 3
	N.C.	Pin 4

Connector Molex **Part number** 39-01-2040

Connection sensors (Cable AWG 26)

yellow	Hall sensor 1	Pin 1
brown	Hall sensor 2	Pin 2
grey	Hall sensor 3	Pin 3
blue	GND	Pin 4
green	V_{Hall} 3...24 VDC	Pin 5
	N.C.	Pin 6

Connector Molex **Part number** 430-25-0600

Wiring diagram for Hall sensors see p. 41

Operating Range

Comments

Continuous operation
In observation of above listed thermal resistance (lines 17 and 18) the maximum permissible winding temperature will be reached during continuous operation at 25°C ambient.
= Thermal limit.

Short term operation
The motor may be briefly overloaded (recurring).

Assigned power rating

maxon Modular System Overview on page 28–36

Planetary Gearhead
∅42 mm
3 - 15 Nm
Page 345

Planetary Gearhead
∅52 mm
4 - 30 Nm
Page 350

Recommended Electronics:

Notes	Page 32
ESCON Mod. 50/5	427
ESCON Mod. 50/4 EC-S	427
ESCON 50/5	428
ESCON 70/10	428
DEC Module 50/5	430
EPOS2 24/5, 50/5, 70/10	435
EPOS2 P 24/5	438
EPOS4 Module/CB 50/5	442
EPOS4 Module 50/8	443
EPOS4 Comp. 50/8 CAN	443
EPOS4 Module 50/15	444
EPOS4 Comp. 50/15 CAN	444
MAXPOS 50/5	447

Encoder HED_5540
500 CPT,
3 channels
Page 414/416

Resolver Res 26
∅26 mm
10 V
Page 422

Brake AB 32
24 VDC
0.4 Nm
Page 460

May 2017 edition / subject to change

Figure A.1. Maxon EC 40, 170 Watt Brushless DC motor Specifications

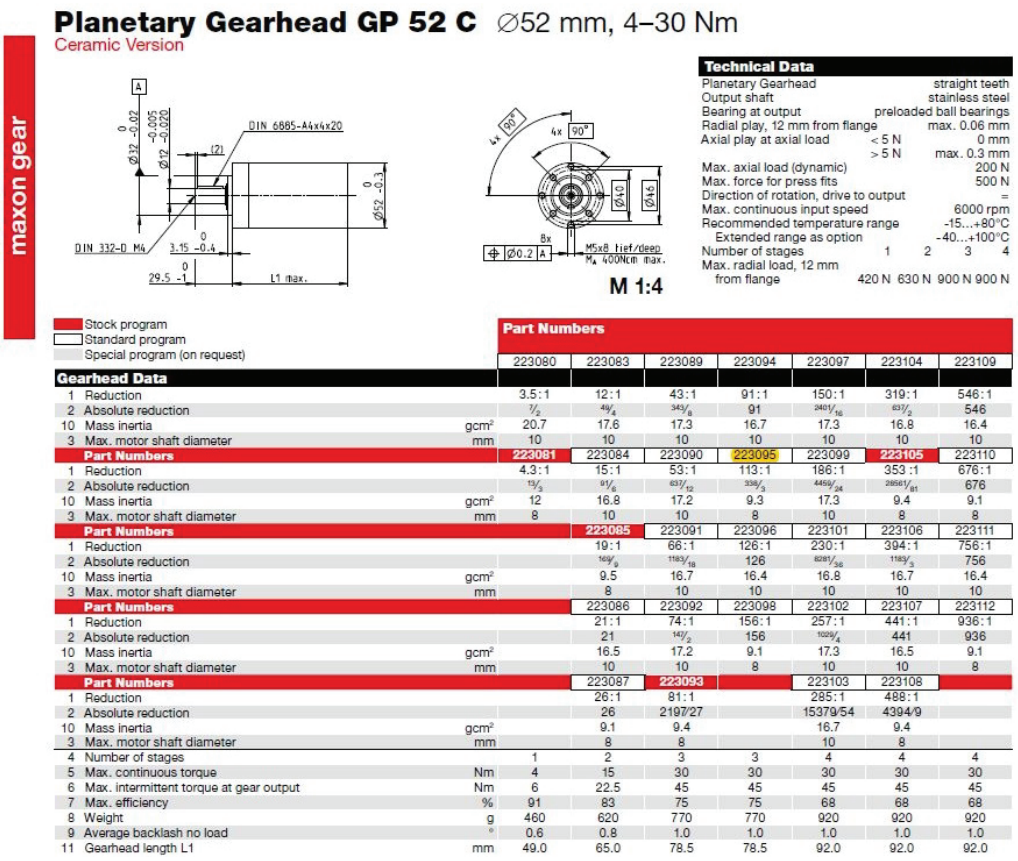

Planetary Gearhead GP 52 C ∅52 mm, 4–30 Nm

Ceramic Version

maxon gear

Technical Data

Planetary Gearhead	straight teeth
Output shaft	stainless steel
Bearing at output	preloaded ball bearings
Radial play, 12 mm from flange	max. 0.06 mm
Axial play at axial load	< 5 N 0 mm
	> 5 N max. 0.3 mm
Max. axial load (dynamic)	200 N
Max. force for press fits	500 N
Direction of rotation, drive to output	=
Max. continuous input speed	6000 rpm
Recommended temperature range	-15...+80°C
Extended range as option	-40...+100°C
Number of stages	1 2 3 4
Max. radial load, 12 mm from flange	420 N 630 N 900 N 900 N

Stock program
Standard program
Special program (on request)

			Part Numbers					
			223080	223083	223089	223094	223097	223104	223109
Gearhead Data									
1	Reduction		3.5:1	12:1	43:1	91:1	150:1	319:1	546:1
2	Absolute reduction		7/2	49/4	343/8	91	2401/16	637/2	546
10	Mass inertia	gcm²	20.7	17.6	17.3	16.7	17.3	16.8	16.4
3	Max. motor shaft diameter	mm	10	10	10	10	10	10	10
	Part Numbers		**223081**	223084	223090	223095	223099	**223105**	223110
1	Reduction		4.3:1	15:1	53:1	113:1	186:1	353 :1	676:1
2	Absolute reduction		13/3	91/6	637/12	339/3	4459/24	28561/81	676
10	Mass inertia	gcm²	12	16.8	17.2	9.3	17.3	9.4	9.1
3	Max. motor shaft diameter	mm	8	10	10	8	10	8	8
	Part Numbers			**223085**	223091	223096	223101	223106	223111
1	Reduction			19:1	66:1	126:1	230:1	394:1	756:1
2	Absolute reduction			169/9	1183/18	126	8281/36	1183/3	756
10	Mass inertia	gcm²		9.5	16.7	16.4	16.8	16.7	16.4
3	Max. motor shaft diameter	mm		8	10	10	10	10	10
	Part Numbers			223086	223092	223098	223102	223107	223112
1	Reduction			21:1	74:1	156:1	257:1	441:1	936:1
2	Absolute reduction			21	147/2	156	1029/4	441	936
10	Mass inertia	gcm²		16.5	17.2	9.1	17.3	16.5	9.1
3	Max. motor shaft diameter	mm		10	10	8	10	10	8
	Part Numbers			223087	**223093**		223103	223108	
1	Reduction			26:1	81:1		285:1	488:1	
2	Absolute reduction			26	2197/27		15379/54	4394/9	
10	Mass inertia	gcm²		9.1	9.4		16.7	9.4	
3	Max. motor shaft diameter	mm		8	8		10	8	
4	Number of stages		1	2	3	3	4	4	4
5	Max. continuous torque	Nm	4	15	30	30	30	30	30
6	Max. intermittent torque at gear output	Nm	6	22.5	45	45	45	45	45
7	Max. efficiency	%	91	83	75	75	68	68	68
8	Weight	g	460	620	770	770	920	920	920
9	Average backlash no load	°	0.6	0.8	1.0	1.0	1.0	1.0	1.0
11	Gearhead length L1	mm	49.0	65.0	78.5	78.5	92.0	92.0	92.0

Figure A.2. Maxon Planetary Gearhead GP 52 C, 4–30 Nm Specifications

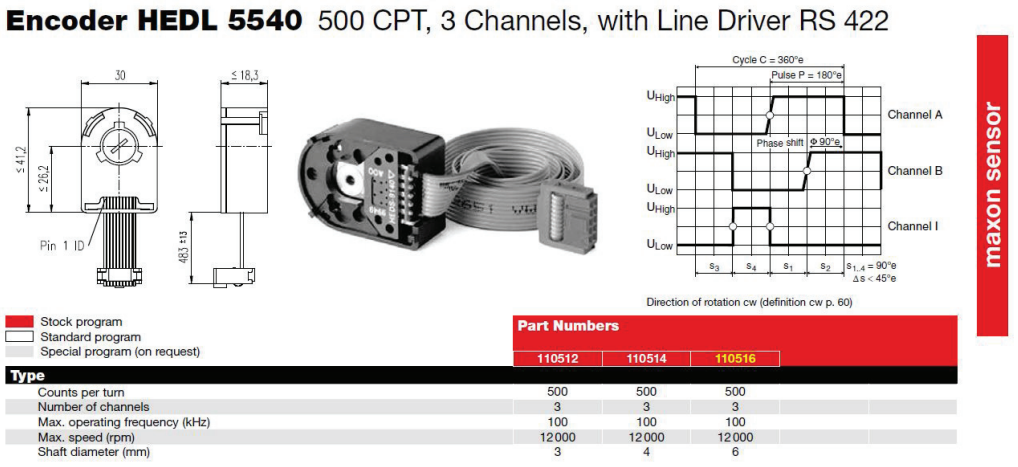

Encoder HEDL 5540 500 CPT, 3 Channels, with Line Driver RS 422

maxon sensor

Stock program
Standard program
Special program (on request)

	Part Numbers		
	110512	110514	110516
Type			
Counts per turn	500	500	500
Number of channels	3	3	3
Max. operating frequency (kHz)	100	100	100
Max. speed (rpm)	12000	12000	12000
Shaft diameter (mm)	3	4	6

Figure A.3. Maxon Encoder HEDL 5540 500 CPT, 3 Channels, with Line Driver RS 422

APPENDIX B

MODELED AND MEASURED PHASE CURRENT RESULTS IN SIMSCAPE AND COMPREHENSIVE MODELS

Figures related with the phase currents in Simscape and Comprehensive models are presented in this section.

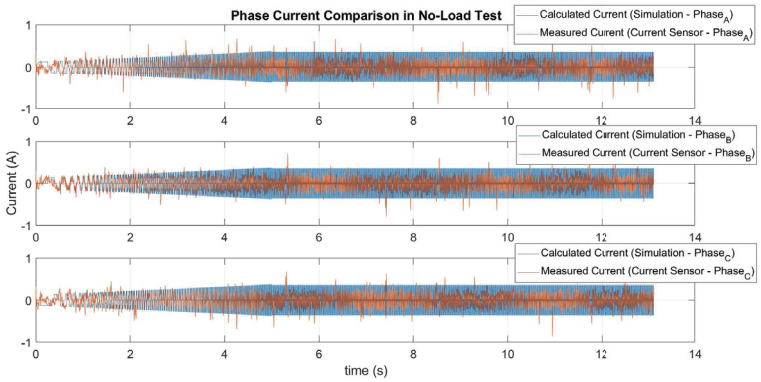

Figure B.1. Current comparison at no-load test - Simscape model

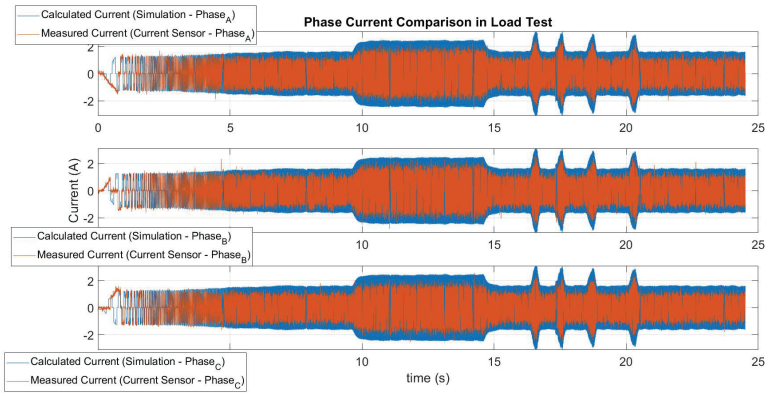

Figure B.2. Current comparison at load test - Simscape model

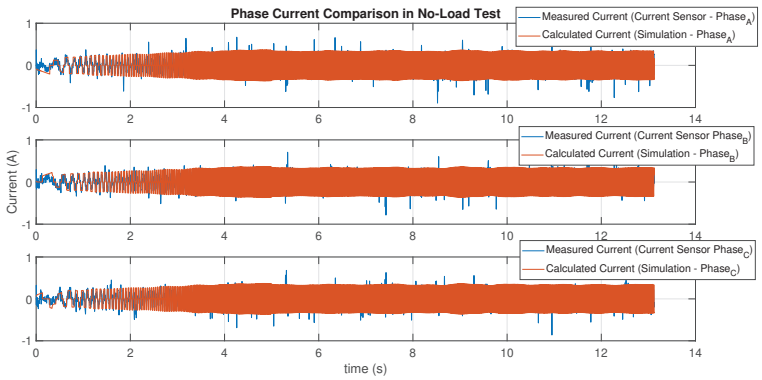

Figure B.3. Current comparison at no-load test - Comprehensive model

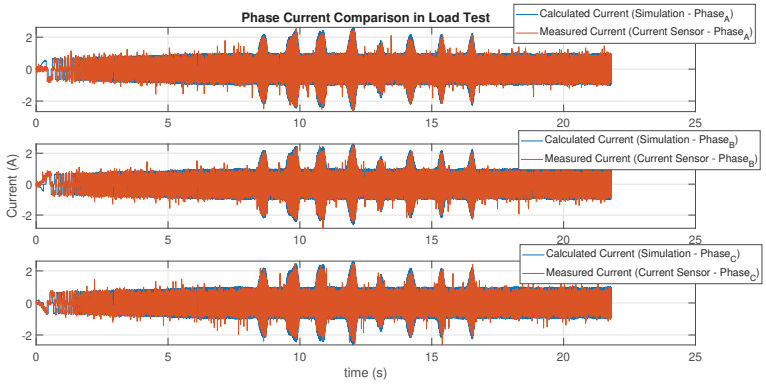

Figure B.4. Current comparison at load test - Comprehensive model

APPENDIX C

FREQUENCY RESPONSE TEST RESULTS

Table C.1. Current-Speed Frequency Response Results

Frequency (rad/s)	Output Angular Velocity (rad/s)
0.1	400.5
0.2	385.28
0.3	388.67
0.7	363.65
0.8	358.09
1.1	346.29
1.4	330.56
1.8	308.11
1.9	303.84
2.4	281.18
2.6	272.56
2.7	271.52
2.8	269.48
3	253.78
3.1	245.64
3.3	244.97
3.5	236.14
3.7	231.15
3.8	223.86
4	222.16
4.5	206.2
4.8	195.6
5	185.61
7	160.18
9	134.23
10	123.86
15	94.5
30	51.01
100	17.26

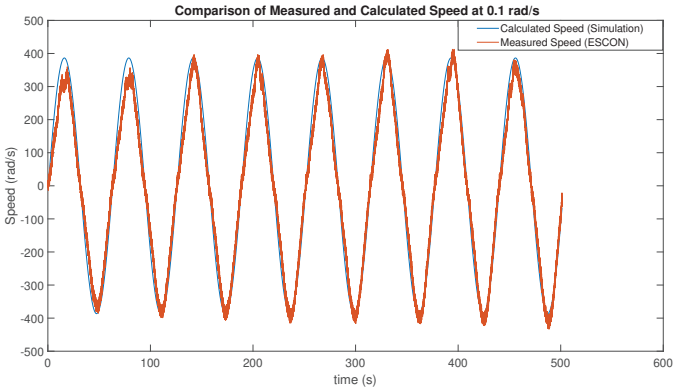

Figure C.1. Comparison of Measured and Theoretical Speed at 0.1 rad/s

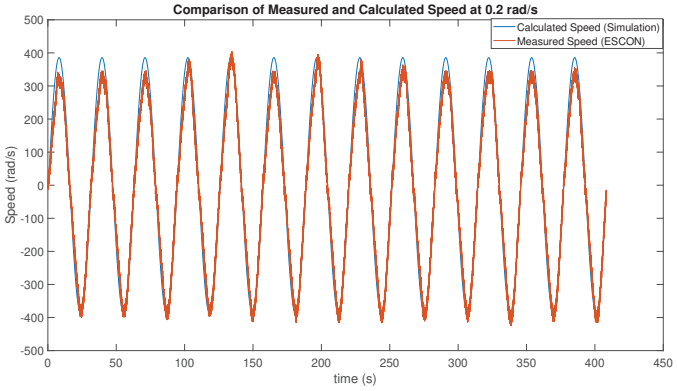

Figure C.2. Comparison of Measured and Theoretical Speed at 0.2 rad/s

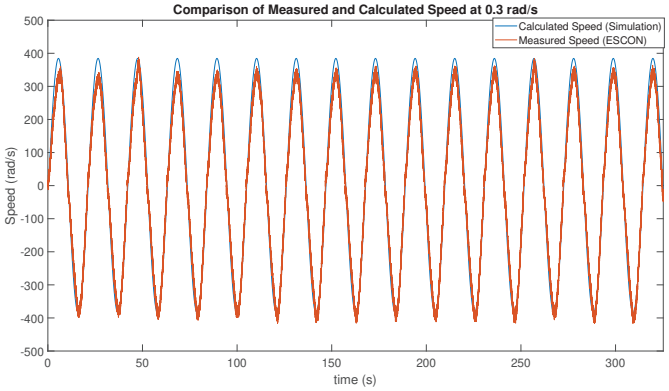

Figure C.3. Comparison of Measured and Theoretical Speed at 0.3 rad/s

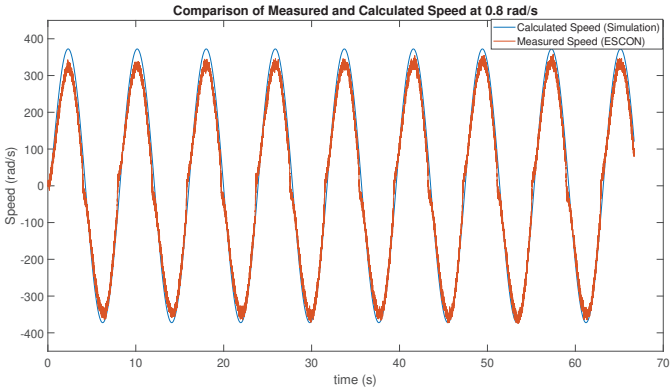

Figure C.4. Comparison of Measured and Theoretical Speed at 0.8 rad/s

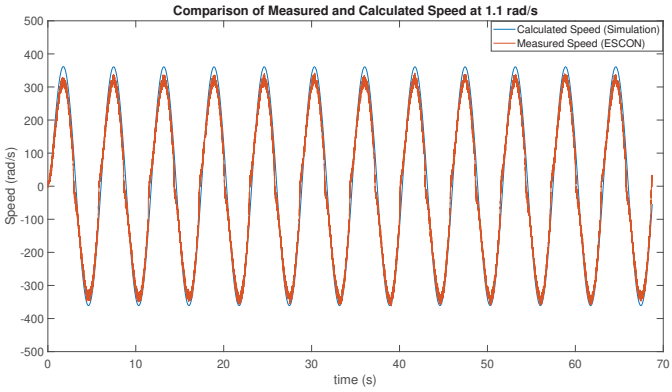

Figure C.5. Comparison of Measured and Theoretical Speed at 1.1 rad/s

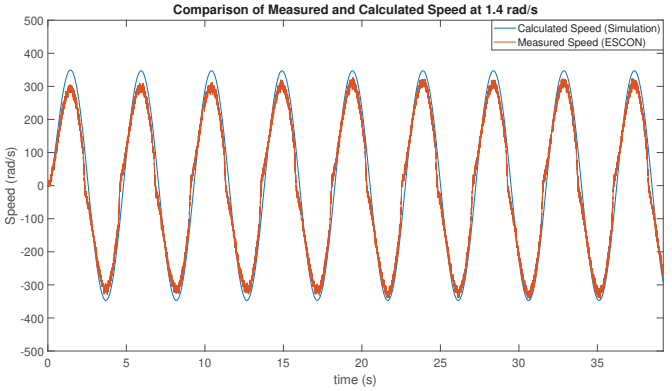

Figure C.6. Comparison of Measured and Theoretical Speed at 1.4 rad/s

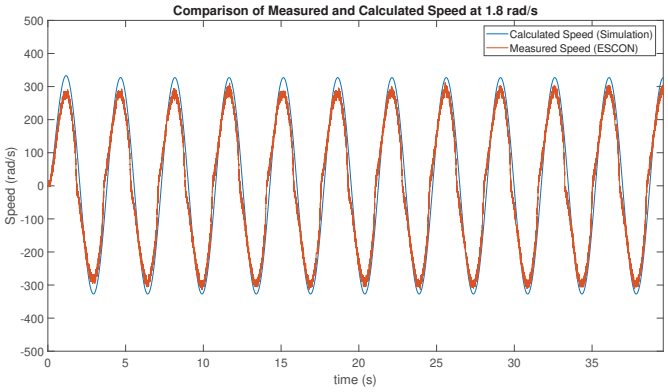

Figure C.7. Comparison of Measured and Theoretical Speed at 1.8 rad/s

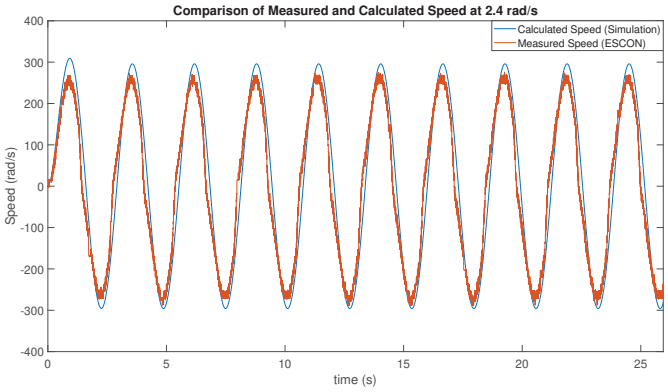

Figure C.8. Comparison of Measured and Theoretical Speed at 2.4 rad/s

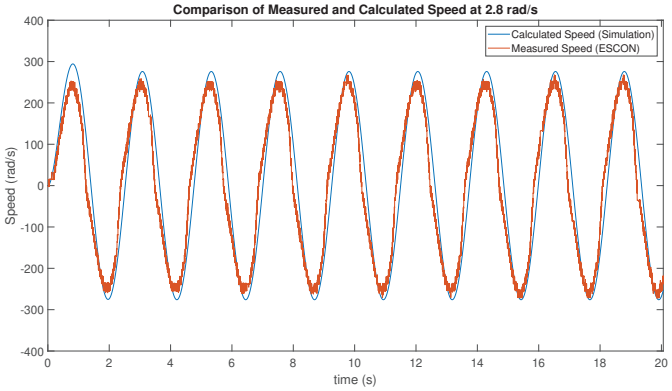

Figure C.9. Comparison of Measured and Theoretical Speed at 2.8 rad/s

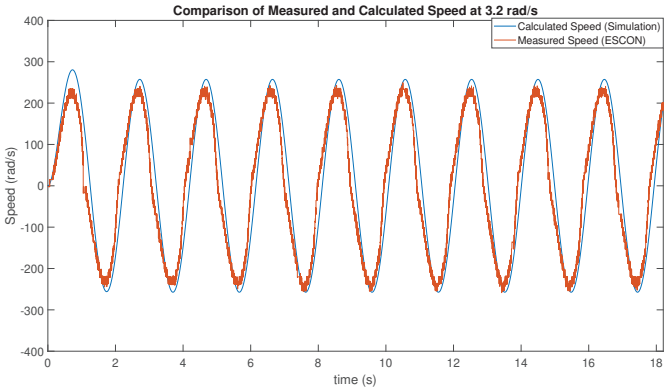

Figure C.10. Comparison of Measured and Theoretical Speed at 3.2 rad/s

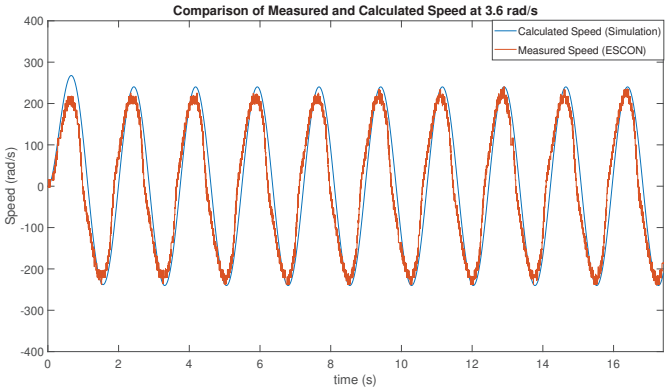

Figure C.11. Comparison of Measured and Theoretical Speed at 3.6 rad/s

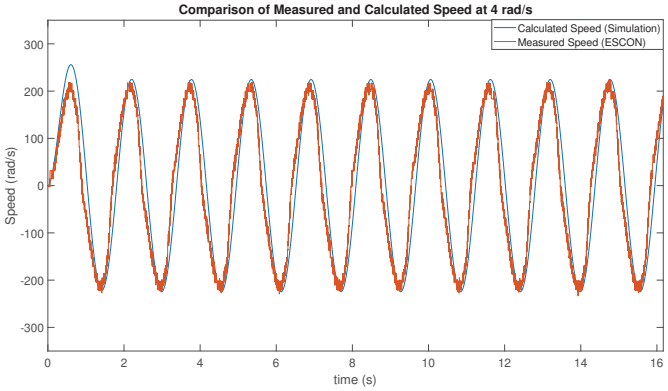

Figure C.12. Comparison of Measured and Theoretical Speed at 4 rad/s

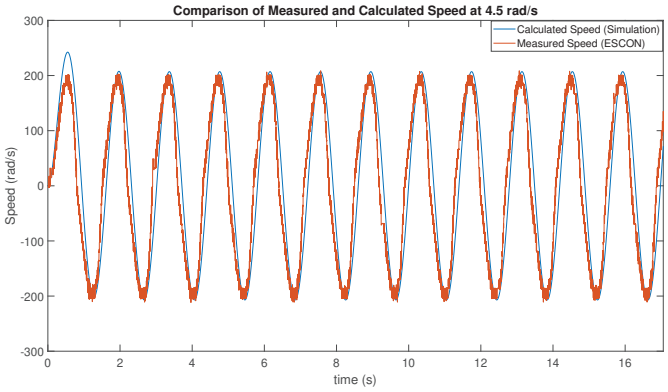

Figure C.13. Comparison of Measured and Theoretical Speed at 4.5 rad/s

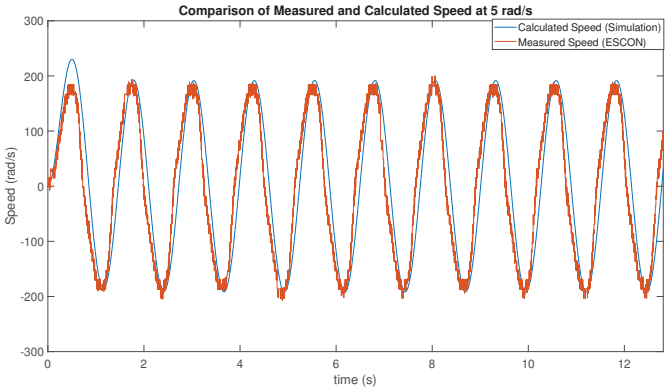

Figure C.14. Comparison of Measured and Theoretical Speed at 5 rad/s

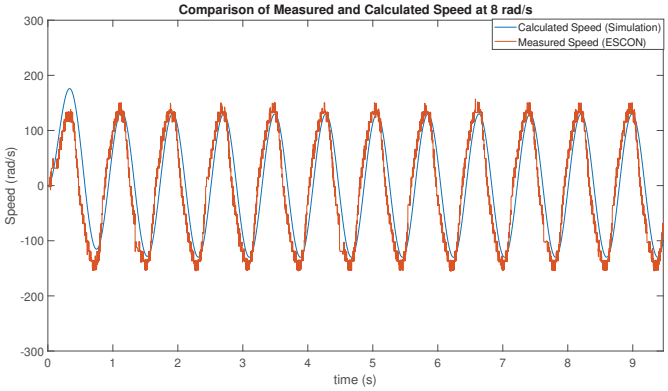

Figure C.15. Comparison of Measured and Theoretical Speed at 8 rad/s